ABSTRACT

Title of dissertation: CASIMIR AND OPTICAL PHENOMENA IN TWO-DIMENSIONAL SYSTEMS

Andrew A. Allocca,
Doctor of Philosophy, 2019

Dissertation directed by: Professor Victor M. Galitski
Department of Physics

The nature of the interaction of light with matter is a long-standing subject of great interest in condensed matter physics. Here I study the behavior of three electromagnetic effects arising from the coupling of light to two-dimensional electron systems: the Casimir effect, excitons in an insulator, and the formation of polaritons in a cavity.

I begin by examining how the Casimir effect is affected by material properties. First we consider using the Casimir force as a probe of a change in the topology of a material's Fermi surface called a Lifshitz transition. Specifically, I study a spin-orbit coupled semiconducting system, which can be made to undergo this sort of transition with an external magnetic field, and find that the signature of this transition is a non-analyticity in the Casimir force at the transition point.

I next consider how the phenomenon of weak localization can be used as a test of the role of disorder in the Casimir effect between metallic objects. I show how the sensitive dependence of the conductivity of a two-dimensional disordered metal on both temperature and magnetic field should translate into similar sensitivities of the Casimir force, assuming effects of disorder should be included at all.

Next, I examine excitons formed in the bulk of an insulator as a system transitions between topological and trivial insulating phases, finding that the phases have different signatures in the exciton spectrum. This can be understood as an effect of the Berry curvature of the model, giving an indirect glimpse of topological properties. I construct a semiclassical model of the system to develop a qualitative intuition, then move to a numerical calculation in a full quantum model.

Finally, I consider the formation of polaritons inside of a photonic cavity containing a two-dimensional superconducting layer. I show how a coupling can be engineered between cavity photons resonant with a collective mode of the superconductor called the Bardasis-Schrieffer mode, leading to hybridized superconductor polariton states. Motivated by exciton polariton condensates, I conjecture that a phase-coherent density of these objects could produce an exotic $s \pm id$ superconducting state.

CASIMIR AND OPTICAL PHENOMENA IN TWO-DIMENSIONAL SYSTEMS

by

Andrew Anthony Allocca

Dissertation submitted to the Faculty of the Graduate School of the
University of Maryland, College Park in partial fulfillment
of the requirements for the degree of
Doctor of Philosophy
2019

Advisory Committee:
Professor Victor M. Galitski: Chair
Professor Theodore Einstein
Professor Mohammad Hafezi
Professor Frederick Wellstood
Professor Victor Yakovenko

Dedication

to my family

Acknowledgements

There are many people who deserve recognition for helping me get through graduate school, both colleagues who contributed to research and my friends and family who supported me throughout.

First and foremost I have to express my sincere gratitude to my advisor, Victor Galitski. He has provided me with so many interesting research questions to work on and no shortage of guidance to help me do so. In my time working with him I have learned a great deal about how to be a physicist, and this dissertation would not have been possible without him.

I must also acknowledge the invaluable guidance provided to me by Justin Wilson. We started collaborating as soon as I joined Victor's group, and he helped me first learn many of the fundamental techniques I use in my research on a near daily basis. Out of our collaboration came my first three papers, two of which are presented in this dissertation, as well as a lasting friendship.

My other collaborators have likewise been a privilege to work with. Dmitry Efimkin and Zachary Raines in particular have had a significant impact on my time in graduate school. Dmitry has offered far more advice and support than he had any obligation to, even long after our work together had finished, and for that I am very grateful. Zach has been not only my chief collaborator for a number of years, but also one of my best friends throughout the entire time I've been at UMD. I'm thankful to Mohammad Hafezi for many fruitful discussions and his very helpful guidance. Jonathan Curtis also deserves special recognition in this list for providing invaluable contributions to a number of recent projects.

I'd also like to thank the rest of my office and group-mates over the years, especially Joe Mitchell, Hilary Hurst, Aydin Keser, Efim Rozenbaum, Valentin Stanev, and Mehdi Kargarian, as well as all the friends I've made while I've been

here.

Last but certainly not least I thank my family, especially my parents. I would not be where I am now without your confidence in me and your unwavering love and support.

Table of Contents

List of Tables

List of Figures

List of Abbreviations

BCS **B**ardeen-**C**ooper-**S**chrieffer

BHZ **B**ernevig-**H**ughes-**Z**hang

BS **B**ardasis-**S**chrieffer

RPA **R**andom **P**hase **A**pproximation

TI **T**opological **I**nsulator

UCF **U**niversal **C**onductance **F**luctuations

WL **W**eak **L**ocalization

List of Publications

This dissertation is based on the author's following publications:

1. A. A. Allocca, J. H. Wilson, and V. Galitski, "Nonanalytic behavior of the Casimir force across a Lifshitz transition in a spin-orbit-coupled material", Phys. Rev. B **90**, 075420 (2014).

2. A. A. Allocca, J. H. Wilson, and V. M. Galitski, "Quantum interference phenomena in the Casimir effect", Phys. Rev. A **91**, 062512 (2015).

3. A. A. Allocca, D. K. Efimkin, and V. M. Galitski, "Fingerprints of Berry phases in the bulk exciton spectrum of a topological insulator", Phys. Rev. B **98**, 045430 (2018).

4. A. A. Allocca, Z. M. Raines, J. B. Curtis, and V. M. Galitski, "Cavity superconductor-polaritons", Phys. Rev. B **99**, 020504 (2019).

Other publications by the author:

1. J. H. Wilson, A. A. Allocca, and V. Galitski, "Repulsive Casimir force between Weyl semimetals", Phys. Rev. B **91**, 235115 (2015).

2. J. B. Curtis, Z. M. Raines, A. A. Allocca, M. Hafezi, and V. M. Galitski, "Cavity quantum Eliashberg enhancement of superconductivity", Phys. Rev. Lett. **122**, 167002 (2019).

3. Z. M. Raines, A. A. Allocca, and V. M. Galitski, "Manifestations of spin-orbit coupling in a cuprate superconductor", arXiv e-prints (2018), arXiv:1812.07949 [cond-mat.supr-con].

4. Z. M. Raines, A. A. Allocca, M. Hafezi, and V. M. Galitski, "Cavity Higgs-Polaritons", arXiv e-prints (2019), arXiv:1905.03377 [cond-mat.supr-con].

Chapter 1: Introduction

In the low-energy realm of condensed matter physics the electromagnetic force is of singular importance. All interactions typically considered in condensed matter systems are ultimately of electromagnetic origin, from electron-electron interactions, to the formation of crystal lattices—and therefore the accompanying electronic band structures and Fermi surfaces—and even the phonon-induced interactions responsible for conventional superconductivity. In these specific examples, however, electromagnetism plays only a supporting role, in the sense that it is sufficient to consider just its static component in the form of the Coulomb interaction, and unnecessary to treat the electromagnetic field as a dynamical quantum field on par with the treatment of electrons.

For many other low-energy condensed matter phenomena the dynamical nature of the electromagnetic field is crucial. A simple example is the use of optical probes to ascertain properties of a sample; precise measurements of the interaction of light with a material can be used to gain insight into a number of its properties including, in different circumstances, bond strengths, band structures, the presence of bound states or collective modes, and the ordering of electrons. In these instances light must be considered explicitly, though it is still of secondary concern—it is an external probe, not an intrinsic part of the system being studied.

Other phenomena can only be fully understood by considering light and matter on a more equal footing. One example is the Casimir effect [1], a typically attractive force between objects at very small scales due to fluctuations of the electromagnetic field between them. Another example is the formation of polaritons—hybrid excitations of light and matter. In these cases light and matter are both essential ingredients that are strongly coupled, and must be treated as full dynamical de-

grees of freedom in order to accurately describe the nature of the combined system. Measurements made on systems hosting these effects can still be leveraged to gain insight into microscopic properties of the system as well. Additionally, because light is relatively straightforward to control in very precise ways, these effects provide a potential means to manipulate modes in electronic systems that are otherwise hard to access. In this dissertation I consider these different perspectives as I examine solid-state systems that feature such prominent electromagnetic effects.

Two-dimensional systems in particular are my primary focus for a number of reasons. The first is that some effects that I wish to study, such as weak localization (see Sec. 1.2.2), occur only in low-dimensional systems. The second, related, reason is that considering a three-dimensional system could preclude an effect we wish to study. For example, a thin-film superconducting layer may appear relatively transparent to light, while a thick superconducting slab would not. The third reason is that considering two dimensions instead of three can sometimes strip away complications which are unimportant for the questions of primary interest, and so provide a good starting point for future investigations. The results obtained by examining two-dimensional system, while not necessarily quantitatively applicable to a three-dimensional analog, in some cases can nonetheless be an indicator of qualitative behaviors higher dimensional systems may exhibit.

The coupling of light and matter considered in this dissertation can be understood at the level of the linear response of electrons to the electromagnetic field. This response given by the tensor function $\hat{\Pi}$ defined through $\mathbf{j} = \hat{\Pi}\mathbf{A}$, where $\mathbf{j}$ is the charge current in an electronic system and $\mathbf{A}$ is the electromagnetic vector potential (or, alternatively, the photon field). This function is a straightforward object to calculate and contains all the relevant properties of the solid-state system in question regarding its coupling to light.

I begin in Chapters 2 and 3 with a consideration of the Casimir effect and

how it depends on microscopic material properties. In Chapter 2 I investigate the signatures of a change in Fermi surface topology, called a Lifshitz transition, in the Casimir force, and in chapter 3 I consider how the phenomenon of weak localization in two-dimensional disordered metals can be used as a test of the importance of disorder in calculations of the Casimir effect between metallic objects. In Chapter 4 I shift to an examination of excitons in the bulk of a two-dimensional topological material, using the exciton spectrum as a means to detect nontrivial topological properties. In Chapter 5 I demonstrate how photon modes in a microwave cavity can be hybridized with a particular collective mode in a superconductor in order to form new polaritonic objects. Finally, in Chapter 6 I end with a summary of my main findings.

Before getting to these projects in detail, however, in the following sections of Chapter 1 I provide an overview and introduction to the general phenomena I will be discussing.

1.1 Casimir and optical phenomena

In this section I introduce the three phenomena that I investigated, which can be primarily understood as effects of the electromagnetic field: the Casimir effect, the formation of excitons, and the formation of polaritons in microwave cavities. Though a coupling to matter is a vital ingredient to produce all of these effects, much can be said about each of them in general without the need to introduce specific microscopic properties of the actual material systems.

1.1.1 The Casimir effect

In 1948 Hendrik Casimir predicted the existence of an attractive force between two neutral, perfectly conducting materials as a result of quantum fluctuations of the electromagnetic vacuum [1] . He argued that the electromagnetic field between

two such plates separated by a finite distance a becomes quantized, and that the vacuum energy of the field in such a configuration will be,

$$E_0(a) = \frac{\hbar}{2} \sum_{\mathbf{k},\sigma} \omega_\sigma(\mathbf{k}), \tag{1.1}$$

where $\omega_\sigma(\mathbf{k})$ is the frequency of the mode with wavevector $\mathbf{k}$ and polarization σ. While the result of this sum is divergent, subtracting off the likewise divergent energy for infinitely separated plates gives a finite result. That is to say, the quantity $E_c(a) \equiv E_0(a) - E_0(a \to \infty)$, defined as the change in the vacuum energy from its free space value, is finite and may have a real physical meaning [1]. This is now known as the Casimir energy, and yields a force between the plates arising purely from fluctuations of the vacuum as $F_c(a) = -\partial E_c(a)/\partial a = -\hbar c \pi^2/(240 a^4)$. Throughout my further discussion of the Casimir effect, I will remain focused on the two parallel plate geometry, labeling the two plates as A and B, though other configurations can be and have been considered elsewhere [2].

For many years following Casimir's first theoretical prediction, developments were limited primarily to extensions of the theoretical understanding of the effect, for instance in more realistic models of the plates as first considered by Lifshitz [3, 4]. Precise experimental evidence of the Casimir effect was first presented by Lamoreaux [5], who measured the effect to within 5% of predictions. Following this important result there has been a great deal more work done on the Casimir effect, both theory [2, 6, 7] and experiment [8–13], which has led to an astounding variety of techniques to analyze the effect.

With this machinery, others have observed that the Casimir force can have a non-trivial dependence on material parameters [14–20], some of which may be tunable. The possibility of tuning the Casimir force by modifying optical properties [21–23]

[1] An alternative method of arriving at this result is to consider regulating the formally divergent sum for the vacuum energy, for example with dimensional or zeta-function regularization. The result is the same, though the physical interpretation is less clear.

could have important applications for precision gravity experiments [24–28] and applications to nanotechnology [29]. Special geometries [30] and boundary conditions [31] can change the Casimir force to be repulsive, though with symmetric geometries without time-reversal symmetry breaking, one cannot escape an attractive effect [32]. Just as a repulsive effect would be a signature of some time-reversal symmetry breaking (such as in the case of two quantum Hall plates [33], topological insulators with gapped surface states [34], or thin-film Weyl semimetals [35]), other changes in the Casimir force can be attributed to other material properties. For instance, Bimonte *et al.* showed that one can in principle measure the change in Casimir energy if a plate changes from the normal state to the superconducting state [16, 17]. Additionally, it has been demonstrated that both the Casimir effect and the thermal Casimir effect [18] are capable of probing phase transitions [19, 20].

I now shift focus to the theoretical frameworks used to study the Casimir effect. In Casimir's original work the electromagnetic properties of the plates, being perfect conductors, were straightforwardly included as simple boundary conditions on the electromagnetic field. When considering real materials, first done by Lifshitz [3, 4], the effect is still dependent on the boundary conditions of the electromagnetic field, but these are no longer as trivial to write down and must be determined from the interactions of the plates with the electromagnetic field. Treating the plates as classical objects as Lifshitz did, the fundamental object to consider is the dielectric function from which one can derive the reflection properties of light off the plates. In this case the Casimir energy is given by what is now known as the Lifshitz formula, which at finite temperature T takes the form

$$E_c(a) = \frac{\hbar}{\beta} {\sum_{\omega_m}}' \int \frac{d^2q}{(2\pi)^2} \operatorname{tr} \log \left[\mathbf{1} - R_A R_B e^{-2q_z a} \right], \tag{1.2}$$

where $\omega_m = 2\pi n T$ is the Matsubara frequency, $\beta = 1/T$, ${\sum}'$ denotes a sum over

only non-negative Matsubara frequencies, with the $m = 0$ frequency included with half weight, the trace is taken over the 2×2 space of the polarizations of light, and $q_z = \sqrt{\omega_m^2 + q^2}$, with q being the photons' two-dimensional momentum parallel to the plates. The reflection matrices R_A and R_B are generally functions of frequency and depend on the material from which the plates are made.

When microscopic effects in the plates are of interests, as in Chapters 2 and 3, it is useful to understand the Casimir effect starting from a purely quantum mechanical perspective. A microscopic derivation of the Casimir energy for parallel two-dimensional plates at zero temperature is provided in the appendix of Ref. [36], and the generalization to finite temperature is straightforward. In the context of quantum field theory, the Casimir energy can be understood as a component of the free energy of the total matter-plus-photon system. Similar to the original derivation, it is calculated as the total free energy minus those parts of the free energy corresponding the self-energy of the plates in isolation, setting the zero of energy. Diagrammatically, this corresponds to the class of closed-loop diagrams that have photons interacting with both plates, as depicted in Fig. 1.1. The contributions of these diagrams can be summed to give the expression

$$E_c(a) = \frac{\hbar}{\beta} {\sum_{\omega_m}}' \operatorname{Tr} \log \left[\mathbf{1} - \tilde{\Pi}_A D_{AB}(a) \tilde{\Pi}_B D_{BA}(a) \right], \tag{1.3}$$

where $\sum'$ has the same meaning as in Eq. (1.2), the trace is now a full trace over all other indices these objects may have, including photon polarizations and momentum, and $D_{AB}(a)$ is the photon propagator from plate A to plate B and depends on the distance between them a. The functions $\tilde{\Pi}$ represent the total interaction of photons with the plates, including the full photon-generated self-energy. The strict alternating pattern of interactions with the plates as one traverses the loop diagrams is a result of including this self-energy.

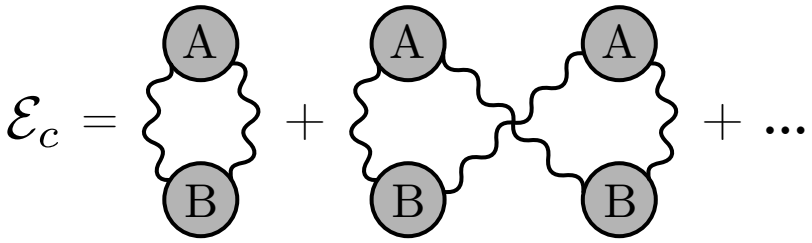

Figure 1.1: The diagrammatic representation of the Casimir energy as part of the free energy, specifically all diagrams involving interactions of photons with both plates. Photon propagators are represented as wavy lines and the full interaction of the plates with light are represented as filled circles, labeled by plate.

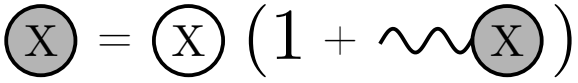

Figure 1.2: The diagrammatic representation of the RPA screening used to calculate the interaction of a plate with photons. The filled circle represents the screened interaction and the empty circle is the bare interaction, given by the current-current correlation function of the plate.

In practice, considering the full interaction of photons with the plates is unfeasible, so an approximation must be made to $\tilde{\Pi}$. The most useful way to do so relates $\tilde{\Pi}$ to the linear response of the plates to the electromagnetic field through the random phase approximation (RPA, see Fig. 1.2). For two-dimensional plates this approximation gives

$$\tilde{\Pi}_X = \Pi_X \left(1 + D_{XX}\tilde{\Pi}_X\right) \quad \Rightarrow \quad \tilde{\Pi}_X = (1 - \Pi_X D_{XX})^{-1}\Pi_X, \tag{1.4}$$

where D_{XX} is the photon propagator from plate X to itself and Π_X is the current-current correlation function for plate X, which relates currents to the vector potential as $j_i = \Pi_{ij}A_j$. Because the dielectric function of a material is related to Π_{ij}, this appeal to the RPA allows us to relate the microscopic treatment to a classical treatment of the plates. Indeed, in two dimensions one can verify that the formulation in terms of RPA dressed interactions is entirely equivalent to the Lifshitz formula in terms of reflection coefficients derived from the macroscopic classical framework.

Despite this microscopic understanding of the Casimir effect and the sophisticated

theoretical work on sometimes relatively esoteric model systems, a surprisingly fundamental question remains unanswered regarding how to best consider one of the simplest of systems. The question regards how metallic plates should be treated microscopically: is the Casimir effect best described by modeling metallic plates with the Drude model or the plasma model? The Drude model considers diffusive electron motion resulting from a random disorder potential, and the plasma model describes ballistic electrons free of disorder scattering effects. Both typically yield similar predictions of the Casimir force as a function of distance between the plates, although the plasma model predicts a slightly stronger attraction than the Drude model in nonmagnetic metals.

Quantitative results from many experiments [37–40] seem to favor use of the plasma model over a naive Drude model, which is generally considered to be the more physical of the two because disorder is ubiquitous in real materials. Many experiments attempt to account for the effect of electrostatic patch potentials in the plates [18, 39–41], expecting the effect to be relevant for agreement with one model or the other. Several of these [39, 40] find that the correction due to patch potentials would make agreement with the Drude model worse while others [18, 41] see agreement with it once the effect of patches is included. There is recent theoretical and experimental work specifically to account for the contribution of patch potentials [42, 43]. While the initial theoretical results seemed to weaken the case for the plasma model, the comparison of calculation and experiment shows the contribution to the force from patch potentials to be approximately an order of magnitude smaller than the difference between the Drude and plasma models. However, the authors caution that the analysis is preliminary and acknowledge that future work may be needed. More recent experimental investigations into the role of patch potentials show that the manner of fabrication is important, and that the contribution of patches to the total measured force can be comparable to the

difference between the plasma and Drude predictions [44].

In the same vein as the work done on patch potentials, there has also been investigation into the effect of charge disorder [45]. This work finds that quenched and annealed disorder contribute to the Casimir force in markedly different ways, with quenched disorder completely overwhelming the Casimir force at large distances.

In this dissertation I examine the behavior of the Casimir effect in response to changes in the properties of the plates. In Chapter 2 I examine how a particular type of transition in the plates (a Lifshitz transition, see Sec. 1.2.1) may be observed using the Casimir force, and in Chapter 3 I consider the effect of weak localization (see Sec. 1.2.2), a disorder phenomenon particular to two-dimensional systems, and show how this yields significantly different predictions from the Drude and plasma models.

1.1.2 Excitons in Semiconductors

Excitons are bound states of particles and holes that can form in systems with a filled valence band and an empty conduction band that are separated by a finite energy gap. Excitons typically occur in semiconductors [46–48], and, being bound states, excitons have lower total energy than is needed to excite a free particle and hole. When considering the two-particle excitation spectrum of the system, exciton states appear as discrete energy levels below the two particle continuum. Their properties can be calculated by considering the same sort of two-particle problem as in the hydrogen atom, but with a particle and a hole interacting via the Coulomb interaction instead of a proton and electron. Writing down the two-particle Hamiltonian, one arrives at a Schrödinger equation for excitons,

$$(E_c(\mathbf{k}) - E_v(\mathbf{k}))\Phi(\mathbf{k}) - \sum_{\mathbf{k}'} U_{\mathbf{k}-\mathbf{k}'}\ \mathcal{F}_{\mathbf{k},\mathbf{k}'}\ \Phi(\mathbf{k}') = E\,\Phi(\mathbf{k}), \tag{1.5}$$

where Φ and E are the exciton wave function and energy, $U_{\mathbf{k}-\mathbf{k}'}$ is the Fourier transform of the Coulomb interaction, and $E_c(\mathbf{k})$ and $E_v(\mathbf{k})$ are the dispersion relations for the particle and hole respectively (the subscripts refer to the conduction and valence bands, in which each resides), which can be combined into a dispersion for the composite object with a single effective mass. The only component of this equation significantly differing from the description of the hydrogen atom is the factor $\mathcal{F}_{\mathbf{k},\mathbf{k}'} = \langle c, \mathbf{k}|c, \mathbf{k}'\rangle \langle v, \mathbf{k}'|v, \mathbf{k}\rangle$, where $|c, \mathbf{k}\rangle$ and $|v, \mathbf{k}\rangle$ are the single particle eigenstates of the noninteracting Hamiltonian. Apart from details of the band structure, which also appear in the kinetic term, most of the properties specific to the system hosting the excitonic states are included through this factor.

The structure of the exciton spectrum depends on the details of the system impacting $\mathcal{F}$, including its dimensionality and symmetries. For the simple three-dimensional rotationally symmetric case $\mathcal{F} = 1$, and for parabolic bands the structure of exciton energy levels is identical to that of the spectrum of the hydrogen atom—the eigenstates are indexed by three quantum numbers, and symmetry enforces that the energy of all angular momentum states for a given principal quantum number are degenerate. For a two-dimensional system the same is true, but with states indexed by two quantum numbers instead of three. Most ways of changing the system away from this idealized model gives $\mathcal{F} \neq 1$, breaking the symmetry that ensures this degeneracy.

The most straightforward way to observe exciton states is by optical means, such as through optical absorption measurements [49–52]. The system can absorb a photons with energy resonant with the exciton spectrum and populate the states. However, because photons only carry angular momentum $\ell = \pm 1$, only a small subset of the full spectrum can be accessed in this way, i.e. those states with angular momentum differing from the ground state by ± 1. A more technical discussion of how excitons appear in the optical properties of a system, including a derivation of

Eq. (1.5), is presented in Appendix A.

In chapter 4 I examine how topological properties are reflected in the energy spectrum of excitons formed within a system's bulk.

1.1.3 Cavities and Polaritons

A nontrivial way of manipulating the electromagnetic environment surrounding a material systems is to place it in a low-loss resonant cavity, by which I mean a volume of space where the enclosed electromagnetic field is subject to a set of nontrivial boundary conditions. One of the simplest types of cavities to consider is a set of neutral, parallel, perfectly conducting plates located at $z = 0$ and $z = L$. Confinement along the z-direction quantizes the photon modes in the cavity and so the photon dispersion becomes

$$\omega_q = cq \to \omega_{q_\perp,n} = c\sqrt{\left(\frac{n\pi}{L}\right)^2 + q_\perp^2}, \tag{1.6}$$

where $q_\perp$ is the two-dimensional momentum perpendicular to the z-direction (lying in the x–y plane) and n indexes the now quantized states. From here onward I will redefine q to mean $q_\perp$, and we will restrict attention to only the lowest mode, $n = 1$, then drop the index n. Examining (1.6) we see that in such a cavity the photons acquire a rest mass π/Lc and no longer disperse linearly as they would in vacuum. Indeed, for $cq \ll \omega_0$ the above dispersion can be expanded to give approximate rest and kinetic masses for cavity photon modes.

A well-studied phenomenon that makes use of these massive photon states is the formation of cavity exciton polaritons [53]—hybrid excitations of cavity photons and excitons within a semiconducting quantum well—which were first observed experimentally in the early 1990s by Weisbuch *et al.* [54]. Many properties of these

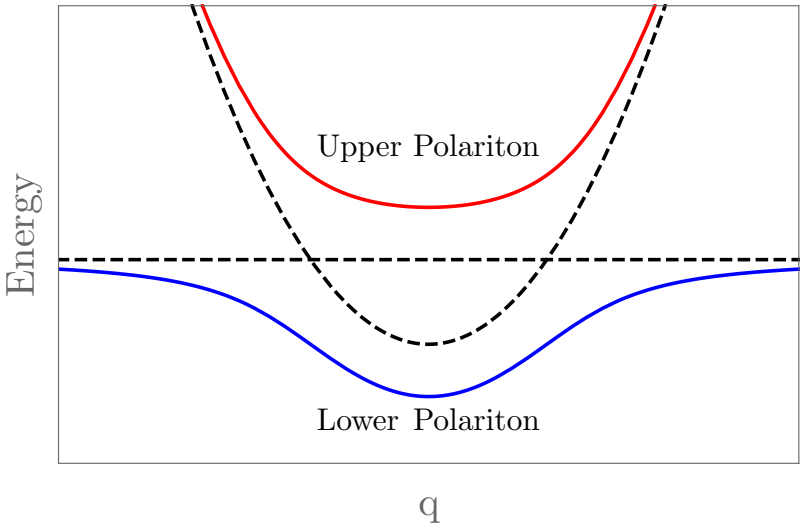

Figure 1.3: Dispersion obtained from diagonalizing the exciton polariton Hamiltonian, Eq. (1.7). The upper polariton branch (red) and the lower polariton branch (blue) are formed from hybridization between the original exciton and photon dispersion (dashed).

objects can be accurately described by a simple Hamiltonian,

$$H = \begin{pmatrix} \Omega_{\text{ex}} & g \\ g & \omega_q \end{pmatrix} \tag{1.7}$$

where Ω_{ex} represents the energy of an exciton in its center of mass frame, g is the coupling between an exciton and light, and ω_q is the cavity photon dispersion as in Eq. (1.6). We can ignore the dispersion of excitons in this model because their kinetic mass is much greater than that of the cavity photons; excitons appear nondispersive on the timescales relevant for photon dynamics. Diagonalizing this Hamiltonian gives the two cavity exciton polariton states, as shown in Fig. 1.3. These states have nontrivial overlap with cavity photon states and can therefore be excited optically. By pumping the cavity modes and measuring the transverse momentum of emitted photons, the polariton dispersion can be imaged directly [55], confirming that this simple theoretical model accurately reflects the physics of the system.

For small q the effective mass of the lower polariton branch is primarily deter-

mined by the very small effective photon mass in the cavity. Because the condensation temperature for bosons is related to the inverse of their effective mass [56], this allows for the remarkable phenomenon of Bose condensation of exciton polaritons at high temperatures. Indeed, polariton condensation up to room temperature is well established experimentally [57–59], and polariton condensates have found use in a number of applications, including quantum simulation of solid state physics [60–63], acoustic black hole physics [64], and topological properties of quasicrystal states [65]. A review of the properties of exciton polaritons, and the coupling of light to matter in this general context, is provided by Carusotto and Ciuti [66], for example.

In Chapter 5 I consider how a close analog of cavity exciton polaritons may be formed when replacing the excitons hosted in a semiconducting quantum well with a collective mode in a superconducting layer.

1.2 Particular phenomena in solid-state systems

In the previous section I described three phenomena of interest that result from the interaction of light with matter. I noted that much could be said about those phenomena without using specific details of the matter being coupled to. In this section I now go on to describe some of the interesting properties and effects hosted by the materials systems that will be considered in later chapters.

1.2.1 Lifshitz transitions

A Lifshitz transition occurs when the topology of a system's Fermi surface changes, for instance, due to the opening or closing of an electron or hole pocket [67, 68], which is what we will consider. In principle this is only a truly sharp transition at zero temperature. At any finite temperature the Fermi distribution describing the occupation of electron states has a tail, so states up to high energy have a small non-zero occupation probability. Therefore, as a band is, for example, pushed to

energies above the chemical potential μ as a result of tuning a parameter, there is no particular value of this parameter for which the occupation of the band suddenly drops to zero. For small but finite temperatures $T/\mu \ll 1$, however, a fairly sharp effect may still be observed. For simplicity I consider systems at precisely zero temperature so the effect is most clearly defined.

There are a number of systems that are believed to undergo a Lifshitz transition of some variety [69–71] including the cuprate superconductors [72] and iron arsenic superconductors [73].

Because I am concerned with the coupling of a system displaying a Lifshitz transition to light, the most important aspect of such a transition is the effect on the electromagnetic response of the material. For instance, a Lifshitz transition resulting from tuning some parameter manifests as a nonanalytic kink in the conductivity as a function of the tuning parameter. It follows that any effects that depend on the optical properties of the system will also display similar nonanalytic behavior as a function of this parameter.

1.2.2 Weak localization

Weak localization (WL) [74–78] is a well known and long-studied effect in disordered low-dimensional metals, in which charge carriers moving through a sample localize due to quantum interference of their wave functions, leading to a suppression of the conductivity at low temperatures. The modification of conductivity is most straightforwardly understood through the Einstein relation $\sigma = e^2 \nu D$, where ν is the electronic density of states at the fermi level in the sample and D is the material's diffusion constant. We can include weak localization in this relation as a correction to the diffusion constant $D \to D + \delta D$ resulting from a variety of quantum processes not typically considered in calculations of conductivity. Because WL is quantum mechanical in origin, arising from phase coherence of charge carriers, the

correction is very sensitive to dephasing processes such as thermal excitation or magnetic effects.

A straightforward picture can be used to qualitatively explain most of the relevant features of the WL effect. In a semiclassical framework, every path p an electron can take through a sample can be assigned an amplitude A_p. The total probability for an electron to propagate between two points is then represented as the square of the total amplitude for propagating between those points,

$$\mathcal{P} = \left| \sum_p A_p \right|^2 = \sum_{p_1,p_2} A^*_{p_1} A_{p_2} = \sum_p \left| A_p \right|^2 + \sum_{p_1 \neq p_2} A^*_{p_1} A_{p_2}. \tag{1.8}$$

Consider the last term, which accounts for interference. In the subset of paths possessing self-intersections, i.e. those paths with loops. For every path traversing a loop in one direction, there is another that is identical except for the direction of propagation around the loop. As long as the electron maintains phase coherence long enough, then the two oppositely directed trajectories around the loop interfere constructively, and the probability to find the electron somewhere along the loop increases. Because the electron is more likely to be in the loop, it is less likely to be transmitted though the sample and contribute to a current, and so the total conductivity of the sample decreases compared to if there are no loops.

Because this picture relies on electrons maintaining phase coherence long enough to traverse loops, it is clear that the effect is strongest at lower temperatures, where electron dephasing is slowest. As the temperature is lowered, coherence can be maintained for longer times, and so self-intersecting paths with larger loops can contribute to the localization effect, causing it to become stronger and conductivity to be suppressed further. Conversely, raising the temperature destroys phase coherence, and weakens the effect. Coherence can alternatively be destroyed by applying a magnetic field to the sample. As electrons traverse the loop paths, they will acquire

an additional phase proportional to the flux of the magnetic field through the loop. In the semiclassical explanation above, this corresponds to the introduction of a phase $A_p \to A_p e^{i\phi_p}$, where ϕ_p is proportional to the magnitude of the applied field and the area of the loop, and its sign depends on the direction of propagation around the loop. Because electrons traversing counter-propagating paths will acquire opposite phases, they will no longer perfectly interfere, and so the effect of WL will be suppressed, raising the conductivity.

The WL effect can be studied more concretely by examining the electromagnetic response function Π of a noninteracting disordered electron gas, represented diagrammatically as in Fig. 1.4. The simplest approximation in calculating the response considers only those diagrams in the first line of the figure—the two diagrams without impurity lines and all ladder diagrams in the particle-hole channel, which can be resummed to give the propagator for diffusons. In the long-wavelength limit $\mathbf{q} \to 0$, these terms combine to give the Drude response function

$$\Pi^{\text{Drude}} = -\frac{ne^2}{m}\frac{\omega_m}{\omega_m + 1/\tau}, \tag{1.9}$$

from which the well-known Drude result for dc conductivity can be found, $\sigma^{\text{Drude}} = -\lim_{\omega_m \to 0} \Pi^{\text{Drude}}/\omega_m = ne^2\tau/m$.

The diagrams with maximally crossed impurity lines, given in the second line of Fig. 1.4, represent the leading correction to this result, and cannot be discarded for a precise calculation of the conductivity of two-dimensional systems at low temperatures. By "twisting" one of the electron legs around, these crossed diagrams can be redrawn as ladder diagrams in the particle-particle channel, which can then be resummed into a single diagram containing a cooperon. This approximation to the response function can be written as

$$\Pi = \Pi^{\text{Drude}} + \delta\Pi, \tag{1.10}$$

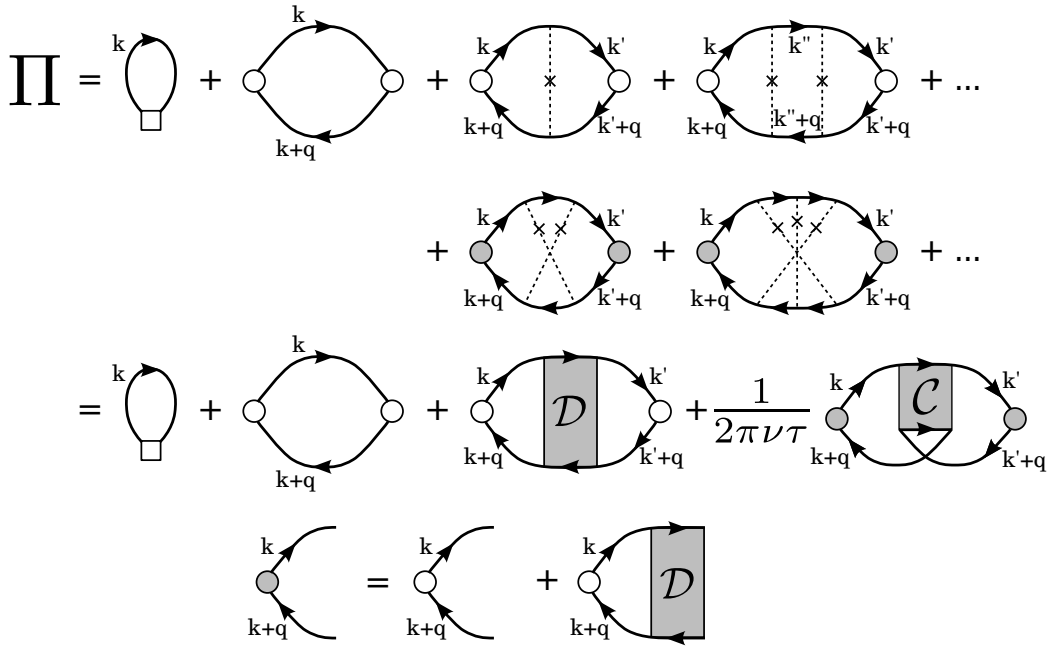

Figure 1.4: The diagrammatic expansion of Π showing the leading correction to the Drude result. Solid lines represent disorder-averaged electron Green's functions, dashed lines represent interactions with the disorder potential, the shaded regions represent diffusons (labeled with $\mathcal{D}$) or cooperons (labeled with $\mathcal{C}$), and the circles represent current vertices. The first three diagrams of the third line together give the Drude result, while the last term gives the leading correction. The last line defines the renormalized vertex.

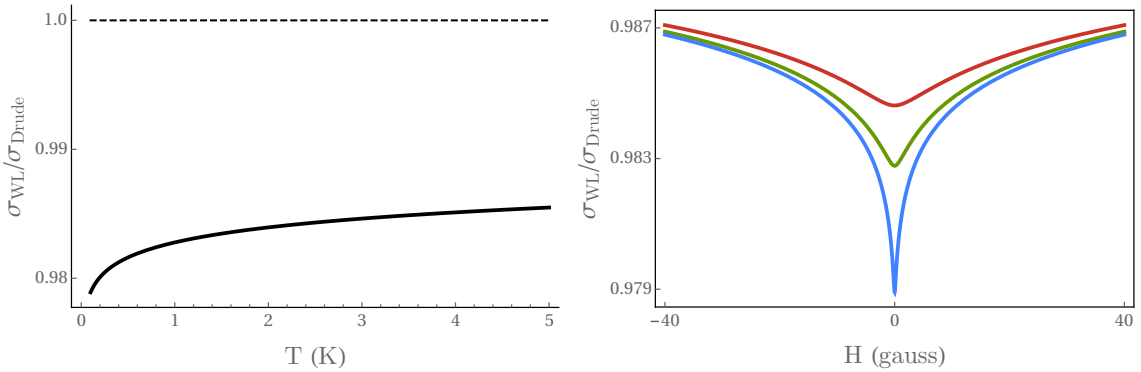

Figure 1.5: The dependence of the conductivity of a disordered 2D metal including the WL correction as a function of temperature (left) and magnetic field (right), normalized by the uncorrected Drude conductivity. On the left, the dotted line at 1 is a reference for the conductivity when ignoring the WL correction. On the right, the three curves are calculated for three different temperature, 3 (red), 1 (green), and 0.1 K (blue).

where $\delta\Pi$ gives the WL correction from the cooperon term. An explicit calculation of $\delta\Pi$ in two dimensions at low but finite temperature T and with an external magnetic field H yields the Hikami-Larkin-Nagaoka formula [74, 75]

$$\delta\Pi(i\omega_m, T, H) = -\frac{e^2|\omega_m|}{2\pi^2\hbar}\left[\psi\left(\frac{1}{2}+\frac{\hbar}{4eHD\tau_\phi(T)}\right)-\ln\left(\frac{\hbar}{4eHD\tau}\right)\right], \qquad (1.11)$$

where ψ is the digamma function, $D = v_F^2\tau/2$ is the diffusion constant in 2D, and τ_ϕ is the electron dephasing time. This correction diverges logarithmically as $T \to 0$ with a sign opposite that of the Drude result, leading to a suppression of the conductivity. It also has a very sensitive dependence on applied magnetic field, showing a dramatic dependence for weak fields ($H < 100\,\mathrm{G}$), even at very low temperatures for which the effect would be largest in the absence of such a field. In Fig. 1.5 I show the dependence of the total conductivity including the WL correction as a function of both temperature and magnetic field.

In two dimensions the primary dephasing mechanism at very low temperatures is believed to be Nyquist electron-electron scattering, and the dephasing time is

given by [79]

$$\frac{1}{\tau_\phi} = \frac{k_B T}{2\pi D\nu\hbar^2} \ln\left(\pi D\nu\hbar\right), \tag{1.12}$$

where $\nu = m/2\pi\hbar^2$ is the density of states per spin at the Fermi level for a two-dimensional system. A two-dimensional treatment of a disordered metallic plate is justified as long as the dephasing length $L_\phi = \sqrt{D\tau_\phi}$ is larger than the thickness of the plate.

1.2.3 Topology and Berry physics of the BHZ model

When describing phases of matter and the transitions between them, the traditional Landau [80] and Ginzburg-Landau [81] theories describing phases in terms of local order parameters, along with Anderson's insights into classification by means of spontaneous symmetry breaking [82], have been the prevailing wisdom for the better part of a century. For a time it was believed that all phases of matter could be described in this framework, but the discovery of the quantum Hall effect by von Klitzing *et al.* [83] and the recognition that topology was important in this system [84] demonstrated that this was not correct. Indeed, categorizing phases of matter in terms of their topological character represents a fundamentally new paradigm unrelated to symmetry breaking, and cannot be formulated in terms of local order parameters. For a full review of the manifestations of topology and topological classification of states in condensed matter physics, I refer the reader to Hasan and Kane [85] and Qi and Zhang [86].

Instead of a local order parameter, topological phases are characterized by intrinsically nonlocal properties. This includes topological invariants such as the Chern number or a winding number, which must be integers. While it is possible for a system to transition from one topological phase to another, a continuous transition of the type described by Landau theory is impossible because topological properties cannot change continuously; one cannot continuously change an integer index from 1

to 0. Two distinct topological phases can only be connected by a sufficiently "violent" perturbation. One broad class of materials where this is most apparent are the topological insulators (TIs). In these systems, the band structure is gapped everywhere in the bulk, the bands are either completely filled or completely empty, and the relevant topological index is the Chern number of the filled bands. It is impossible to change the Chern number, and therefore to transition between topological phases, without closing the gap.

One important model of a TI is known as the Bernevig-Hughes-Zhang (BHZ) model [87]. The BHZ model describes two-dimensional topological insulators which exhibit the quantum spin Hall effect, first observed experimentally in Hg(Cd)Te quantum wells [88], after the prediction of the theory. An important characteristic of this model for our purposes is that it can be tuned between topologically trivial and nontrivial regimes by changing a single parameter. The model is given by the Hamiltonian

$$H_{\mathrm{BHZ}}(\mathbf{p}) = \begin{pmatrix} \hat{h}(\mathbf{p}) & 0 \\ 0 & \hat{h}(-\mathbf{p})^* \end{pmatrix}, \tag{1.13}$$
$$\hat{h}(\mathbf{p}) = \epsilon(p)\hat{\mathbf{1}} + \mathbf{d}(\mathbf{p}) \cdot \hat{\tau}, \quad \mathbf{d}(\mathbf{p}) = \left(Ap_x, -Ap_y, M(p)\right),$$

where $\epsilon(p) = C - Dp^2$ is the electron-hole asymmetry of the system, $M(p) = M - Bp^2$ is the momentum-dependent Dirac mass, $\hat{\tau}$ is the vector of Pauli matrices, $\hat{\mathbf{1}}$ is the unit matrix, and A, B, C, D, and M are material parameters. (Matching experiment, we will take $A > 0$ and $B < 0$ throughout.) We note that $\epsilon(p)$ is unimportant for all of the properties of the system we will consider, and so we drop it from this point forward. The Hamiltonian acts in the space $\left(|\uparrow, s\rangle, |\uparrow, p\rangle, |\downarrow, s\rangle, |\downarrow, p\rangle\right)^T$, where $\uparrow\downarrow$ labels spin and s, p label atomic orbitals. It is invariant under both time reversal and inversion. The action of time reversal transforms the two blocks into each other, and because they are not otherwise coupled, we will be able to consider just a single

block (half-BHZ model) in order to understand many of the full model's properties. More properties of the symmetries of this model are discussed in Appendix B.1.

For the purposes of examining topological phases it is important that the mass-like parameter M is allowed to take both positive and negative values. For $M = 0$, the mass term vanishes at $p = 0$ and gap closes, connecting a topologically trivial phase and a topologically nontrivial phase for different signs of M.

It is useful to understand the two phases of this model quantitatively from several different perspectives. The vector $\mathbf{d}(\mathbf{p})$ is a map from two-dimensional momentum space (including the point at infinity) to the Bloch sphere, and contains all of the topological properties of the model. I can define the unit vector

$$\begin{aligned}\hat{\mathbf{d}}(\mathbf{p}) = \frac{\mathbf{d}(\mathbf{p})}{|\mathbf{d}(\mathbf{p})|} = \frac{1}{\sqrt{\tilde{p}^2 + (1-\beta\tilde{p}^2)}}\left(\tilde{p}_x,\ \tilde{p}_y,\ \operatorname{sgn} M\,(1-\beta\tilde{p}^2)\right) \\ = \left(\cos\varphi_p \sin\theta_p,\ \sin\varphi_p \sin\theta_p,\ \cos\theta_p\right) \quad (1.14)\end{aligned}$$

where I use the shorthand notation $\tilde{\mathbf{p}} \equiv A\mathbf{p}/|M|$ and $\beta \equiv BM/A^2$, and the azimuthal (φ) and polar (θ) angles in the second line are defined through

$$\cos\varphi_p = \frac{p_x}{p}, \quad \sin\theta_p = \frac{\tilde{p}}{\sqrt{\tilde{p}^2 + (1-\beta\tilde{p}^2)^2}}, \quad \cos\theta_p = \frac{\operatorname{sgn}(M)\,(1-\beta\tilde{p}^2)}{\sqrt{\tilde{p}^2 + (1-\beta\tilde{p}^2)^2}}. \quad (1.15)$$

One can easily show that $\hat{\mathbf{d}}(p=0) = (0, 0, \operatorname{sgn} M)$ while $\hat{\mathbf{d}}(p \to \infty) \to (0, 0, 1)$ since we have taken $B < 0$. Therefore, for $M < 0$ (i.e. $\beta > 0$), $\hat{\mathbf{d}}(\mathbf{p})$ maps momentum space surjectively onto the Bloch sphere, whereas for $M > 0$ ($\beta < 0$) the map does not cover the entire Bloch sphere. The Chern number is equivalent to the number of times the Bloch sphere is fully covered by this map, and so the fact that distinct topological phases are determined by the sign of M is immediately apparent.

The two phases can also be distinguished in several ways by considering the eigenstates of the Hamiltonian. Because the eigenstates and the vector $\hat{\mathbf{d}}(\mathbf{p})$ are two

representations of the same mathematical structure in different spaces, connected by the Clifford algebra of the Pauli matrices, this is not a surprising result but it is worth demonstrating nonetheless. The single-particle spinor eigenstates corresponding to the two bands of the upper block of the BHZ Hamiltonian Eq. (1.13) are[2]

$$|\mathbf{p},+\rangle = \begin{pmatrix} \exp\left[i\frac{s+1}{2}\varphi_{\mathbf{p}}\right]\cos\frac{\theta_{\mathrm{p}}}{2} \\ \exp\left[i\frac{s-1}{2}\varphi_{\mathbf{p}}\right]\sin\frac{\theta_{\mathrm{p}}}{2}, \end{pmatrix}, \qquad |\mathbf{p},-\rangle = \begin{pmatrix} -\exp\left[-i\frac{s-1}{2}\varphi_{\mathbf{p}}\right]\sin\frac{\theta_{\mathrm{p}}}{2} \\ \exp\left[-i\frac{s+1}{2}\varphi_{\mathbf{p}}\right]\cos\frac{\theta_{\mathrm{p}}}{2}, \end{pmatrix} \tag{1.16}$$

where $s \equiv \operatorname{sgn}\beta$. The angles used in parametrizing these states are equivalent to those introduced in Eq. (1.14), and the states for the other 2×2 block of the BHZ Hamiltonian can be generated from these by applying the time reversal operator (see Appendix B.1).

One way to examine the topological phases of the model is by examining the spin textures of the eigenstates. In Fig. 1.6 I plot the projection of these spinors onto the basis states $|\uparrow\rangle = \left(\begin{smallmatrix}1\\0\end{smallmatrix}\right)$ and $|\downarrow\rangle = \left(\begin{smallmatrix}0\\1\end{smallmatrix}\right)$. We see that the textures for the trivial and topological phases in each band are qualitatively different. In the topological phase both eigenstates cover the entire Bloch sphere and correspond to a phase with nonzero Chern number, while in the trivial phase they are primarily polarized along either $|\uparrow\rangle$ or $|\downarrow\rangle$.

These states can also be used to calculate the Chern number of the system as the integral of the Berry curvature [89] of the filled bands over all momentum space. It will also be useful to have the form of the Berry connection and Berry curvature in the BHZ model for the analysis in Chapter 4. Consider the chemical potential to sit within the gap so just the lower band is filled. The Berry connection for the lower band is

$$\mathbf{A}(\mathbf{p}) = i\langle \mathbf{p},-|\,\boldsymbol{\nabla}_p\,|\mathbf{p},-\rangle = \frac{s+\cos\theta_p}{2p}\hat{\boldsymbol{\varphi}}, \tag{1.17}$$

[2]Note that in the topological regime these states are not well defined for the point $\theta = 0$, a manifestation of the obstruction to a single chart of the sphere.

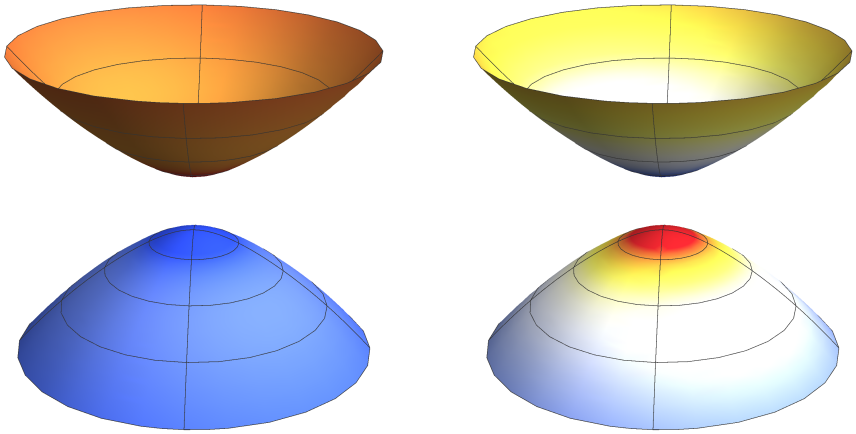

Figure 1.6: The z projection of the spin textures of the eigenstates of the BHZ model, overlayed onto their respective bands. The topologically trivial case ($\operatorname{sgn}\beta < 0$) is on the left and the topologically nontrivial case ($\operatorname{sgn}\beta > 0$) is on the right. We see that in the trivial case, the upper band is polarized primarily along $|\uparrow\rangle$ (red) and the lower band is polarized primarily along $|\downarrow\rangle$ (blue), while in the topologically nontrivial case the spin texture flips from $|\uparrow\rangle$ to $|\downarrow\rangle$ (or vice versa) going from $p = 0$ towards larger p.

where this is written as a vector in polar coordinates, from which is then obtained the corresponding Berry curvature,

$$\boldsymbol{\Omega}(\mathbf{p}) = \boldsymbol{\nabla}_p \times \mathbf{A}_-(\mathbf{p}) = -A^2 \frac{M + Bp^2}{2d(p)^3}\hat{\mathbf{z}} \tag{1.18}$$

$$= \frac{1}{p}\frac{\partial}{\partial p}\left(pA_\varphi(p)\right)\hat{\mathbf{z}} = -\frac{1}{2p}\sin\theta_p \frac{\partial\theta_p}{\partial p}\hat{\mathbf{z}}. \tag{1.19}$$

As a consequence of how it is defined, the Berry curvature is independent of the gauge choice made in writing the Berry connection; redefining the Berry connection up to the gradient of some unspecified smooth function leaves the Berry curvature unchanged, and so quantities obtained using it may have observable consequences. The integral of the Berry curvature over all momentum space gives the Chern

number, which can be easily calculated using spherical coordinates,

$$C_1 = \frac{1}{2\pi}\int d^2p\ \Omega_z(\mathbf{p}) = \frac{1}{2}\int_{\theta_{p\to\infty}}^{\theta_{p=0}} d\theta\ \sin\theta = \begin{cases} 0, & \operatorname{sgn}\beta < 0 \\ 1, & \operatorname{sgn}\beta > 0. \end{cases} \tag{1.20}$$

Here I have used the expressions for the polar angle θ_p in Eq. (1.15) to find that $\theta_{p=0} = \theta_{p\to\infty} = 0$ when $\operatorname{sgn}\beta < 0$, while $\theta_{p=0} = \pi$ and $\theta_{p\to\infty} \to 0$ when $\operatorname{sgn}\beta > 0$. Thus, this more rigorous calculation verifies the intuition obtained by examining the limiting properties of the map $\hat{\mathbf{d}}(\mathbf{p})$ and the spin textures defined by the eigenstates, with the sign of M determining either a trivial or nontrivial Chern number.

In this dissertation I use the BHZ model as a testbed for analyzing how different topological phases affect the optical properties of a system, including the spectrum of excitons formed in the bulk of the material (see Chapter 4).

1.2.4 Superconductivity and the Bardasis-Schrieffer mode

In this final introductory section I focus on the closest analog of excitons within a superconducting system. The existence of internal exciton-like states of the superconducting order parameter was originally proposed by Bardasis and Schrieffer [90], not long after the development of the BCS theory of superconductivity. Now named Bardasis-Schrieffer (BS) modes, these can be thought of as the excitation of Cooper-pairs into states with angular momentum different from their ground state.

The BCS pairing interaction can be expanded in angular momentum channels, or, in a lattice model, in terms of representations of the lattice symmetry group. In two dimensions these channels are parametrized by a single quantum number, and so the interaction is

$$V(\mathbf{k},\mathbf{k}') = \sum_{\ell} g_\ell \chi_\ell(\mathbf{k})\chi_\ell(\mathbf{k}'), \tag{1.21}$$

where g_ℓ is the interaction strength in the ℓ channel, and $\chi_\ell(\mathbf{k})$ is the basis function

for that channel. Typically only the interaction strength in a single channel is sizable and so all others can be discarded, but in models where multiple g_ℓ's are of comparable strength they must all be retained. We can now more precisely define BS modes as gapped, undamped, in-gap fluctuations of the superconducting order parameter in these subdominant pairing channels.

Typically fluctuations in a d-wave channel are considered about an s-wave superconducting ground state, and in this case the BS mode is the d-wave mode that fluctuates with a $U(1)$ phase of $\pi/2$ relative to the phase of the s-wave condensate. These modes have long been sought experimentally but are difficult to detect because they do not couple to electromagnetism at the level of linear response; their detection has only been recently reported through Raman spectroscopy in iron-based materials [91–93]. A variety of multiband effects are known to complicate their identification [94], which we will not consider for simplicity.

Chapter 2: Nonanalytic behavior of the Casimir force across a Lifshitz transition

2.1 Overview

In this chapter, we consider how the Casimir force between two thin films is modified a system is tuned across a Lifshitz transition – an extreme case of Fermi surface reconstruction in an electronic material. This chapter is largely taken from the author's paper [36], originally published in Physical Review B, ©American Physical Society, 2014. Atypically for the Casimir effect, we find that as the system is driven through this transition by tuning a magnetic field, the Casimir force is both nonanalytic and nonmonotonic as a function of the field strength. Our model involves a thin layer of indium antimonide (or another semiconductor with a large g factor, as discussed below) and could be experimentally realized in the common experimental setup for Casimir measurements as shown in Fig. 2.1.

In the remainder of this chapter we first define our model and show how it undergoes such a transition. We then find the current-current correlation function from linear response theory after minimally coupling our Hamiltonian to light in order to calculate the Casimir energy. Using this expression, we numerically integrate to obtain the Casimir force as we tune our original Hamiltonian through a Lifshitz transition.

2.2 Model of Spin-Orbit Coupled Plates

Others have considered the implications of considering two-dimensional plates instead of thick slabs in calculations of the Casimir effect [95–97], but similar to the particular case of graphene [98–100], our model requires a more microscopic

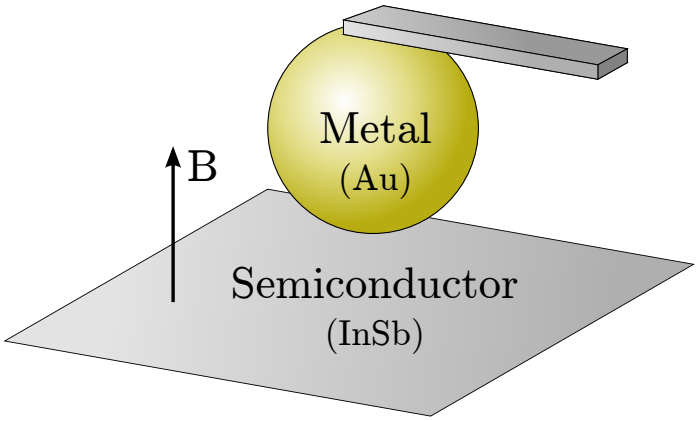

Figure 2.1: Configuration often used in experimental measurements of the Casimir force [11] showing a gold-coated sphere suspended from a cantilever above an InSb plate. We first consider a lower plate of indium antimonide with an applied magnetic field. Afterward we also consider both a plate and sphere composed of indium antimonide, again with applied magnetic field.

approach (see the Appendix of Ref. [36]). We consider the Casimir force at zero temperature between two parallel plates where at least one is modeled as a two-band spin-orbit-coupled material (sufficiently thin to be considered quasi-two-dimensional) with a fixed chemical potential and tunable Zeeman splitting due to an external magnetic field. (When considering only one spin-orbit-coupled plate, the other is a metallic plate, modeled as a clean free electron gas.) The Zeeman field tunes a gap in this two-band material and can cause the Fermi surface of one of the bands to form or collapse as it is pushed to different energies around the Fermi level. This is the simplest realistic model exhibiting a Lifshitz transition. At these transition points, the Casimir force between the two plates experiences a kink, as seen in Fig. 2.2.

This could be experimentally measured with the usual plate and sphere geometry as seen in Fig. 2.1. While we consider the parallel plate scenario, our calculations can be generalized to the sphere-plate geometry by using the proximity force approximation [2] without damage to the nonanalyticity we observe in the Casimir force.

We consider the single-particle effective Hamiltonian for one electron in the

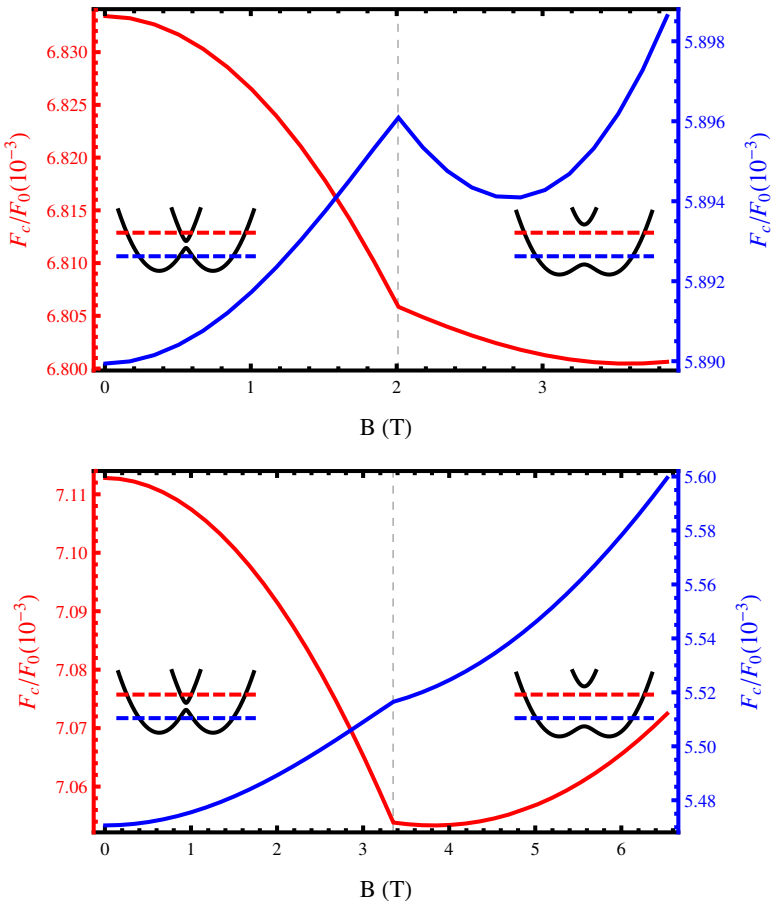

Figure 2.2: The Casimir force F_c normalized by the ideal conductor value between one semiconductor plate and one metallic plate separated by $a = 50\,\text{nm}$ as a function of applied magnetic field. The red plot (left axis) corresponds to $\mu > 0$, and the blue plot (right axis) corresponds to $\mu < 0$. The upper plot uses $\mu = \pm 6\,\text{meV}$ and the lower uses $\mu = \pm 10\,\text{meV}$. The insets show the band structure above and below the transition point (marked with a dashed line) along with the two fixed values of the Fermi energy.

conduction bands of the semiconductor,

$$\hat{H} = \frac{k^2}{2m^*} - \mu + \beta(\hat{\sigma}_x k_x - \hat{\sigma}_y k_y) + V_z \hat{\sigma}_z, \tag{2.1}$$

which has eigenvalues

$$\xi^{\pm}(k) = \frac{k^2}{2m^*} - \mu \pm \sqrt{V_z^2 + \beta^2 k^2}, \tag{2.2}$$

where m^* and μ are the conduction band effective mass of the electron and chemical potential. The coefficient β is the strength of the Dresselhaus spin-orbit coupling, and $\hat{\sigma}_i$ are the Pauli matrices. The factor V_z is the induced Zeeman splitting, given by $V_z = \mu_B g^* B$, where μ_B is the Bohr magneton, g^* is the material's g factor, and B is an applied magnetic field.

For all calculations we assume that this Hamiltonian provides a simple model of the relevant bands of the material indium antimonide, for which $m^* = 0.014 m_0$, where m_0 is the free electron mass, and $\beta = \gamma \langle k_z^2 \rangle \simeq \gamma \left(\frac{\pi}{d}\right)^2$ [101], where d is the thickness of the plate and $\gamma = 760.1\,\mathrm{eV\AA}^3$ is the intrinsic Dresselhaus parameter for the material. We consider InSb plates that are six lattice constants thick, i.e. $d = 6 \times 0.6479\,\mathrm{nm} = 3.89\,\mathrm{nm}$. The plates may still be considered effectively two-dimensional as long as the energy needed to excite higher electron modes in the confined direction is much larger than the energy required to excite the two lowest bands modeled here. Additionally, since the g factor of InSb is $g^* = -51.6$ we can also neglect the orbital coupling of the electrons directly to the external magnetic field as well as the effect of the magnetic field on the metallic plate when it is considered [102].

This simple model neglects virtual excitations in the confined direction as well as changes in bulk parameters due to confinement, band bending, or emergence of other spin-orbit effects (e.g., Rashba spin-orbit coupling). The parameters are at

least of the same order of magnitude, and other spin-orbit terms just modify the geometry of the Fermi surface. At worst, these complications and effects due to the crystalline structure of InSb could affect the quantitative features but should not the qualitative features.

For $\mu > |V_z|$ there are two bands crossing the Fermi energy. As $|V_z|$ is increased for fixed μ the occupation of the upper band decreases until the Fermi surface disappears entirely when $|\mu| = |V_z|$, i.e. the electron pocket defined by that Fermi surface disappears. Increasing the Zeeman splitting further, the Fermi energy lies within the gap and only the lower band crosses the Fermi level, giving a single Fermi surface. This represents the Lifshitz transition for $\mu > 0$, and is shown with the red dashed line in the insets of Fig. 2.2.

If $m^*\beta^2 > |V_z|$ the lower band has a "Mexican hat" form, with a local maximum at $k = 0$ and a ring of minima at finite k, and a similar scenario can be considered for $\epsilon_{\min} < \mu < -|V_z|$, where $\epsilon_{\min}$ is the minimum energy of the band. In this case, the lower band crosses the Fermi energy for two distinct values of k, producing two Fermi surfaces, the inner one enclosing a hole pocket. Again, increasing $|V_z|$ for fixed μ leads to a shrinking of the inner Fermi surface until it disappears completely at the point when $|\mu| = |V_z|$. For larger Zeeman splitting, the Fermi energy again lies within the gap and there is a single Fermi surface. This scenario for $\mu < 0$ is shown with the blue dashed line in the insets of Fig. 2.2.

The disappearance of a Fermi surface by changing V_z in these two scenarios are simple examples of a Zeeman-driven Lifshitz transition. Since these transitions occur at a specific value of $|V_z|$, regardless of the sign of V_z, the direction of the applied magnetic field is unimportant. For this reason, we always assume $V_z > 0$ for simplicity. We also denote the magnetic field strength needed to reach the Lifshitz transition point as $B_L = \frac{|\mu|}{g\mu_B}$.

We determine the bare correlation function using the current operator, $j_i(x) =$

$\psi^\dagger(x)\frac{\partial \hat{H}[A]}{\partial A_i(x)}\psi(x)$, where

$$\hat{H}[A] = \frac{ie}{2m^*}\left(A_i\partial_i - \overleftarrow{\partial}_i A_i\right) - e\beta\left(\hat{\sigma}_x A_x - \hat{\sigma}_y A_y\right) \tag{2.3}$$

is the Hamiltonian given in Eq. (2.1) after minimal coupling, and the notation $\overleftarrow{\partial}_i$ means a derivative acting to the left. The correlation function is then expressed in terms of the current as

$$\Pi_{ij}(x,x') = \langle -\delta(x-x')\delta_{ij}\partial_{A_i} j_i(x) + j_i(x)j_j(x')\rangle\Big|_{A=0}, \tag{2.4}$$

where $\langle\cdots\rangle$ represents averaging over the ground state [103]. In the case of a weakly correlated system we can use the approximation that the Casimir effect is determined by the local current-current response functions; i.e., we need to consider only the $q = 0$ limit of $\hat{\Pi}$ since nonlocal behavior is screened out. Equivalently, this is a simple extension of the commonly considered plasma model to the case of a spin-orbit-coupled Hamiltonian. Furthermore, coupling of the spin to the magnetic fluctuations of the vacuum field does not need to be considered. In this limit, the correlation function for the spin-orbit-coupled plates has the form

$$\hat{\Pi}(i\omega) = -\frac{e^2}{h}\begin{pmatrix} \Pi_L(i\omega) & \Pi_H(i\omega) \\ -\Pi_H(i\omega) & \Pi_L(i\omega) \end{pmatrix}, \tag{2.5}$$

where e^2/h is the quantum of conductance,

$$\Pi_H(i\omega) = V_z\left[\cot^{-1}\left(\frac{\omega}{2\epsilon^+}\right) - \cot^{-1}\left(\frac{\omega}{2\epsilon^-}\right)\right] \tag{2.6}$$

$$\Pi_L(i\omega) = \mu\left[\Theta(\mu - |V_z|) + \Theta(\mu + |V_z|)\right] + \frac{\epsilon^+ - \epsilon^-}{2} + \frac{\omega^2 - 4V_z^2}{4V_z\omega}\Pi_H(i\omega)$$

and $\epsilon^{\pm}$ are the positive square roots of

$$(\epsilon^{\pm})^2 = V_z^2 + \max\left\{0, 2m^*\beta^2(\mu + m^*\beta^2)\left[1 \pm \sqrt{1 - \frac{\mu^2 - V_z^2}{(\mu + m^*\beta^2)^2}}\right]\right\}. \tag{2.7}$$

2.3 Results for the Casimir Force

We use a microscopic quantum field theoretic method to calculate the Casimir energy at zero temperature in terms of the current-current correlation functions of the two electron systems under consideration and virtual photons in the three-dimensional vacuum between them. Summing up the appropriate diagrams, the Casimir energy at zero temperature for parallel 2D plates separated by a distance a is given by [36]

$$\mathcal{E}_c(a) = \frac{1}{4\pi^2}\int_0^\infty dq_\perp\, q_\perp \int_0^{q_\perp} d\omega\ \mathrm{tr}\ln\left[\hat{\mathbf{1}} - \hat{\tilde{\Pi}}_A \hat{D}(a)\hat{\tilde{\Pi}}_B \hat{D}(a)\right], \tag{2.8}$$

where $\hat{D}$ is the photon propagator and $\hat{\tilde{\Pi}}_i$ is the current-current correlation function for plate i, dressed by interactions with photons. We have suppressed the dependence of all functions on $q_\perp$ and the imaginary frequency $i\omega$. We also use the Coulomb gauge with no scalar potential $\phi = 0$, so the relevant components of the photon propagator have the form

$$\hat{D}(q_\perp, i\omega, z) = \frac{\hbar}{2}\begin{pmatrix} \frac{q_\perp}{\omega^2} & 0 \\ 0 & \frac{1}{q_\perp} \end{pmatrix} e^{-q_\perp|z|}. \tag{2.9}$$

The dressed current-current correlation function can be expressed in terms of the bare correlation function $\hat{\Pi}$ as

$$\hat{\tilde{\Pi}} = \left[\hat{\mathbf{1}} - \hat{\Pi}\hat{D}(z=0)\right]^{-1}\hat{\Pi}, \tag{2.10}$$

which accounts for dynamical screening of photons in the random-phase approximation (RPA).

Taking the derivative of the Casimir energy Eq. (2.8) with respect to the separation between the plates a gives an expression for the Casimir force. We can then integrate this expression numerically for fixed separation a and Fermi energy μ, while varying $|V_z|$, which in principle can be done by varying an applied magnetic field. For numerical work, we take $a = 50\,\text{nm}$ in our calculations. We consider two Fermi energies, $\mu = \pm 6\,\text{meV}$ and $\pm 10\,\text{meV}$, which, using the g-factor of InSb, give that the magnetic fields needed to reach the transition are $B_L = 2$ and $3.35\,\text{T}$. For all numerical results we scale the strength of the Casimir force F_c by the strength of the Casimir force between ideal conducting plates, $F_0 = -\hbar c\pi^2/240a^4$, as calculated for the same plate separation. We consider only a single plate separation because the dependence on this parameter closely follows the usual $1/a^4$ dependence for the Casimir force, with the magnitude of the force increasing as the plates are brought closer together. Furthermore, the qualitative nature of the effect we are primarily focused on is unaffected by changing this distance.

As a point of comparison, we first consider the Casimir force between two metallic plates subject to a Zeeman field, each described by (2.1) with $\beta = 0$. In this case, the Casimir force as a function of magnetic field is shown in Fig. 2.3. As the magnetic field is tuned and the chemical potential is kept fixed, the Fermi surface changes by the removal of an electron pocket, depicted schematically in Fig. 2.4. In Fig. 2.3, we see that for $B < B_L$ the Casimir force is constant with varying B, since the carrier density of the material, which in this case is the only free parameter determining the value of $\hat{\Pi} = -\frac{e^2}{h}\left[2\mu\,\Theta(\mu - |V_z|) + (\mu + |V_z|)\,\Theta(|V_z| - \mu)\right]$, is constant in this region. As the upper band is raised above the Fermi level, the closing of its corresponding Fermi surface produces a kink in the Casimir force, above which the magnitude of the force increases with B, consistent with the increase in the carrier density in this

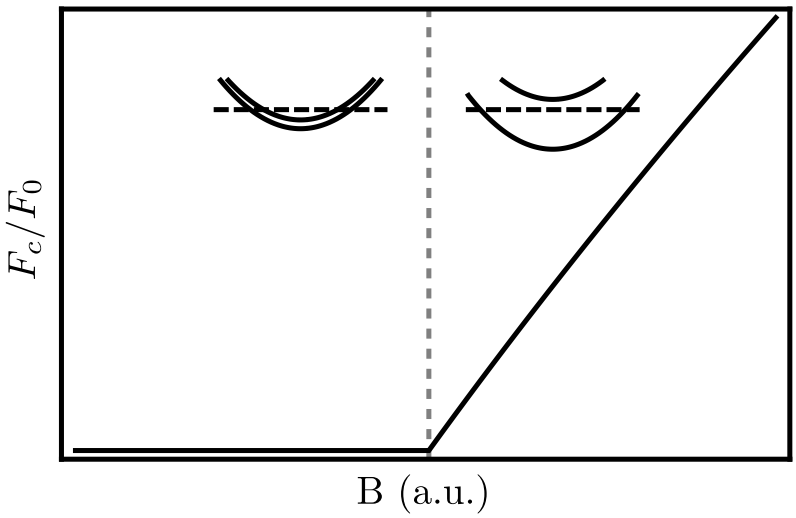

Figure 2.3: The Casimir force F_c normalized by the ideal conductor value F_0 between two metallic plates at a fixed separation as a function of the applied magnetic field. The Lifshitz transition occurs at the magnetic field strength indicated by the dashed vertical line. The insets show the band structure above and below the transition along with the fixed value of the Fermi energy. With a large Fermi energy and small electronic g factor (≈ 2), a prohibitively large magnetic field is needed to reach the transition.

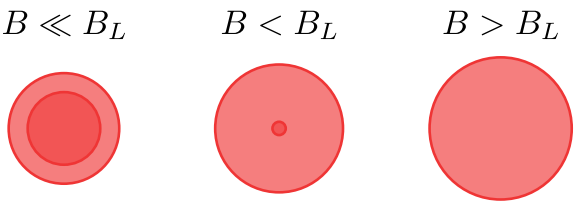

Figure 2.4: A schematic picture of the Fermi surfaces in 2D k space as a function of magnetic field for constant chemical potential μ. A Lifshitz transition occurs between the second and third pictures, when the smaller electron-like pocket vanishes.

region. This simple system has a critical field $B_L = \frac{|\mu|}{g\mu_B}$ which would unreasonably large to produce in a real experiment (on the order of 10000 T) due to large Fermi energies and small g factors in typical metals.

Spin-orbit-coupled semiconductors, on the other hand, may have small Fermi energies and large g factors, leading to more experimentally accessible values of B_L. The Casimir force as a function of the magnetic field is presented in Fig. 2.2 for the case of one metallic plate and one InSb plate and in Fig. 2.5 for the case of two InSb plates. The relevant numerical quantities for these plots are given in Tables 2.1

Table 2.1: Numerical results from the case of the Casimir force between one metallic plate and one InSb plate, all in units of $F_0 = -\hbar c\pi^2/240a^4$ and multiplied by a factor of 10^3. The first column gives the value of the force at the transition. The second column gives the change in the force from $B = 0$ to the transition. The last column gives the jump in the derivative of the force with respect to the applied magnetic field across the transition, giving a measure of the severity of the kink.

μ (meV)	$\frac{F_c(B_L)}{F_0} \times 10^{-3}$	$\frac{F_c(B_L)-F_c(0)}{F_0} \times 10^{-3}$	$\frac{dF_c}{dB}\|_{B=B_L^+} - \frac{dF_c}{dB}\|_{B=B_L^-}$ (F_0/T)
6	6.806	-0.02756	0.0212
10	7.054	-0.0589	0.0326
-6	5.896	0.0061	-0.0097
-10	5.516	0.0458	-0.0125

Table 2.2: The same as Table 2.1 but for the case of two identical InSb plates.

μ (meV)	$\frac{F_c(B_L)}{F_0} \times 10^{-3}$	$\frac{F_c(B_L)-F_c(0)}{F_0} \times 10^{-3}$	$\frac{dF_c}{dB}\|_{B=B_L^+} - \frac{dF_c}{dB}\|_{B=B_L^-}$ (F_0/T)
6	5.138	-0.0291	0.0200
10	5.346	-0.0619	0.0310
-6	4.367	-0.0020	-0.0056
-10	4.041	0.0192	-0.0035

and 2.2, including the chemical potential μ, the value of the force, the change of force from the zero magnetic field value, and the change of the slope characterizing the kink. We see from Fig. 2.2 and Fig. 2.5 that the sign and value of the chemical potential has a strong influence on the magnetic field dependence of the Casimir force. For positive values of μ (red curves), the Fermi surface behaves similar to that seen in Fig. 2.4. In this case the behavior of the Casimir force above and below the transition is similar in both systems. In particular, the force decreases in magnitude as the magnetic field strength is increased towards the transition and the force increases as the field increases above the transition for sufficiently large values of B. This increase at large B is irrespective of Fermi energy and it arises because $V_z \gg \beta\sqrt{2m^*|\mu|}$, leading to a suppression of the spin-orbit-coupling term and a crossover to simple metallic behavior.

For negative values of μ (blue curves), the Fermi surface possesses a hole pocket that closes at the critical magnetic field, as shown in Fig. 2.6. Due to the disappearance of this Fermi surface the behavior of the Casimir force is different in the two

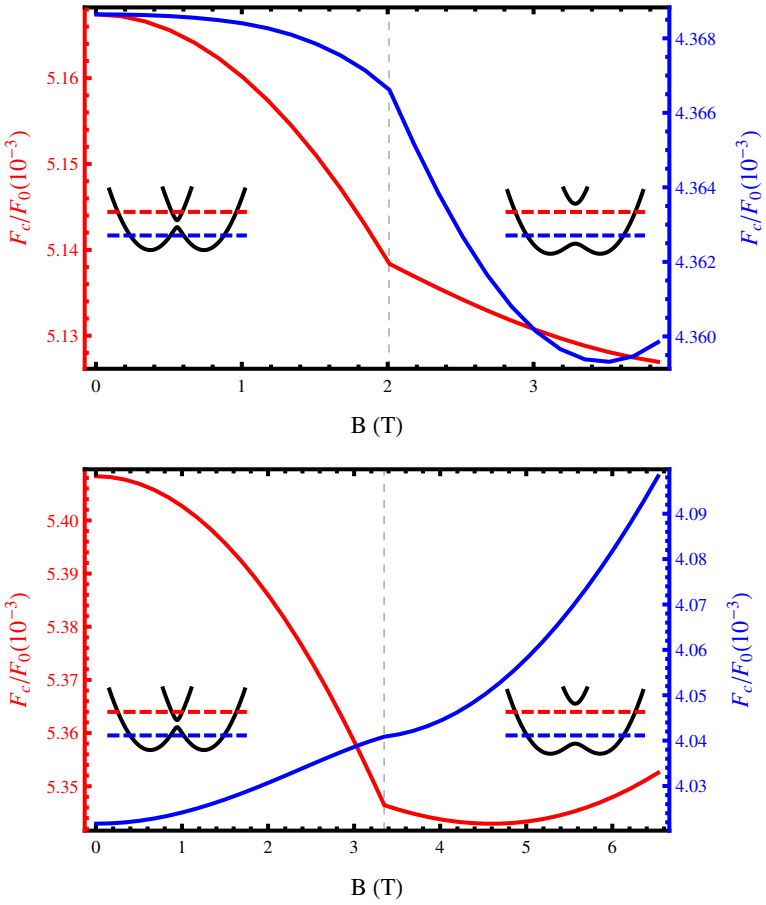

Figure 2.5: The Casimir force F_c normalized by the ideal conductor value F_0 between two semiconductor plates separated by $a = 50\,\text{nm}$ as a function of applied magnetic field. The red curve (left axis) corresponds to $\mu > 0$, and the blue curve (right axis) corresponds to $\mu < 0$. The upper plot uses $\mu = \pm 6\,\text{meV}$ and the lower plot uses $\mu = \pm 10\,\text{meV}$. The insets show the band structure above and below the transition point along with the two fixed values of the Fermi energy.

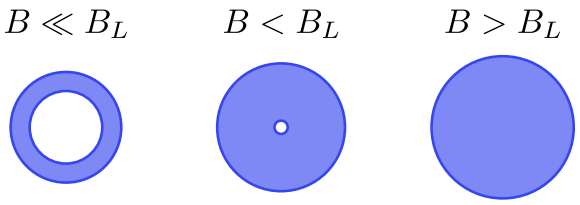

Figure 2.6: Illustration of the Fermi surfaces in 2D k space as a function of magnetic field for constant chemical potential μ, here for the lower band of the spin-orbit coupled model. A Lifshitz transition occurs between the second and third pictures, when the hole-like pocket vanishes and changes the Fermi surface from an annulus to a disk.

systems. When considering one InSb plate and one metallic plate, the force increases with increasing B below the Lifshitz transition for all values of μ considered, and then, with a kink at the transition, increases above the transition for a sufficiently strong magnetic field (again, in a crossover to the simple metal case). In the system composed of two InSb plates, there is no obvious trend in the Casimir force except that, again, for a strong enough magnetic field the force increases with increasing B. For fields below the transition, however, the force may increase or decrease in strength as a function of B, depending on the value of μ.

The main feature in all of these plots is the sharp kink that occurs at the Lifshitz transition. In principle, this feature should be discernible even considering the effects of temperature and a substrate, which would tend to smooth out the dependence of the force. We expect the features to remain for temperatures much less than the energy of the gap at the transition point (i.e. the chemical potential): 70 K and 116 K for chemical potentials of 6 meV and 10 meV, respectively. Additionally, as long as the substrate for either the InSb or Au is a poor conductor, nonmagnetic, and does not experience an electronic transition in the range of magnetic fields needed to reach the Lifshitz transition, then we would expect it to have at most a small effect on our results, and not to fundamentally change the nature of the kink feature.

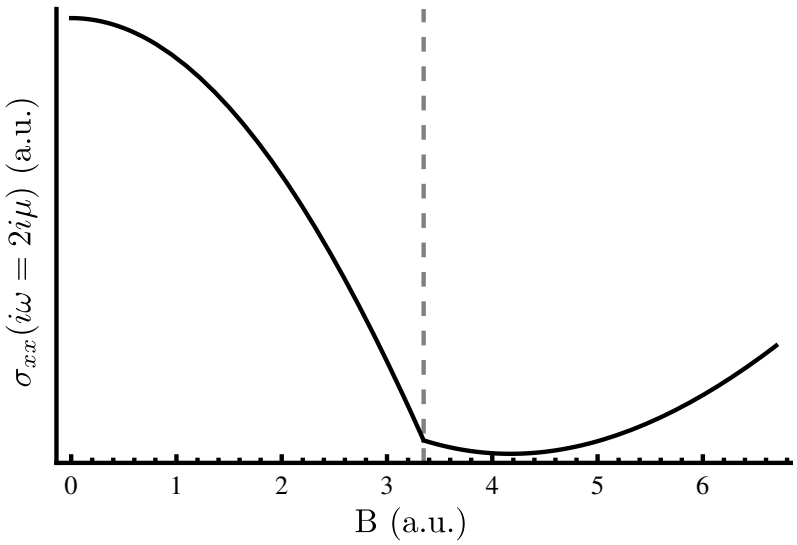

Figure 2.7: The imaginary frequency longitudinal conductivity of the InSb plate at $i\omega = 2i\mu$ for $\mu = 10\,\text{meV}$ as a function of the applied magnetic field. The Lifshitz transition point is indicated with a dashed line.

2.4 Conclusions

The dependence of the Casimir force on the magnetic field strength in these systems can be understood by examining the imaginary frequency optical conductivities of the InSb plates at a fixed nonzero frequency; since in our model the plates have no disorder, there will also be no dissipation and the longitudinal dc conductivity is infinite. This also means that the longitudinal and Hall conductivities at finite frequency have a discontinuity in their derivatives with respect to B at the point where $|\mu| = V_z$, just as we find with the Casimir force (the fourth columns of Tables 2.1 and 2.2). The overall trend in the longitudinal conductivity, shown in Fig. 2.7, mimics the behavior of the Casimir force for all positive Fermi energies—both decreasing in magnitude below the transition, then decreasing less drastically directly above the transition until reaching a minimum and finally increasing with B. This suggests that the Hall conductivity contribution to the Casimir effect, arising due to interband spin-orbit interactions, which are stronger when the bands are closer in energy (i.e. small V_z), works to suppress the strength of the Casimir force. For

smaller values of the chemical potential the bands are closer together in energy at the point of the Lifshitz transition, and so interband effects have a more significant impact than for larger values of μ. Additionally, these effects are stronger in the system with two InSb plates, as would be expected if they were the result of spin-orbit coupling.

In conclusion, tuning through a Lifshitz transition in a spin-orbit-coupled material causes a nonanalytic kink in the Casimir force while the microscopic properties of the model control the nature and severity of the kink. We argue that the Hall conductivity serves to suppress the Casimir force, which affects the nonanalyticity as well. We expect similar features to be found in other materials with such transitions – particularly due to the change in the carrier concentration across such a transition. This is one way in which precision Casimir force experiments could be used as a probe of nontrivial electronic properties or transitions. This analysis is not exclusive to the particular semiconductor considered here; not only could the Casimir effect be used to probe Lifshitz transitions in other materials, but it could conceivably be used to detect other phenomena such as the Fermi surface reconstruction and the superconducting transition in cuprates as well as disorder-driven phenomena such as localization.

Chapter 3: Quantum interference phenomena in the Casimir effect

3.1 Overview

This chapter is largely taken from the author's paper [104], originally published in Physical Review A, ©American Physical Society, 2015. There is a continuing debate in the Casimir literature over which of two models best describes metallic plates in calculations of the Casimir effect. In this chapter we propose a way to test the validity of one of these models, which could provide a clear answer to this long standing question. Our method relies on the phenomenon of weak localization (WL), which is only observed in one- and two-dimensional disordered metallic systems, as described in Sec. 1.2.2. WL causes the conductivity of these systems to be strongly dependent on temperature and externally applied magnetic fields at low temperatures. We calculate how this dependence translates to the Casimir effect, finding that the Casimir force will likewise manifest a strong sensitivity to temperature and magnetic field, as long as disorder processes are relevant in such calculations.

A fundamental assumption of the WL effect is that electronic motion in the system is diffusive in nature, and its contribution to conductivity is calculated as a correction to the Drude model. Therefore, any modification to the Casimir effect we calculate as a result of including WL would apply only to a diffusive model of metallic plates and not to a ballistic model; a sensitive experimental test of the effects of WL on the Casimir effect would provide a clear indication of whether a diffusive picture of electronic motion correctly describes the physics of real electrons in Casimir experiments. The experiment we propose is very similar to a typical experimental setup used to measure the Casimir effect, as depicted in Fig. 3.1, with a gold-coated sphere suspended from a cantilever over a flat metallic plate. To test

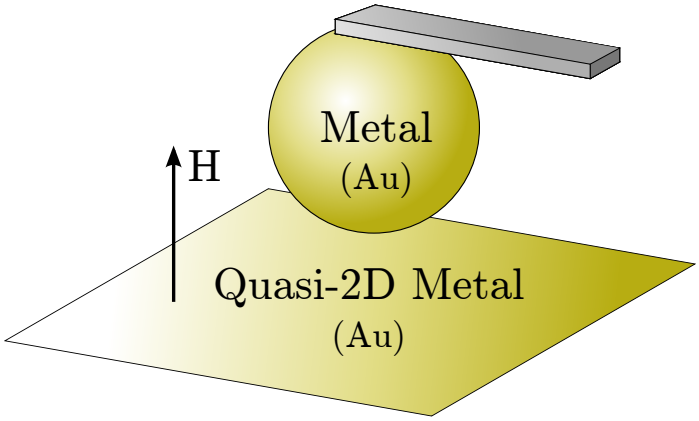

Figure 3.1: Configuration typically used in experimental measurements of the Casimir force, a gold-coated sphere above a planar metallic plate. Here we show the sphere suspended from a cantilever and consider a lower plate of very thin metal with a weak applied perpendicular magnetic field.

the results presented here, the only modification to the geometry of this typical setup would be to ensure this flat plate be a quasi-two-dimensional layer in order for WL to occur.

We note that the theory behind the use of a diffusive model relies upon performing an average over all realizations of the disorder potential in the material. However, if the disorder average is done at the level of linear response instead of the Casimir energy itself, then all effects from, for example, the nonuniformity of physical disorder realizations are neglected. While exact calculation of these neglected effects is impossible, it is possible to estimate the size of their impact on the Casimir force, and whether it is a valid approximation to ignore them when finding the Casimir energy.

3.2 Weak localization in the Casimir effect

To explore the possible effect of WL on the Casimir effect, we consider a system consisting of two flat parallel plates: one thick plate we assume to be well-described by the Drude model and one two-dimensional plate described by the Drude model with an additional "correction" accounting for the effect of weak localization. With

an experimental setup in the typical plate-sphere geometry, as shown in Fig. 3.1, the gold layer on the sphere is thick enough to be most accurately described as a three-dimensional material. Since the effect of WL is insignificant in 3D systems, especially compared to 2D films, we only need to consider the WL effect in the 2D plate. For comparison we also consider the Casimir force between two plasma plates and between two Drude plates without the WL correction. The latter also gives the expected behavior of the system including the WL correction for high magnetic fields, which kill WL effects. In these comparison cases we consider the same geometry, with one thick plate and a parallel 2D plate.

To calculate the Casimir force in these systems we start from the well-known Lifshitz equation for the Casimir energy density at finite temperature [105],

$$\mathcal{E}_c(a) = k_B T {\sum_{\omega_m}}' \int \frac{d^2q}{(2\pi)^2} \left[\ln\left(1 - r_{\mathrm{TM}}^{(1)} r_{\mathrm{TM}}^{(2)} e^{-2\sqrt{q^2+\omega_m^2}a}\right) + \ln\left(1 - r_{\mathrm{TE}}^{(1)} r_{\mathrm{TE}}^{(2)} e^{-2\sqrt{q^2+\omega_m^2}a}\right)\right], \tag{3.1}$$

which can be obtained by expanding the free energy of the two-plate and photon system. In this expression, $\sum'$ again denotes a sum over positive Matsubara frequencies $\omega_m = 2\pi m k_B T$, counting the $m = 0$ term with half weight. The functions $r_{\mathrm{TM}}^{(i)}$ and $r_{\mathrm{TE}}^{(i)}$ are the reflection coefficients of plate i for the two polarizations of light. The subscript TM refers to the transverse-magnetic polarization, where the magnetic field is perpendicular to the plane of incidence, and similarly for TE with the electric field. The reflection coefficients depend on both in-plane momentum q and the Matsubara frequency, and may also depend on parameters of the system such as the applied magnetic field H and temperature.

The reflection coefficients can be written explicitly in terms of the dielectric functions of the plates, $\epsilon_i(i\omega_m)$, or alternatively in terms of the electromagnetic linear response functions of the plates, $\Pi_i(i\omega_m)$, which are related to the dielectric

functions as

$$\epsilon(i\omega_m) = \begin{cases} 1 - \Pi^{2D}(i\omega_m)\delta(z)/\omega_m^2 & \text{for 2D systems} \\ 1 - \Pi(i\omega_m)/\omega_m^2 & \text{for 3D systems.} \end{cases} \tag{3.2}$$

The reflection coefficients have the forms

$$\begin{aligned} r_{\mathrm{TM}}^{\mathrm{2D}}(q, i\omega_m) &= \frac{\Pi^{\mathrm{2D}}(i\omega_m)}{\Pi^{\mathrm{2D}}(i\omega_m) - \frac{2\omega_m^2}{q_\perp}} \\ r_{\mathrm{TE}}^{\mathrm{2D}}(q, i\omega_m) &= \frac{\Pi^{\mathrm{2D}}(i\omega_m)}{\Pi^{\mathrm{2D}}(i\omega_m) - 2q_\perp} \end{aligned} \tag{3.3}$$

for two-dimensional plates, where $q_\perp = \sqrt{q^2 + \omega_m^2}$. For very thick three-dimensional metallic plates (thickness $d \gg a$, we take $d \to \infty$), the reflection coefficients have the forms

$$\begin{aligned} r_{\mathrm{TM}}^{\mathrm{3D}}(q, i\omega_m) &= -\frac{\sqrt{q_\perp^2 - \Pi(i\omega_m)} - q_\perp + \frac{q_\perp}{\omega_m^2}\Pi(i\omega_m)}{\sqrt{q_\perp^2 - \Pi(i\omega_m)} + q_\perp - \frac{q_\perp}{\omega_m^2}\Pi(i\omega_m)} \\ r_{\mathrm{TE}}^{\mathrm{3D}}(q, i\omega_m) &= -\frac{\sqrt{q_\perp^2 - \Pi(i\omega_m)} - q_\perp}{\sqrt{q_\perp^2 - \Pi(i\omega_m)} + q_\perp}. \end{aligned} \tag{3.4}$$

The Casimir force is found by substituting Eqs. (3.3) and (3.4) into Eq. (3.1) and taking the derivative with respect to the plate separation a.

From a microscopic viewpoint the only inputs into Eq. (3.1) are the electromagnetic linear response functions Π for the two plates, which contain all necessary electromagnetic properties for computing the Casimir force. For disordered plates in the Drude model we have

$$\Pi^{\mathrm{Drude}} = -\frac{ne^2}{m^*}\frac{\omega_m}{\omega_m + 1/\tau}. \tag{3.5}$$

The WL correction for the two-dimensional plate given by the Hikami-Larkin-

Nagaoka formula [74, 75], given in Eq. 1.11,

$$\delta\Pi(i\omega_m, T, H) = -\frac{e^2|\omega_m|}{2\pi^2\hbar}\left[\psi\left(\frac{1}{2}+\frac{\hbar}{4eHD\tau_\phi(T)}\right)-\ln\left(\frac{\hbar}{4eHD\tau}\right)\right]. \tag{3.6}$$

For the plasma model, the response function of the plates is simply given by the $\tau \to \infty$ limit of the Drude response, i.e. $\Pi^{\text{plasma}} = -ne^2/m^*$.

We calculate the Casimir force for three different systems, which each have one thick plate and one 2D plate: (i) both plasma plates, (ii) both Drude plates, and (iii) one thick Drude plate and one 2D Drude plate including the weak localization correction term. In each of these systems we fix the plate separation at $a = 250\,\text{nm}$ and calculate the Casimir force as a function of either temperature or applied magnetic field. In all cases, we will assume the system remains in the low-temperature regime where the dephasing time is given by

$$\tau_\phi = \left[\frac{k_B T}{2\pi D\nu\hbar^2}\ln\left(\pi D\nu\hbar\right)\right]^{-1}. \tag{3.7}$$

In this expression $\nu = m^*/2\pi\hbar^2$ is the density of states per spin at the Fermi level. Additionally, we set the elastic mean free path of the electrons in disordered plates to be $l = 15\,\text{nm}$ and the Fermi energy and effective electron mass to be those of gold: $\epsilon_F = 5.53\,\text{eV}$ and $m^* = 1.10m_0$, where m_0 is the free-electron mass [106]. We normalize all Casimir forces by the ideal conductor result for the Casimir force $F_0 = -\hbar c\pi^2/240a^4$, with $a = 250\,\text{nm}$. At the temperatures we consider, between $0.1\,\text{K}$ and $5\,\text{K}$, and with these parameters, the dephasing length in the thin film given by Eq. (3.7) is about half a micron or larger, so in an experimental realization of this system a thin film described by these parameters would need to be much thinner than this in order to observe the effects we are examining here.

We find qualitatively different behavior between the Drude and plasma model results when accounting for the effect of weak localization. The Casimir force between

plasma plates has no dependence on the strength of the applied magnetic field, at least for such weak fields as we consider here, and only a very weak dependence on temperature in this low-temperature regime—the change of the normalized force from 10 K to 0.1 K is a decrease of 1.7×10^{-4}. In stark contrast, the Casimir force when considering a disorded plate with WL shows both a highly nontrivial dependence on weak applied magnetic field at low temperatures, shown in Fig. 3.2, and also a sharp decrease with decreasing temperature when no magnetic field is present, shown in Fig. 3.3.

The effects of both temperature and magnetic field are not surprising when considering the Casimir force as a function of the conductivity of the plates. Compare the dependence of the conductivity in Fig. 1.5 with Figs. 3.2 and 3.3. The strong dependence of the Casimir force on both temperature and magnetic field strongly mirrors the dependence of the conductivity [77, 78]. Indeed, we find that applying a magnetic field of only $H = 40\,\mathrm{G}$ perpendicular to the plates is enough to weaken the suppression of the force by approximately 40% at 0.1 K, the lowest temperature we consider.

At $T = 0.1\,\mathrm{K}$ and $H = 0\,\mathrm{G}$ we find that the inclusion of the WL correction suppresses the Casimir force by 11% compared to the value calculated without the WL correction. At this temperature and magnetic field, the change in the Casimir force from including the WL correction is larger in magnitude than the difference in the Casimir forces predicted by the plasma model and naive Drude model. Examining Fig. 3.2 at $T = 0\,\mathrm{K}$ we find

$$\frac{F_c^{\mathrm{Drude}} - F_c^{\mathrm{WL}}}{F_c^{\mathrm{plasma}} - F_c^{\mathrm{Drude}}} = 1.14, \tag{3.8}$$

which suggests that the effect is large enough to be measurable at this low temperature.

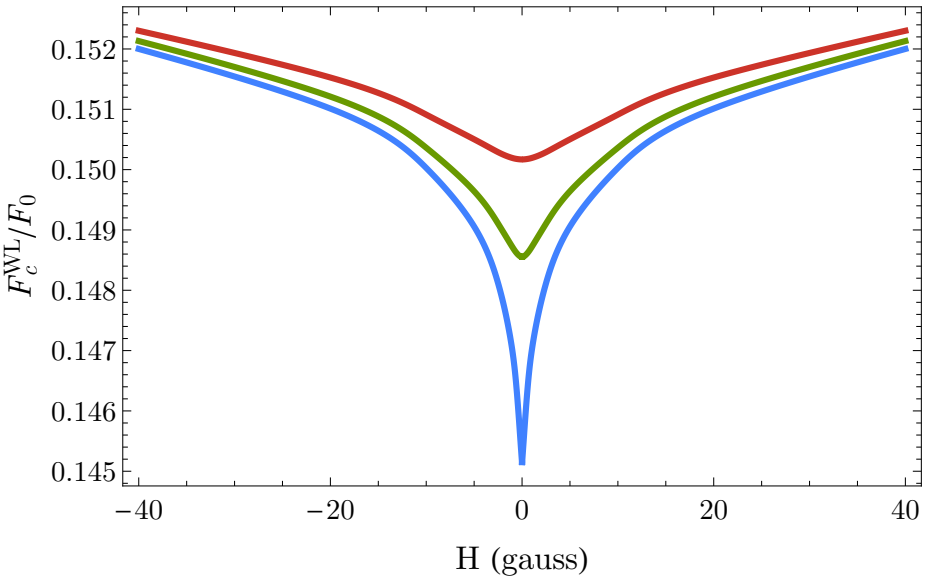

Figure 3.2: The dependence of the Casimir force on the applied magnetic field between two disordered plates (one 3D and one 2D) at a separation of $a = 250\,\text{nm}$. The 2D plate is described by the Drude model with the WL correction, Eq. (3.6). The Casimir force is normalized by the ideal conductor result $F_0 = -\hbar c\pi^2/240a^4$ and is plotted for three temperatures—3, 1, and 0.1 K, from top to bottom. At the lowest temperature considered, the WL correction gives a maximum of an 11% suppression of the force as compared to the simple Drude model. Note the similarity of this result and the dependence of the conductivity on magnetic field in Fig. 1.5.

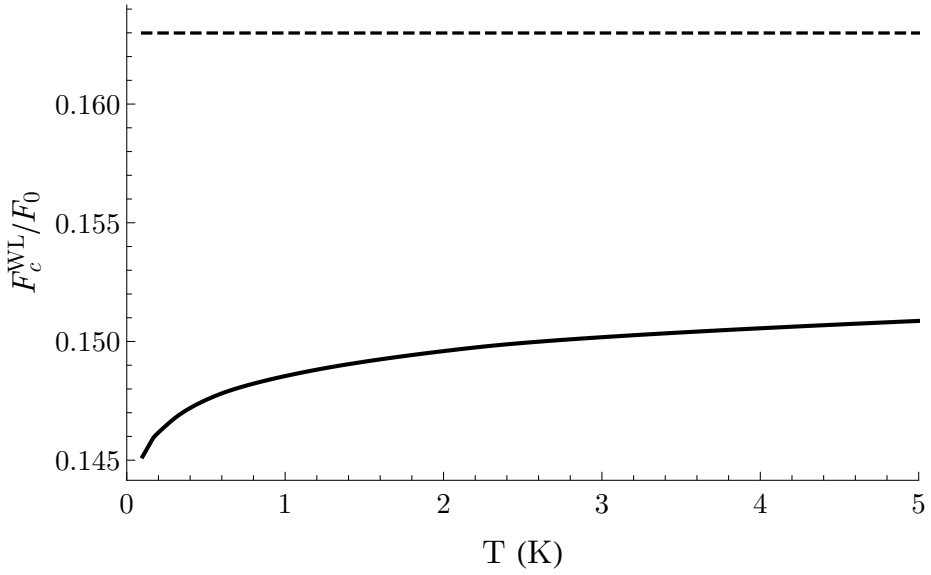

Figure 3.3: Dependence of the Casimir force on temperature between two disordered plates (one 3D and one 2D) at a separation of $a = 250\,\mathrm{nm}$. The force is normalized by the ideal conductor result F_0, and there is no applied magnetic field. The solid curve is obtained by including the WL correction in the 2D plate and the dashed curve is the result obtained if the effect of WL is ignored. Note the similarity of this result with the dependence of the conductivity on temperature in Fig. 1.5.

There are several ways to increase the size of the effect. The most straightforward way in principle to increase the size of the effect is to lower the temperature even further. We also find that the effect can be increased by decreasing the electron mean free path l. The simplest way to do this is to increase the impurity concentration, which can be seen by examining the dependence of Eq. (3.6) on the mean free path, given partially through the dephasing time in Eq. (3.7). When considering smaller values of l, however, we must assume that the impurity concentration is still below the limit of complete Anderson localization, or else the assumption of a diffusive model of conduction breaks down. On the other hand, when considering large values of l, which would make the effect smaller, one must be sure that the mean free path is much smaller than the sample dimension L or else the model of a disordered system breaks down. In real systems neither of these issues is likely to arise in practice.

A controlled smooth variation of temperature in Casimir effect experiments has proven challenging, especially at low temperatures where vibrational noise is difficult to remove due to the boiling of cryogenic liquids [107]. Instead, a test of the effects of WL in the Casimir effect could be more easily performed at fixed low temperature by varying magnetic field, looking for the effect shown in Fig. 3.2. Only weak magnetic fields would be necessary for such an experiment, as applying a magnetic field as weak as tens of gauss perpendicular to the plates should be enough to reduce the Casimir force by a significant percentage. An experimental test of these effects could be performed in the normal plate-sphere geometry with a very thin metallic film at a fixed separation, at a fixed low temperature, and with a varying weak magnetic field. While the exact numerical values the forces measured in this geometry are likely to differ from the results we find because of the simplifying assumptions we have made, the qualitative dependence on temperature and magnetic field are expected to remain.

3.3 Mesoscopic disorder fluctuations

When considering disordered systems one must determine when it is necessary to average over different realizations of the disorder potential. Different realizations of the disorder potential will give different Casimir energies, and spatial variations in the disorder potential will cause different parts of the plates to vary in how attractive they are—this is similar to the phenomenon of universal conductance fluctuations [108, 109] (UCFs)—leading to a self-averaging of the Casimir energy between two macroscopic plates. This argument would imply that, instead of carrying out the averaging procedure on the linear response Π, which gives the Lifshitz formula for the Casimir energy in terms of the Drude model response function, we should perform averaging over the entire Casimir energy. Indeed, it is well known that using the naive Drude model in the Lifshitz formula can not

be entirely correct, as it leads to a violation of the Nernst heat theorem [110, 111], with a nonzero entropy in the limit of zero temperature. In practice, however, it is not possible to calculate quantities using an exact disorder potential or to perform the averaging procedure over the entire Lifshitz formula, and it is unknown if the simplification of using the disorder-averaged linear response (i.e. the Drude model) in the Lifshitz formula is still a legitimate approximation.

Another way of phrasing this issue is that the approximation

$$\langle \mathcal{E}_c[\Pi] \rangle = \mathcal{E}_c[\langle \Pi \rangle] + \delta\mathcal{E}_c \approx \mathcal{E}_c[\langle \Pi \rangle] \tag{3.9}$$

leads to known issues, such as a violation of the Nernst theorem, but the full impact of neglecting the term $\delta\mathcal{E}$ is not well understood. In particular, it is unknown if this approximaion still gives a good approximation of the Casimir energy one would obtain if disorder were considered with a more rigorous treatment.

Here we calculate what effect fluctuations from an average disorder realization have on the Casimir energy at low temperature, where conductance fluctuations are strongest. We start from a microscopic version of the Lifshitz formula in position space,

$$\mathcal{E}_c\left[\Pi_1, \Pi_2\right] = k_B T \sum_{\omega_m}{}' \operatorname{Tr} \ln\left(1 - M\right), \tag{3.10}$$

where

$$M = \int dr_1 dr_2 dr_3 \hat{\tilde{\Pi}}_1(r, r_1) \hat{D}(r_1, r_2) \hat{\tilde{\Pi}}_2(r_2, r_3') \hat{D}(r_3, r').$$

Here, $\hat{D}$ is the photon propagator, which connects the screened response of one plate to the other, and $\hat{\tilde{\Pi}}_i$ is the random phase approximation (RPA) screened electromagnetic linear response functions for plate i, schematically given by $(\hat{\mathbf{1}} - \hat{\Pi}_i \hat{D}(0))^{-1} \hat{\Pi}_i$, where $\hat{\Pi}$ is the unscreened linear response function and $\hat{D}(0)$ is the photon propagator along the plate. From this point on we will assume plate 1 to have a particular disorder realization and that plate 2 is homogeneous and not disordered.

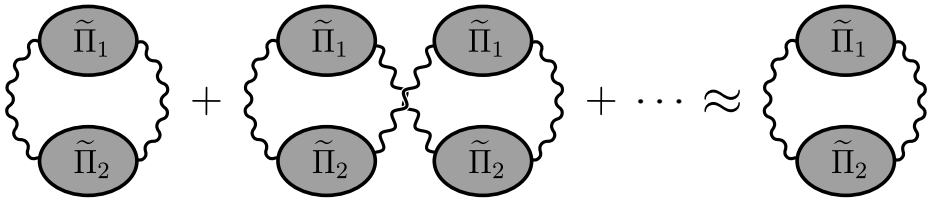

Figure 3.4: Diagrammatic representation of the lowest-order approximation to the Casimir energy given in Eq. (3.11). The gray ovals represent the RPA screened linear response functions and the wavy lines represent photon propagators.

We will further take both plates to be two dimensional. For two-dimensional plates, the linear response function and photon propagator are 2×2 matrices, with the components of Π being related to the optical conductivity of the plates. The trace Tr is a generalized trace over both this matrix structure and the position labels of the function M.

We are mainly interested in the case of isotropic metallic plates without a Hall effect. In this limit, both response functions are proportional to the identity matrix. The photon propagator is diagonal as well. The matrix trace in Eq. (3.10) becomes trivial, leaving a sum over photon polarizations. We make the further approximation that we can expand the logarithm in the expression for the Casimir energy in Eq. (3.1) and keep just the first term obtained from expanding the logarithm,

$$\mathcal{E}_c\left[\Pi_1, \Pi_2\right] \approx -k_B T {\sum_{\omega_m}}' \int \prod_{i=1}^{4} dr_i \sum_{X=\mathrm{TE,TM}} \tilde{\Pi}_1^X(r_4, r_1) D^X(r_1, r_2) \tilde{\Pi}_2^X(r_2, r_3) D^X(r_3, r_4), \tag{3.11}$$

where now we label the two photon polarizations with the superscript X. Diagrammatically, this approximation can be represented as in Fig. 3.4.

To find analytically tractable expressions, we must make one further simplifying approximation. We assume that the response function for plate 1 Π_1, which depends on an exact disorder realization, can be written as $\Pi_1 = \langle \Pi_1 \rangle + \delta\Pi_1$, i.e. the exact response function can be written as the disorder-averaged (Drude) response $\langle \Pi_1 \rangle$ plus a small term $\delta\Pi_1$ to account for the particular disorder realization[1]. With this

[1]Note that this $\delta\Pi_1$ is distinct from the function of similar name given in Eq. (1.10) and Eq. (1.11)

notation, we now expand the dressed response of plate 1, as given by the RPA, to first order in $\delta\Pi_1$ and write

$$\tilde{\Pi}_1 \approx \underbrace{\frac{\langle\Pi_1\rangle}{1-\langle\Pi_1\rangle D(0)}}_{=\tilde{\Pi}_1^D} + \left[\frac{1}{1-\langle\Pi_1\rangle D(0)} + \frac{\langle\Pi_1\rangle D(0)}{(1-\langle\Pi_1\rangle D(0))^2}\right]\delta\Pi_1$$
$$= \tilde{\Pi}_1^D + \underbrace{\frac{1}{1-\langle\Pi_1\rangle D(0)}\left[1+\tilde{\Pi}_1^D D(0)\right]}_{=\Gamma_1}\delta\Pi_1 . \quad (3.12)$$

This is the form of $\tilde{\Pi}_1$ that we use in Eq. (3.11).

We now look to the probability distribution for the Casimir energy due to fluctuations in the disorder realization in plate 1, now contained entirely within the function $\delta\Pi_1$. We can write the probability of seeing Casimir energy $\mathcal{E}$ to $\mathcal{E}+\delta\mathcal{E}$, divided by $\delta\mathcal{E}$, as

$$\mathcal{P}_{\mathcal{E}_c}[\mathcal{E}] = \langle\delta(\mathcal{E}_c - \mathcal{E})\rangle$$
$$= \int \mathcal{D}(\delta\Pi_1)\int\frac{dx}{2\pi}\,e^{ix(\mathcal{E}_c-\mathcal{E})}\exp\left[-\frac{1}{2}\int\prod_{i=1}^{4}dr_i\,\delta\Pi_1(r_1,r_2)K_1(r_1,\ldots,r_4)\delta\Pi_1(r_3,r_4)\right]. \quad (3.13)$$

This expression makes use of the disorder-averaged correlator of two response functions for the disordered plate, explicitly given as

$$K_1^{-1}(r_1,r_2,r_3,r_4) = \langle\delta\Pi_1(r_1,r_2)\delta\Pi_1(r_3,r_4)\rangle . \quad (3.14)$$

Figure 3.5 shows the corresponding diagrammatic representation.

The function K_1^{-1} is similar to the central object of interest considered in the context of UCFs [108, 109, 112], and it is calculated in the same manner. It is related to the size of the fluctuations of the conductivity, $\delta\sigma^2$ (or equivalently, in 2D,

which defines the WL correction to the correlation function obtained after disorder averaging.

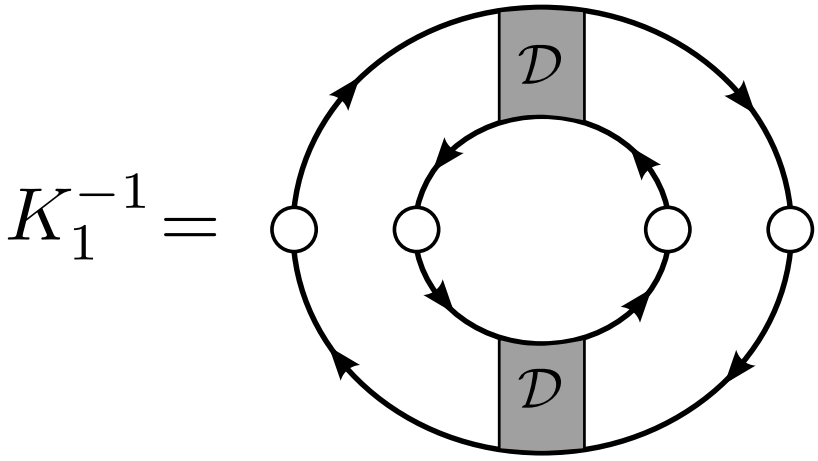

Figure 3.5: The primary diagram giving the correlation of disorder fluctuations, as defined in Eq. (3.14). The small circles are paramagnetic coupling of photons to electrons, and the shaded boxes represent diffusons. Diagrams containing more diffusons are found either not to contribute to the correlator or to have a contribution $O(1/\epsilon_F\tau)$ smaller.

the conductance) in a similar way to how the linear response function Π is related to the conductivity (see the expression following Eq. (1.9)). The only difference between the calculation of this function here and in the context of UCFs is that for UCFs one is primarily concerned with conduction of electrons through a system with attached leads, usually at zero temperature, while we consider a system with no leads at finite temperature. Given the similarities, most of the qualitative properties of conductance fluctuations also apply to our analysis of fluctuations in the Casimir energy, although the exact form of K_1^{-1} differs by small numerical factors.

With this insight, we can draw several conclusions about the nature of the distribution one obtains from Eq. (3.13). Most importantly, for weak disorder we can expect fluctuations of the Casimir energy around the average value to be small since conductance fluctuations are small in good metals [108, 109, 112]: $\delta\sigma^2/\sigma^2 \sim 1/(\epsilon_F\tau)^2$. Additionally, we should expect the size of the fluctuations to be reduced by a factor of 2 if a sufficiently large magnetic field is applied to the sample. This is because the diagram for K_1^{-1} given in Fig. 3.5 gives the same contribution at zero magnetic field if all diffusons are replaced with cooperons, but the cooperon

contribution is suppressed in magnetic fields in the same way as the WL correction to the conductivity.

In order to evaluate Eq. (3.13), we perform a saddle point approximation on the functional integral over the disorder fluctuation $\delta\Pi_1$. After a straightforward calculation we find

$$\mathcal{P}_{\mathcal{E}_c}[\mathcal{E}] \approx \frac{1}{\sqrt{2\pi W^2}} \exp\left[-\frac{(\mathcal{E}-\mathcal{E}_0^{\text{Drude}})^2}{2W^2}\right], \tag{3.15}$$

where $\mathcal{E}_0^{\text{Drude}}$ is the average Casimir energy and W is the width of the energy distribution. We find that the average energy is given by Eq. (3.11), but with the substitution $\tilde{\Pi}_1 \to \tilde{\Pi}_1^{\text{D}}$, i.e. replacing the exact unaveraged response function Π_1 with the disorder-averaged (Drude) response. Therefore, the average $\mathcal{E}_0^{\text{Drude}}$ is an approximation of the exact Drude result. Additionally, we find that the square of the width of the distribution can be written explicitly as

$$\begin{aligned} W^2 = (k_B T)^2 {\sum_{\{\omega_m,\omega_m'\}}}' \int \prod_{i=1}^{4} dr_i dr_i' \sum_{X,Y} D^X(r_1,r_2)\tilde{\Pi}_2^X(r_2,r_3)D^X(r_3,r_4) \\ \times D^Y(r_1',r_2')\tilde{\Pi}_2^Y(r_2',r_3')D^Y(r_3',r_4')\Gamma_1^X\Gamma_1^Y K_1^{-1}(r_1,r_4,r_1'r_4'), \end{aligned} \tag{3.16}$$

which can be represented diagrammatically as in Fig. 3.6. The multiple diagrams in this figure result from an expansion of the Γ_1 factors of Eq. (3.16),

$$\begin{aligned} \Gamma_1^X\Gamma_1^Y K_1^{-1} &= \frac{\left(1+\tilde{\Pi}_1^{\text{D}}D^X(0)\right)\left(1+\tilde{\Pi}_1^{\text{D}}D^Y(0)\right)K_1^{-1}}{\left(1-\langle\Pi_1\rangle D^X(0)\right)\left(1-\langle\Pi_1\rangle D^Y(0)\right)} \\ &\equiv \left(1+\tilde{\Pi}_1^{\text{D}}D^X(0)\right)\left(1+\tilde{\Pi}_1^{\text{D}}D^Y(0)\right)\tilde{K}_1^{-1}. \end{aligned} \tag{3.17}$$

We compute these expressions numerically in the same way that we calculate the Casimir force in Sec. 3.2. For both plates we use the Fermi energy and effective electron mass of gold, and we consider plate 1 to be disordered while plate 2 is a

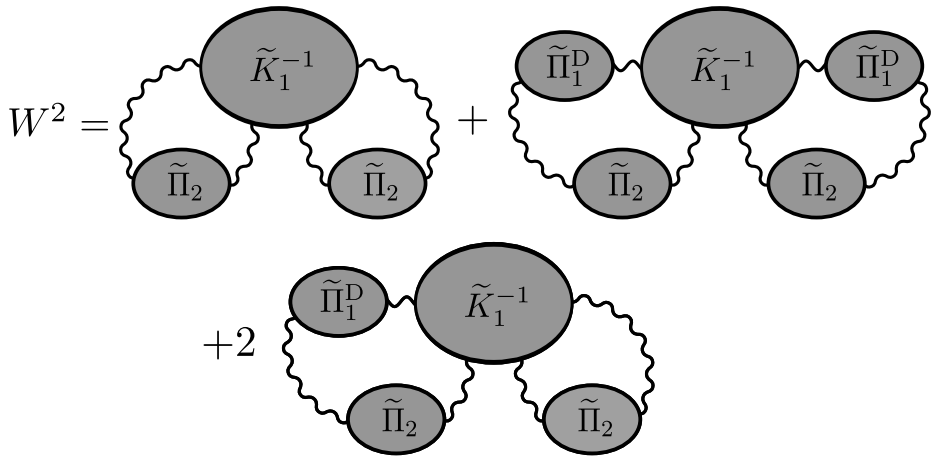

Figure 3.6: The diagrams giving the width of the distribution W in Eq. (3.16).

clean (plasma) plate, with $\Pi^{\mathrm{plasma}} = -ne^2/m$. We use the material parameters for gold in plate 2 so that in the limit of weak disorder we are left with identical plasma plates. We vary the parameter τ to determine the dependence of W and E_0, and fit the numerical results for their ratio to the expected functional dependence,

$$\frac{W}{\mathcal{E}_0^{\mathrm{Drude}}} \approx \frac{W}{\mathcal{E}_c^{\mathrm{plasma}}} + C_1 \frac{\hbar}{\epsilon_F \tau}, \tag{3.18}$$

with the fit shown in Fig. 3.7. In this expression $C_1 \approx 0.096$ is a distance-independent constant and $\mathcal{E}_0^{\mathrm{plasma}}$ is the Casimir energy between two clean plasma model plates calculated in the same approximation as $\mathcal{E}_0^{\mathrm{Drude}}$, using Eq. (3.11).

In the same way, we also find how $W/\mathcal{E}_0$ depends on the distance between the plates. It suffices to consider only the first term for this purpose, since the second term in Eq. (3.18) has no dependence on a. We find

$$\frac{W}{\mathcal{E}_c^{\mathrm{plasma}}} \approx C_2 \sqrt{\frac{\hbar c}{\epsilon_F a}}, \tag{3.19}$$

where $C_2 \approx 0.038$ is another constant independent of both τ and a.

The form of the disorder dependence in Eq. (3.18) is expected since a weakening of disorder, interpreted as an increase of the scattering time τ, will make a disordered

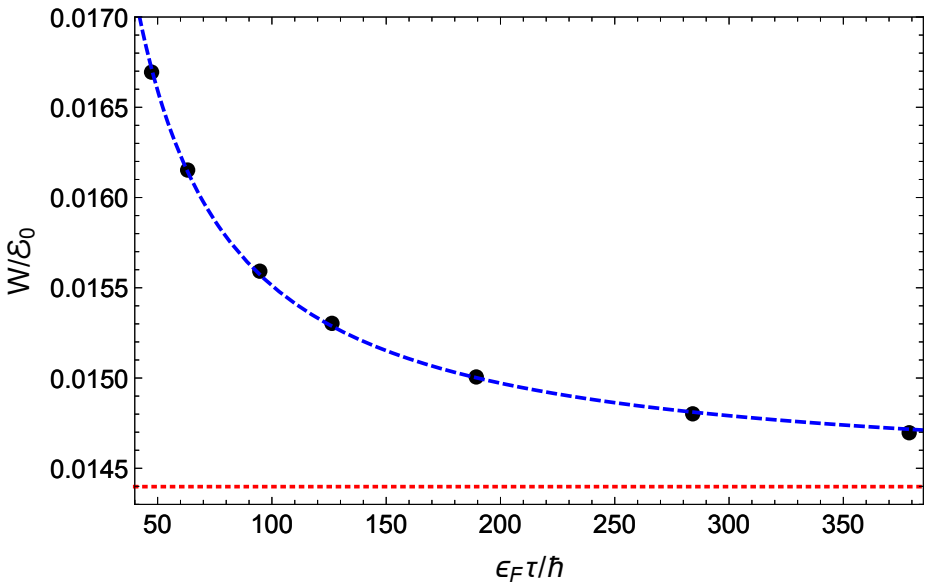

Figure 3.7: Fit of numerical data (black dots) for the quantity $W/\mathcal{E}_0^{\text{Drude}}$ to the expected functional dependence (dashed blue) given in Eq. (3.18). The dotted red line is the asymptotic value $W/\mathcal{E}_0^{\text{plasma}}$, which has no dependence on τ in the leading approximation.

plate more like a plasma plate. Therefore, a large scattering time should give a good approximation to the plasma result. Note, however, that the complete removal of disorder through the limit $\tau \to \infty$ has no physical meaning at this point in the calculation, since W has already necessarily been calculated in the presence of disorder. We can see from these two expressions that the distribution will be sharply peaked, in the sense that $W/\mathcal{E}_0^{\text{Drude}} \ll 1$, for plates that are not too close together and are in the disorder regime $1/\epsilon_F\tau \ll 1$, as we have considered thus far.

We can get a better understanding of how peaked the energy distribution is around its average value by comparing its width W to a smaller relevant energy scale $\mathcal{E}_0^{\text{Drude}} - \mathcal{E}_0^{\text{plasma}}$, by combining Eqs. (3.18) and (3.19). We obtain

$$\frac{W}{|\mathcal{E}_0^{\text{Drude}} - \mathcal{E}_0^{\text{plasma}}|} \approx C_2 \left(\sqrt{\frac{\hbar c}{\epsilon_F a}} + \frac{C_2}{C_1} \frac{c\tau}{a} \right) . \tag{3.20}$$

Note that the nature of the energy distribution Eq. (3.15) depends on the two

dimensionless quantities $\hbar c/(\epsilon_F a)$ and $c\tau/a$. The dependence on these parameters can be understood intuitively. The dependence on $\hbar c/(\epsilon_F a)$ can be understood as arising from the relevant photonic energy scale. The most important photons are those with wavelength equal to twice the distance between the plates, and when this distance is large, these long-wavelength photons are able to average over larger areas of the plates, reducing the effect of local fluctuations. The dependence on $c\tau/a$ is similarly straightforward. It is a comparison of two time scales: the impurity scattering time τ and the time for photons to traverse the distance between the plates, a/c. When the ratio is small, electrons will have many impurity scattering events before interacting with a photon, so effects due to impurities will be important.

There are several regimes we can now explore. Here, we will only consider plates of the same material, so the Fermi energy is a fixed parameter and we can vary only a and τ. First, if the plates are close together, meaning that $\hbar c/(\epsilon_F a)$ is large, then the distribution is wide regardless of the size of τ. Second, if τ is large compared to a/c, meaning that photons interact with any given electron many times between impurity scattering events, then the distribution is again quite wide, regardless of the size of $\hbar c/(\epsilon_F a)$. The only regime in which the distribution is sharply peaked is when both dimensionless parameters are small. This requires that the plates are much farther apart than both length scales $\hbar c/\epsilon_F$ and $c\tau$. In this limit each electron undergoes many impurity scattering events between photon interactions and the effect of disorder is more pronounced. Also in this limit, long wavelength photons are most important, which averages out the disorder fluctuations.

Ultimately, this means that for a given level of disorder, one can always find a large enough plate separation so that relatively small local fluctuations in the disorder potential of metallic plates do not greatly affect the Casimir energy, as shown in Fig. 3.8. The difficulty here is that for large values of the inelastic scattering time τ, the distance at which the distribution becomes very sharply peaked may

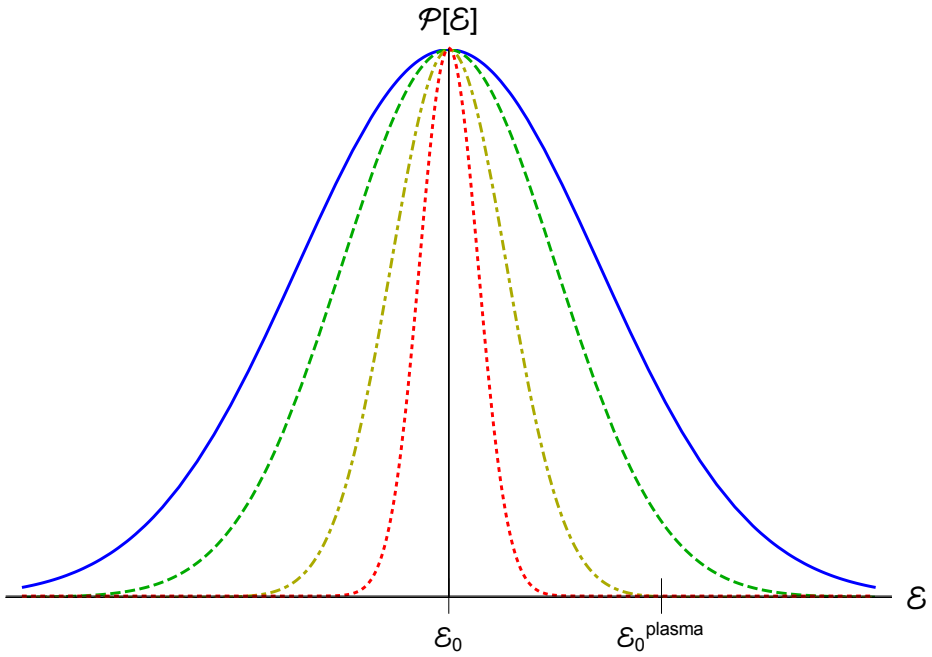

Figure 3.8: A plot of the distribution Eq. (3.15) for several values of a and a constant value $\tau = 4.5 \times 10^{-14}$ s, corresponding to $l = 60$ nm. The values of a are 250 (solid blue), 400 (dashed green), 800 (dash-dotted yellow), and 1600 nm (dotted red). The average $\mathcal{E}_0^{\text{Drude}}$ and width W are calculated numerically using Eqs. (3.11) and (3.16). The plots are scaled so that the distributions are all the same height, and so that $|\mathcal{E}_0^{\text{Drude}} - \mathcal{E}_0^{\text{plasma}}|$ is always the same width. Also indicated is the value of $\mathcal{E}_0^{\text{plasma}}$. One sees that as a is increased the distribution becomes sharply peaked compared to the small energy scale set by the difference from the plasma model.

be so large that the magnitude of the Casimir effect will become unmeasurably small. We note also that the values of the parameters τ and a used to obtain the results in the previous section give a distribution very sharply peaked around its average, so we are justified in our use of the Drude model despite concerns over the disorder-averaging procedure.

3.4 Conclusion

As we have shown, the weak localization correction to the Drude model at low temperatures may give the Casimir force a nontrivial dependence on both temperature and applied perpendicular magnetic field. Moreover, we find that, for low enough temperatures, WL effects perturb the Casimir force by an amount greater than the difference between the Drude and plasma model predictions. Since these effects are not applicable in a model of a 2D plate without disorder, i.e. the plasma model, a high-precision experimental test measuring this temperature or magnetic field dependence could give a definitive indication of whether a diffusive model truly describes the behavior of electrons in Casimir experiments.

Additionally, we explored the effect that fluctuations in the disorder potential can have on the Casimir energy and the validity of using the Drude model considering that the correct averaging procedure would give a result that differs from the Drude model by the inclusion of nonlocal disorder fluctuation contributions. We find that, for a given level of disorder, one can always ignore the effects of fluctuations if the plates are sufficiently far enough apart, which justifies the use of the Drude model.

Chapter 4: Fingerprints of Berry phases in the bulk exciton spectrum of a topological insulator

4.1 Overview

This chapter is taken with minor modification from the author's paper [113], published in Physical Review B, ©American Physical Society, 2018. One of the most widely studied phenomena associated with topological insulators (TIs) is the nature and behavior of the robust conducting Dirac states on their surfaces [85, 86]. From the particular perspective of exciton physics, there have been a number of works investigating the impact that excitons at the surface of TIs may have on the materials' optical properties [114, 115], as well as the possibility of exotic interaction effects such as chiral excitons [116] or as a platform for potential realizations of excitonic condensation [117, 118]. Other work has examined the impact of exciton condensation on the quantum spin Hall effect [119]. Something that has been largely overlooked in examinations of TIs, however, is how or whether topological properties can be manifest as bulk features.

In this chapter we consider the properties of excitons in the bulk of a 2D model of a TI. In particular, we examine a system that can be tuned between topologically trivial and nontrivial parameter regimes—the well-studied Bernevig-Hughes-Zhang (BHZ) model [87] introduced in Sec. 1.2.3, which accurately describes the band-inversion physics and topologically distinct phases observed in 2D Hg(Cd)Te quantum wells [88]. The model is given by the Hamiltonian

$$H_{\mathrm{BHZ}}(\mathbf{p}) = \begin{pmatrix} \hat{h}(\mathbf{p}) & 0 \\ 0 & \hat{h}(-\mathbf{p})^* \end{pmatrix}, \tag{4.1}$$

$$\hat{h}(\mathbf{p}) = \epsilon(p)\hat{\mathbf{1}} + \mathbf{d}(\mathbf{p}) \cdot \hat{\tau}, \quad \mathbf{d}(\mathbf{p}) = \left(Ap_x, -Ap_y, M(p)\right),$$

where $\epsilon(p) = C - Dp^2$ is the electron-hole asymmetry of the system, $M(p) = M - Bp^2$ is the momentum-dependent Dirac mass, $\hat{\tau}$ is the vector of Pauli matrices, $\hat{\mathbf{1}}$ is the unit matrix, and A, B, C, D, and M are material parameters. We will take $A > 0$ and $B < 0$ to match values obtained from experiments. We also note that $\epsilon(p)$ is irrelevant for the properties we will consider, and so we do not consider it from this point onward. Note that with fixed B the topological properties of the model are determined by the sign of M (see Sec. 1.2.3).

Far away from the surface, the band structure of a TI is qualitatively similar to that of a trivial insulator or a semiconductor with a large band gap. Consequently, optical and transport properties are naively expected to be similar as well, and indeed electrical conductivity through the bulk is exponentially small in the size of the gap for both trivial and topological insulators. Only a few studies have been done, however, exploring the effect of nontrivial topological character on other physical phenomena in the bulk. One such study [120] examined the polarization properties of a two-dimensional topological model, concluding that features of the optical conductivity of this model, including a plasmon resonance absent in graphene or usual two-dimensional electron gasses, provide a way to identify its topological character via bulk measurements. Other work has shown that the linewidths of bulk optical phonons contain information on band inversions in the electronic spectrum [121]. Here we add to this line of inquiry, investigating how the properties of excitons formed from the bulk bands of a topological insulator depend on the topological character.

Important quantities to consider in the context of TIs are the Berry connection, the Berry curvature, and the resulting Berry phase [89]. It has been well established that Berry physics can lead to a shift and splitting of otherwise degenerate exciton energy levels even in a system with trivial topological character [122, 123], i.e., without the usual hallmarks of topological phases such as protected edge states and

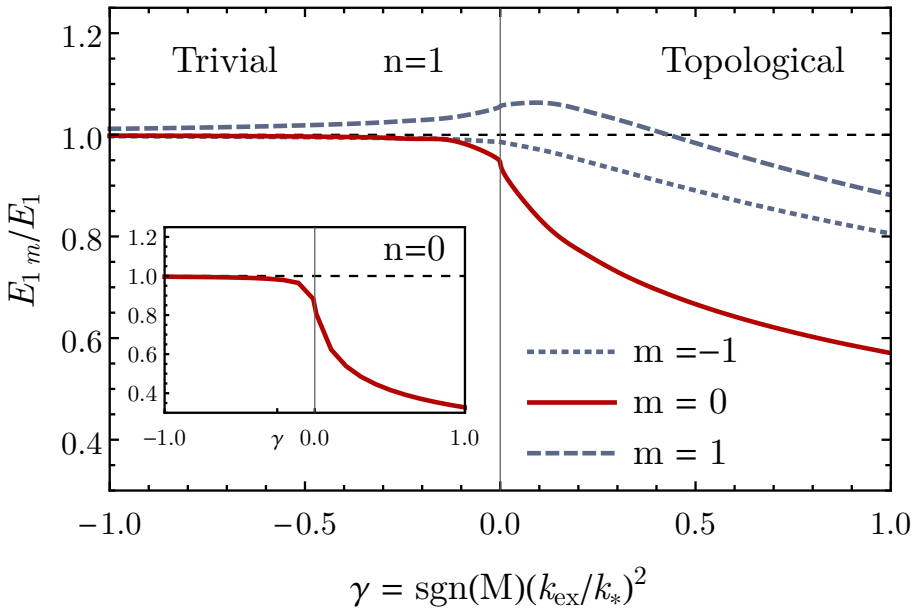

Figure 4.1: Calculated $n = 1$ energies for excitons formed from particles in the upper BHZ block as a function of a dimensionless parameter γ, which tunes the system between trivial ($\gamma < 0$) and topological ($\gamma > 0$) phases, scaled by the energy of 2D hydrogen with $n = 1$. The inset shows the energy of the $n = 0$ state for the same range of γ, scaled by the $n = 0$ hydrogen energy. There is a clear qualitiative difference in the behavior of the energy levels on different sides of the transition, with a crossover between them. In the topological phase there is a large splitting of states due to Berry physics that is absent in the trivial phase. Furthermore, the $m = 0$ states change energy quickly above the topological transition. Energies are obtained using an effective fine structure-constant $\alpha = 0.4$.

a nontrivial topological index such as the Chern number. It is therefore reasonable to expect that effects associated with Berry physics will be seen in the topological phase of the BHZ model.

We find that these expectations are indeed true, with key features of our main results given in Fig. 4.1. The hierarchy of exciton energy levels is drastically altered as one moves from the topologically trivial phase through the topological transition into the nontrivial phase. Within the topological phase, states with opposite orbital angular momentum are split from each other and the $m = 0$ angular momentum state is pushed to a smaller binding energy than the rest. In contrast, all these levels would be degenerate in the absence of Berry curvature. In the trivial phase, however,

all states are very nearly degenerate, with the splitting decreasing the further one tunes away from the topological transition. Although there is no sharp feature at the topological transition itself, as one might expect from a topological effect, this behavior nevertheless arises from effects intimately tied to topological character.

It is worth mentioning for completeness that other phenomena could potentially lead to splitting of exciton states [124], such as nonparabolicity in the spectrum [125, 126], screening of the Coulomb interaction in 2D systems [127, 128], or the exchange interaction between particles and holes [129]. None of these, however, are present in the model we use to generate these results. Moreover, the effect we find is distinct and distinguishable since none of these other effects are sensitive to changes in topology, and so would lead to splitting of states across the entire parameter range, not just on a single side of the topological transition.

In Sec. 4.2 we begin by presenting an intuitive understanding of the physics at play in this system, considering a semiclassical model as well as an effective Hamiltonian for Dirac-like systems. In Sec. 4.3 we formulate the quantum-mechanical description of excitons and discuss further how topological effects are manifest. In Sec. 4.4 we discuss the methods used to numerically calulate the exciton spectra in the regimes of interest and present our main numerical results.

4.2 Semiclassical approach

Before presenting the full quantum-mechanical analysis of the exciton problem, we discuss a semiclassical approach. This not only gives a clearer physical picture of the role of the Berry phase, but it also captures its effect on the electronic spectrum. The reason is that the semiclassical method applied to the usual 2D excitonic Coulomb problem reproduces the full spectrum exactly, and not just the structure of highly excited states. This remarkable result provides some assurance that the rest of the analysis will provide meaningful insights into the problem.

We start from the Lagrangian $L(\mathbf{r}_\mathrm{e}, \mathbf{r}_\mathrm{h}, \mathbf{p}_\mathrm{e}, \mathbf{p}_\mathrm{h})$ for the dynamics of interacting electron and hole wave-packets [130–132] given by

$$L = \sum_{\alpha=\mathrm{e,h}} \left(\dot{\mathbf{r}}_\alpha \cdot \mathbf{p}_\alpha + \dot{\mathbf{p}}_\alpha \cdot \mathbf{A}_{\alpha,\mathbf{p}_\alpha} - E^\alpha_{\mathbf{p}_\alpha} \right) - V(\mathbf{r}_\mathrm{e} - \mathbf{r}_\mathrm{h}). \tag{4.2}$$

Here $\mathbf{r}_{\mathrm{e(h)}}$ is the location of the electron (hole) wave-packet and $\mathbf{p}_{\mathrm{e(h)}}$ is its momentum. We approximate their dispersions as quadratic in the vicinity of band minima as $E^\alpha_\mathbf{p} = \alpha\, \epsilon_p + \mathbf{p}^2/2m$, where ϵ_p is the particle-hole asymmetry as defined after Eq. 1.13. Here $V(\mathbf{r}) = e^2/\epsilon r$ is the Coulomb interaction with dielectric constant ϵ. The function $\mathbf{A}_{\alpha,\mathbf{p}_\alpha} = i \langle \mathbf{p}, \alpha | \nabla_p | \mathbf{p}, \alpha \rangle$ is the Berry connection, calculated from the particle and hole states of the BHZ Hamiltonian 1.13. We consider only intrablock excitons (those formed from the particle and hole bands coming from a single 2×2 block of the BHZ Hamiltonian) with zero center of mass momentum $\mathbf{q}_\mathrm{CM} = 0$ since only they are optically active and are probed in experiments.

The Lagrangian for the relative motion of a single electron and hole reduces to

$$L = \dot{\mathbf{r}} \cdot \mathbf{p} + \dot{\mathbf{p}} \cdot \mathbf{A}_\mathbf{p} - \frac{\mathbf{p}^2}{2\mu} - V(\mathbf{r}), \tag{4.3}$$

where $\mu = m/2$ is the reduced electron-hole effective mass and the corresponding energy is independent of electron-hole asymmetry $\epsilon_\mathbf{p}$ of the BHZ model. The vector $\mathbf{A}_\mathbf{p} = \mathbf{A}_{\mathrm{e},\mathbf{p}} + \mathbf{A}_{\mathrm{h},-\mathbf{p}}$ is the Berry connection for the relative electron-hole motion, which for the BHZ model is (see Appendix B.2)

$$\mathbf{A}_\mathbf{p} = -\left(s + \frac{M_\mathbf{p}}{|\mathbf{d}_\mathbf{p}|} \right) \frac{\hat{\mathbf{z}} \times \mathbf{p}}{p^2}, \tag{4.4}$$

where $s \equiv \mathrm{sgn}(MB)$ and the corresponding Berry curvature is

$$\mathbf{\Omega}_\mathbf{p} = \nabla_p \times \mathbf{A}_\mathbf{p} = A^2 \frac{M + Bp^2}{|\mathbf{d}_\mathbf{p}|^3} \hat{\mathbf{z}}. \tag{4.5}$$

These two functions contain information about the topology of two particle states within the model. For example, the integral of the Berry curvature over all momentum space gives the Chern number, a topological invariant that distinguishes topological and trivial phases. Note that the Berry connection is not gauge invariant, changing by the divergence of a scalar function if the state vectors are transformed by multiplication with a momentum dependent phase, but the Berry curvature is invariant under such transformations.

The Euler-Lagrange equations obtained from Eq. (4.3) are given by

$$\dot{\mathbf{p}} = -\nabla_r V(\mathbf{r}) \tag{4.6}$$

$$\dot{\mathbf{r}} = \frac{\mathbf{p}}{\mu} + \nabla_r V(\mathbf{r}) \times \mathbf{\Omega}_{\mathbf{p}}. \tag{4.7}$$

The term containing the electron-hole Berry curvature $\mathbf{\Omega}_{\mathbf{p}}$ is called the anomalous velocity. Examining these equations in polar coordinates shows that the anomalous velocity contributes only to the angular motion of the exciton, with clockwise and counterclockwise spinning states affected in exactly opposite ways, breaking the symmetry between them that is present in the absence of the Berry curvature. In particular, the anomalous velocity changes the usual expression for angular momentum to

$$L_z = [\mathbf{r} \times \mathbf{p}]_z + \frac{\phi_{\mathbf{p}}}{2\pi}\hat{\mathbf{z}}. \tag{4.8}$$

Here $\phi_{\mathbf{p}}$ is the Berry phase acquired by traversing a circular trajectory with momentum $\mathbf{p}$. From this observation one can anticipate that states with opposite angular momenta will not have the same energy in this system, unlike the case for the 2D hydrogen atom.

We can provide some quantitative intuition for how topologically relevant physics comes into play by consideration of the function $\phi_{\mathbf{p}}$. To do so, we compare two momentum scales. The first is the topological scale $k_* = \sqrt{|M/B|}$. In the topological

regime M and B have the same sign. However, at $k = k_*$ the momentum-dependent Dirac mass $M_{\mathbf{k}} = M - Bk^2$ changes sign, making k_* an important momentum scale in the context of topological effects. We find that the Berry curvature reaches its maximum value near $k = k_*$ in the topological phase, and it is the point at which the function $\phi_{\mathbf{p}}$ suddenly increases and takes on a value that is almost the Chern number for larger momenta. In the trivial regime there are no features of note near $k = k_*$.

The second scale is the characteristic momentum for excitonic physics, related to the inverse Bohr radius of the exciton, $k_{\text{ex}} = 1/a_B = \mu e^2/\epsilon$. In the topological phase, if the excitonic momentum is small compared to k_*, then the Berry phase term is likewise small. This is always the case in the trivial phase since the Berry curvature is small for all reasonable momenta (see Appendix B.2). If the ratio $k_{\text{ex}}/*$ becomes even moderately sized in the topological phase, however, then the Berry phase will introduce a nontrivial perturbation to the angular momentum. Although it is not immediately apparent how this will affect the exciton spectrum, it is clear that a change will only occur in the topological phase when k_{ex}/k_* becomes sufficiently large.

Additional insight can be gained by rewriting the angular momentum as $L_z = (\mathbf{R} \times \mathbf{p})_z$. Here $\mathbf{R} = \mathbf{r} - \mathbf{A}_{\mathbf{p}}$ and $\mathbf{p}$ are the canonical coordinates of the problem, and the shift in the position coordinate is the momentum space equivalent of the Peierls substitution, which takes the Berry connection $\mathbf{A}_{\mathbf{p}}$ correctly into account. Using these coordinates, the equations of motion Eqs. (4.6) and (4.7) can be derived from the effective Hamiltonian $H_{\text{eff}}(\mathbf{R}, \mathbf{p})$ given by

$$H_{\text{eff}} = \frac{\mathbf{p}^2}{2\mu} + V(\mathbf{R} + \mathbf{A}_{\mathbf{p}}). \tag{4.9}$$

Expanding in the Berry connection $\mathbf{A}_{\mathbf{p}}$ and taking into account its solenoidal nature

in momentum space, we can write $H_{\text{eff}} = H_0 + \Delta H$, where H_0 is the usual Coulomb Hamiltonian,

$$H_0 = \frac{p_R^2}{2\mu} + \frac{L_z^2}{2\mu R^2} - \frac{e^2}{\epsilon R}, \tag{4.10}$$

with $p_R = \mathbf{p} \cdot \hat{\mathbf{R}}$, while ΔH is the correction due to the Berry curvature

$$\Delta H = \left(s + \frac{M_p}{|\mathbf{d}_p|} \right) \frac{e^2}{\epsilon R} \frac{L_z}{(Rp)^2}. \tag{4.11}$$

Examining this correction term, we see that it acts as a perturbation to the Hamiltonian of the 2D hydrogen atom. In general ΔH will split energy levels with differing angular momentum, which we anticipated to be the effect of the Berry phase based on our brief analysis of the equations of motion Eqs. (4.6) and (4.7) and the expression for angular momentum Eq. (4.8).

Equation (4.11) for ΔH is a generalization of a correction that was previously derived using the Foldy-Wouthuysen transformation for the case of a constant Berry curvature [123, 133]. The Foldy-Wouthuysen transformation produces a consistent quadratic approximation to a Hamiltonian with a linear dispersion at high energies. Because we approximated the dispersion as purely quadratic in our semiclassical analysis, we missed the Darwin term this transformation produces [123], which has the form $H_{\text{Darwin}} = \frac{1}{4}\Omega_z \nabla^2 V(R)$, where $\Omega_z = \Omega_z(\mathbf{p} = 0)$. This term gives an additional effective shift of the angular momentum index $L_z \to L_z + \frac{1}{2}$. This shift leads to an asymmetric splitting of states with opposite angular momentum as well as a shift for the $m = 0$ state, which, in this effective Hamiltonian picture, would otherwise remain unaffected by Berry physics.

4.3 Excitonic states

As discussed in Sec. 1.1.2, excitons are two-particle electron-hole bound states formed due to Coulomb interactions. Only excitons with zero total momentum

$\mathbf{q}_{\mathrm{CM}} = 0$ are optically active and will be considered here. Excitonic states can be written as

$$|\mathrm{X}_{i,j}\rangle = \sum_{\mathbf{k}} \Phi_{\mathbf{k}}^{(ij)} \; a_{\mathbf{k},+,i}^{\dagger} a_{\mathbf{k},-,j} \, |0\rangle \, . \tag{4.12}$$

Here $\Phi_{\mathbf{k}}^{(ij)}$ is the wave function of the exciton in momentum space, $|0\rangle$ is the state with filled valence bands and empty conduction bands, and $a_{\mathbf{k},\alpha,i}^{\dagger}$ ($a_{\mathbf{k},\alpha,i}$) creates (destroys) the single particle state $|\mathbf{k}, \alpha, i\rangle$, where $\alpha = \pm$ labels the band and $i = 1, 2$ labels the block of the BHZ Hamiltonian the state is taken from. When rotated to the band basis, each of the two 2×2 blocks of the BHZ Hamiltonian produces a single conduction and valence band, hosting the electrons and holes that are the building blocks of excitons. When $i = j$, the electron and hole come from the same block (intrablock excitons), while the case of $i \neq j$ corresponds to an interblock exciton. In general, intrablock excitons are optically active while interblock excitons require some degree of inversion symmetry breaking to be accessible via optical means. We do not consider such symmetry breaking in our model, but we calculate interblock exciton energies nonetheless as a point of comparison.

The exciton wave function satisfies a Schrodinger-like equation in momentum space given by

$$2\,|\mathbf{d}_{\mathbf{k}}|\,\Phi_{\mathbf{k}}^{(ij)} - \sum_{\mathbf{k}'} U_{\mathbf{k}-\mathbf{k}'} \mathcal{F}_{\mathbf{k},\mathbf{k}'}^{(ij)} \Phi_{\mathbf{k}'}^{(ij)} = (E_g + E_{\mathrm{X}}) \Phi_{\mathbf{k}}^{(ij)}, \tag{4.13}$$

which can be derived as in Appendix A. Here $E_g = 2\,|M|$ is the energy gap and $E_{\mathrm{X}} < 0$ is the exciton binding energy. The screened Coulomb interaction is given by $U_{\mathbf{q}} = 2\pi e^2/\epsilon q$, with ϵ being the effective dielectric constant of the surrounding medium, and $2\,|\mathbf{d}_{\mathbf{k}}| = E_{k,+,i} - E_{k,-,j}$ is the two-particle free dispersion, independent of the particle-hole asymmetry. Finally, $\mathcal{F}^{(ij)}$ is a function resulting from the rotation from the original basis of the Hamiltonian to the band basis, and its importance will be discussed at length.

To proceed, we now simplify the model by approximating the two-particle dispersion with a simple parabolic dispersion,

$$2\left|\mathbf{d}_{\mathbf{k}}\right| \to 2\left|M\right| + \frac{k^2}{2\mu}, \quad \text{with } \mu = \frac{|M|}{2A^2}. \tag{4.14}$$

This choice will change some features of the spectrum in the topological phase, which for the unmodified BHZ model develops a degenerate band minimum at a finite momentum for large enough $|M|$; in a more accurate approximation there is a value of M for which the effective mass near $k = 0$ changes sign within the topological phase. This alone can lead to large effects on excitonic properties but is actually unrelated to the topological transition. Since smooth deformations of the band structure leave topological properties unchanged, the above simplification is one way to remove this parametric dependence of the model on M while leaving topological properties intact. This allows us to more easily isolate the effect of topology alone.

Since this simplified model has rotational symmetry, we can perform a multipole decomposition of the exciton wave function and write

$$\Phi_{\mathbf{k}}^{(ij)} = \sum_m \Phi_m^{(ij)}(k) e^{im\varphi_{\mathrm{k}}}, \tag{4.15}$$

where $\varphi_{\mathbf{k}}$ is the angle of $\mathbf{k}$ from the k_x axis. The Schrodinger equation (4.13) then becomes

$$\frac{k^2}{2\mu}\Phi_m^{(ij)}(k) - \sum_{k'} U_m^{\mathrm{eff},ij}(k,k')\Phi_m^{(ij)}(k') = E_{\mathrm{X}}\Phi_m^{(ij)}(k), \tag{4.16}$$

where $U_m^{\mathrm{eff},(ij)}$ is the effective interaction in the m channel given by

$$U_m^{\mathrm{eff},(ij)}(k,k') = \sum_{m'} U_{m-m'}(k,k')F_{m'}^{(ij)}(k,k'), \tag{4.17}$$

and $F_m^{(ij)}(k,k')$ are the coefficients of the angular decomposition of $\mathcal{F}^{(ij)}$. Being the

index related to rotational invariance, m is a component of the angular momentum of the exciton, specifically the component related to the relative motion of its constituents (see Appendix B.1 for a discussion of the exciton angular momentum). It should be noted that the choice of the underlying spinor wave functions of electrons and holes is not unique (see Appendix B.2), and one can change them up to an arbitrary gauge transformation. Although gauge transformations leave all observables unchanged, they can uniformly shift the label m by any integer, making this label of excitonic states ambiguous and dependent on gauge choice. The gauge that we employ here is chosen to reduce to the normal labeling of states for the 2D hydrogen atom in the limit $MB \to -\infty$, i.e. infinitely far into the trivial regime.

The function

$$\mathcal{F}^{(ij)}_{\mathbf{k},\mathbf{k}'} = \langle \mathbf{k}, +, i | \mathbf{k}', +, i \rangle \langle \mathbf{k}', -, j | \mathbf{k}, -, j \rangle \tag{4.18}$$

results from the rotation from the original basis of the BHZ Hamiltonian to the band basis and is given by the overlaps of electron and hole spinor wave functions. We can explicitly write this function as

$$\begin{aligned} \mathcal{F}^{(11)}_{\mathbf{k},\mathbf{k}'} = e^{i(s-1)(\varphi_{\mathbf{k}}-\varphi_{\mathbf{k}'})} \cos^2\tfrac{\theta_{\mathbf{k}}}{2} \cos^2\tfrac{\theta_{\mathbf{k}'}}{2} + e^{i(s+1)(\varphi_{\mathbf{k}}-\varphi_{\mathbf{k}'})} \sin^2\tfrac{\theta_{\mathbf{k}}}{2} \sin^2\tfrac{\theta_{\mathbf{k}'}}{2} \\ + 2e^{is(\varphi_{\mathbf{k}}-\varphi_{\mathbf{k}'})} \cos\tfrac{\theta_{\mathbf{k}}}{2} \cos\tfrac{\theta_{\mathbf{k}'}}{2} \sin\tfrac{\theta_{\mathbf{k}}}{2} \sin\tfrac{\theta_{\mathbf{k}'}}{2}, \end{aligned} \tag{4.19}$$

$$\mathcal{F}^{(12)}_{\mathbf{k},\mathbf{k}'} = \cos^2\tfrac{\theta_{\mathbf{k}}}{2} \cos^2\tfrac{\theta_{\mathbf{k}'}}{2} + \sin^2\tfrac{\theta_{\mathbf{k}}}{2} \sin^2\tfrac{\theta_{\mathbf{k}'}}{2} + 2\cos\tfrac{\theta_{\mathbf{k}}}{2} \cos\tfrac{\theta_{\mathbf{k}'}}{2} \sin\tfrac{\theta_{\mathbf{k}}}{2} \sin\tfrac{\theta_{\mathbf{k}'}}{2} \cos(\varphi_{\mathbf{k}} - \varphi_{\mathbf{k}'}), \tag{4.20}$$

with $\mathcal{F}^{(11)} = \mathcal{F}^{(22)*}$, $\mathcal{F}^{(12)} = \mathcal{F}^{(21)}$, $\cos\theta_{\mathbf{k}} = M_{\mathbf{k}}/|\mathbf{d}_{\mathbf{k}}|$, and $s \equiv \mathrm{sgn}(MB)$. This is the only ingredient in the excitonic eigenvalue equation (4.13) that reflects the underlying topology, and it is qualitatively different in trivial and topological regimes.

The topological information carried in the functions $\mathcal{F}^{(ij)}$ can be seen explicitly

by considering their multipole expansions,

$$\mathcal{F}^{(11)}_{\mathbf{k},\mathbf{k}'} = \sum_{m=0}^{2} F_{s,m}(k,k')e^{ism(\varphi_{\mathbf{k}}-\varphi_{\mathbf{k}'})}, \tag{4.21}$$

$$\mathcal{F}_{\mathbf{k},\mathbf{k}'} = F_{s,0}(k,k') + F_{s,2}(k,k') + F_{s,1}(k,k')\cos(\varphi_{\mathbf{k}} - \varphi_{\mathbf{k}'}). \tag{4.22}$$

These three functions $F_{s,m}$, which are defined to be the coefficients of the multipole expansion of $\mathcal{F}^{(11)}$, are plotted in Figure 4.2 in the trivial and topological phases.

Far into the trivial parameter regime, one sees that $F_{-,0}$ is approximately equal to 1 for all values of k, k', while $F_{-,1}$ and $F_{-,2}$ are very small. Indeed in the limit $MB \to -\infty$, then $F_{-,0} \to 1$ and $F_{-,m\neq 0} \to 0$, so $\mathcal{F} \to 1$ and the Schrodinger equation approaches that of the 2D hydrogen atom.

In contrast, in the topological parameter regime, the behavior of $\mathcal{F}$ is nontrivial for all values of the tuning parameter. In this regime both $F_{+,0}$ and $F_{+,2}$ show nontrivial behavior as one or both of their arguments become large compared to the topological scale k_*. The remaining function, $F_{+,1}$ does not display such a drastic change on either side of the topological transition, though in the topological phase it always reaches the value 1/2 for $k = k' = k_*$. Note that these differences in the qualitative behavior of these functions are indeed tied directly to the topological character of the respective phases. There is a sudden transition between one behavior and the other as the tuning parameter passes through the topological transition, with the $(k, k') \to (\infty, \infty)$ limits of the functions $F_{+,0}$ and $F_{+,2}$ changing discontinuously at that point.

To gain further physical insight and to simplify eventual numerical calculations, we rewrite the eigenvalue problem in a dimensionless form by scaling all momenta by the characteristic exciton momentum, $k_{\text{ex}} = 1/a_B = \mu e^2/\epsilon$. Since the Bohr radius is the most natural length scale in the problem, its inverse gives a relevant momentum for excitonic physics. This rescaling naturally results in an equation

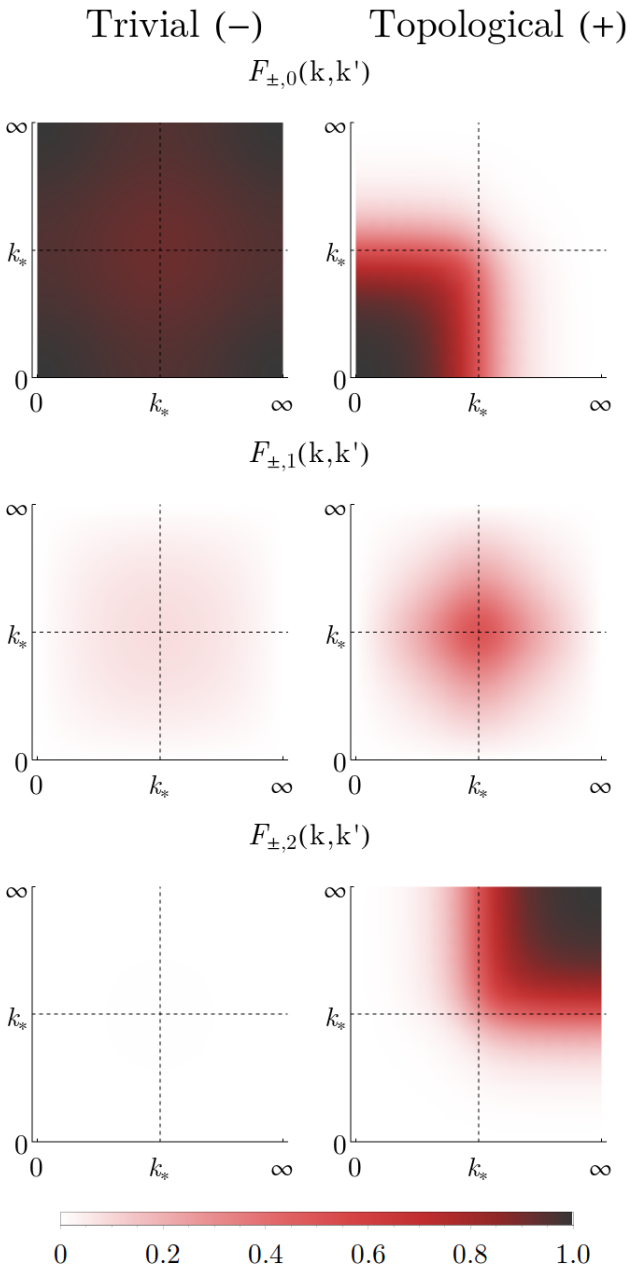

Figure 4.2: The multipole coefficients of the overlap function $\mathcal{F}^{(11)}$ plotted as functions of their two arguments k and k', with the infinite domains $k, k' \in [0, \infty)$ projected onto a finite interval. The plots on the left show the typical behavior of the F's in the trivial phase, and those on the right show them in the topologically nontrivial phase. $F_{\pm,0}$ and $F_{\pm,2}$ show distinct differences in their qualitative behavior on either side of the transition, with a discontinuous jump from one behavior to the other at the transition itself.

with only two dimensionless parameters: the relative fine-structure constant of the material $\alpha = e^2/\epsilon A$, and the quantity $\gamma = \mathrm{sgn}(M)(k_{\mathrm{ex}}/k_*)^2$, involving a ratio of the excitonic and topological momentum scales, which we use as our external tuning parameter.

As we discussed in Sec. 4.2, we can understand how the topological nature of the system manifests itself in excitonic properties by considering the relative size of these momentum scales, i.e., the size of γ. First note that the small momentum features of the functions $F_{s,m}$ shown in Fig. 4.2 are very much alike on either side of the transition. Close to the transition, where $|\gamma|$ is small and small momenta are most important, excitons in both sides of the topological transition should be qualitatively similar. Conversely, if $|\gamma|$ is not small, then the nontrivial features of the F functions near $k \sim k_*$ will be relevant in the topological phase, and excitons should behave quite differently depending on the sign of γ. From this we anticipate that a numerical analysis will not find a sharp feature in excitonic properties at the transition itself, but instead show a gradual crossover between two regimes.

Another way to see effects of topology is to compare the exciton problem to that of the two-dimensional hydrogen atom. Just as for the 2D hydrogen atom, the eigenstates of the excitons in this model are labeled by two indices, $n = 0, 1, 2, ...$ and $m = 0, \pm 1, ..., \pm n$, the principal and angular momentum quantum numbers[1]. For the 2D hydrogen atom a hidden SO(3) symmetry (distinct from, but containing SO(2) rotational symmetry) ensures a perfect degeneracy between the $2n+1$ angular momentum states for each n [134, 135], with energies given by

$$E_n = -\frac{\mu e^4}{2\epsilon^2} \frac{1}{\left(n + \frac{1}{2}\right)^2}. \tag{4.23}$$

In our system, although n and m are still good quantum numbers, the overlap

[1] Another common choice of quantum numbers for the 2D problem is $n_r = 0, 1, ...$ and $m = 0, \pm 1, \pm 2, ...$, related to our choice by $n = n_r + |m|$. For our purposes, n and m as defined in the text will prove more convenient.

function $\mathcal{F}$ breaks the SO(3) symmetry, mixing angular momentum channels and reorganizing the spectrum. The result is that different angular momentum states for each energy level n will have their energies split from each other, as anticipated in Sec. 4.2. Note that for interblock excitons, states with angular momentum differing by a sign must still be degenerate due to time-reversal symmetry, but those with different values of $|m|$ will generically be split.

In general, the breaking of this SO(3) symmetry is ensured by the existence of any nonzero Berry curvature ($\mathcal{F} \neq 1$), even in a phase with a trivial Chern number. However, far enough into the topologically trivial phase, one can consider this symmetry breaking as just a small perturbation to the 2D hydrogen atom Hamiltonian (i.e. $\mathcal{F} \approx 1 + \delta\mathcal{F}$ with $\delta\mathcal{F} \ll 1$), which only introduces a small splitting between the states. The same cannot be said of the topologically nontrivial phase, where the behavior of $\mathcal{F}$ is fundamentally nontrivial as well, as described above and in Fig. 4.2. In this case, the effect cannot be approximated as a small perturbation to the 2D hydrogen atom Hamiltonian, so we can expect that the splitting between states will not necessarily be vanishingly small.

4.4 Numerical Analysis

To solve Eq. (4.16) we discretize the momentum in the integral Schrödinger equation according to a modified Gaussian quadrature method (with $N = 192$ points) that is designed to handle the divergence in the Coulomb potential at $\mathbf{k} = \mathbf{k}'$ [136]. Choosing $\alpha = 0.4$ for the effective fine-structure constant, we can then invert the resulting matrix equation to find the excitonic spectrum as a function of the parameter γ. We scale all energies by the corresponding energies of the 2D hydrogen atom, i.e. with the same n, defining the effective mass μ in Eq. 4.23 the same way as in Eq. 4.14 so that the energy vanishes as $\gamma \to 0$.

Our main result was already presented in Fig. 4.1, showing the $n = 0$ state and

three $n = 1$ states for intrablock excitons[2]. In addition to these results, we also calculated the corresponding states for interblock excitons, finding similar effects. The qualitative behavior of the exciton energy levels in the topologically trivial and nontrivial regimes is immediately apparent, with the different angular momentum levels separating from each other quickly as a function of γ in the nontrivial regime, and converging to the 2D hydrogen energy moving deeper into the trivial regime, as expected based on the discussed properties of the function $\mathcal{F}$ and the semiclassical intuition developed in Sec. 4.2. Furthermore, we find that intrablock exciton levels with opposite angular momentum split from each other, while corresponding levels in interblock excitons remain degenerate as ensured by symmetry. We also note that while there is a crossover between two behavior regimes, there is no sharp feature at the topological transition itself, again as anticipated.

The most notable behavior, seen in all cases, is the strong dependence of the $m = 0$ state on γ, which has considerably lower energy in the topological regime compared to the trivial regime. Indeed, for interblock excitons this is the primary feature we find. Since this effect is found in all cases, it must be caused by a different mechanism than that causing the splitting of opposite angular momentum states in the intrablock case, i.e. it cannot be due to the Berry phase. In other words, it is an effect that is insensitive to time reversal and seems to be strongest for the cases of zero angular momentum. In particular, the Darwin term mentioned in Sec. 4.2 cannot be the only explanation since it is proportional to the Berry curvature and therefore cancels exactly in the interblock case. The underlying cause of this effect is not yet understood, but the onset of this energy shift at the transition indicates an origin related to topology. One possibility is that it is related to the quantum geometric tensor [137] or moments of the distribution of Berry curvature

[2]The exciton binding energy is identically zero at $\gamma = 0$ where the gap closes, and the finite values of the curves in the figure at this point are due to our choice of scaling; the 2D hydrogen atom energy levels also vanish at this point, but the limit of the ratio is finite.

in momentum space, e.g., the Berry curvature dipole [138].

4.5 Conclusions

By examining excitonic spectra in the bulk of a model system that has nontrivial topology we have demonstrated that topology can in principle have strong manifestations in bulk properties. In particular, we have shown that the degeneracy of 2D excitonic states in the BHZ model, which that would exist in a system without a Berry curvature, is broken due to the inclusion of such topological effects. In the trivial phase with Chern number 0 the splitting is small, with the Berry phase acting as a small perturbation to the 2D hydrogen atom problem. In the topological phase, however, the splitting is much greater since the effects of nontrivial topology can no longer be considered as a small perturbation. Though there is no sharp feature in the exciton spectrum precisely at the transition point, the difference in the behavior in the two phases can nevertheless be understood as a result of a change in the topological character. As the characteristic excitonic momentum scale k_{ex} becomes comparable to the scale associated with topological effects k_*, the large momentum differences between trivial and nontrivial phases becomes important to the physics of the system. The result is a dramatic reorganization of the excitonic spectrum, producing a hierarchy of states that is distinct for values of the tuning parameter well into each of the two phases.

Chapter 5: Cavity Bardasis-Schrieffer Polaritons

5.1 Overview

This chapter is largely taken from the author's paper [139], originally published in Physical Review B, ©American Physical Society, 2019. Strong light-matter interaction has been a field of continuing interest for many years [66], with exciton polaritons [53] in particular garnering much attention. Formed from strong coupling between microcavity photons and excitons within a semiconductor, exciton-polaritons and their condensation at high temperatures are a well-established experimental phenomenon [54, 57–59]. These systems have recently seen application in the quantum simulation of solid state physics [60–63], acoustic black hole physics [64], and topological properties of quasicrystal states [65].

Closely related cavity schemes have been proposed to enhance the strength of superconductivity through various different mechanisms [140–145]. Although there is a rough similarity between semiconducting and superconducting quasiparticle spectra, both featuring a gap, the BCS ground state is notably more complicated than that of a semiconductor, thus complicating the matter of superconductor-polariton formation.

In this chapter, we unite these two fields by examining an equivalent of exciton polaritons in a system composed of a cavity containing a superconducting layer instead of a semiconducting quantum well. In the superconductor, the role of excitons is replaced by Bardasis-Schrieffer (BS) modes, which are the closest analog of excitons in such a system, as described in Sec. 1.2.4. In our model the BS mode can be made to hybridize with photons in a resonant cavity to form polaritons, in close analogy with the theory of exciton polariton formation in semiconductors. Importantly we show how the BS mode's lack of linear coupling to light, which

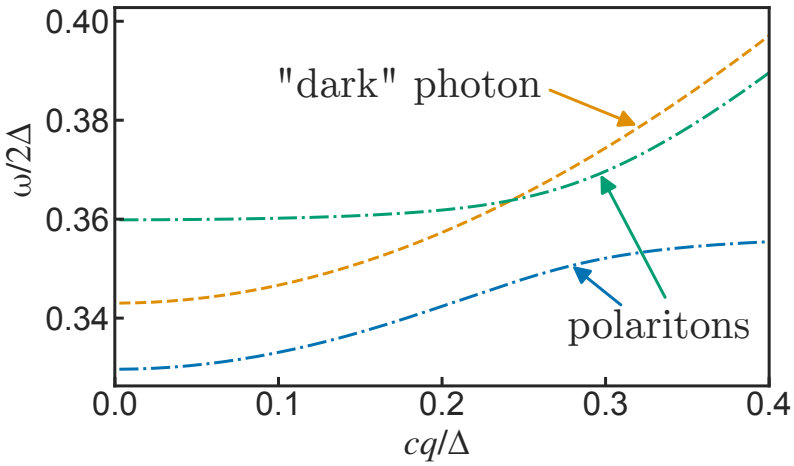

Figure 5.1: The dispersion of the Bardasis-Schrieffer-polariton modes (dot-dashed), calculated both numerically and with a simplified analytic method—the two methods give virtually identical results. An external supercurrent causes the BS mode and cavity photons to hybridize, and the polariton states have significant overlap with each. The "dark" photon mode (dashed) remains decoupled. The splitting of otherwise degenerate photon modes is a result of a supercurrent-induced self-energy contribution. Temperature and supercurrent angle are chosen to maximize hybridization (see Fig. 5.3).

would normally prohibit this hybridization, can be overcome by driving a supercurrent. This method has similarly been proposed for directly driving the Higgs mode of a superconductor with light [146] and has been recently implemented in experiment [147]. A secondary implication of our work is that the BS mode can also be observed optically with an experimental protocol similar to that of Nakamura *et al.* [147].

Our main results, presented in Fig. 5.1, demonstrate the hybrid Bardasis-Schrieffer polariton dispersions calculated from a microscopic model of coupled fermions and cavity photons. We further show that these polariton states can be described to an excellent degree of approximation by an intuitive effective Hamiltonian picture of the coupled modes, just as can be done for cavity exciton polaritons (see Sec. 1.1.3). Owing to the origin of the light-matter coupling, we examine how the extent of hybridization can be controlled in a straighforward manner.

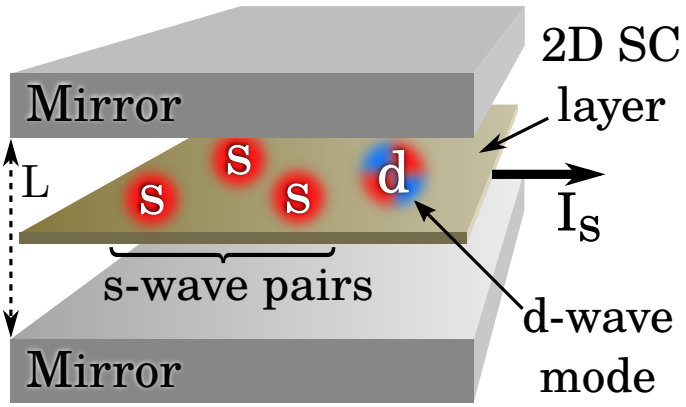

Figure 5.2: Illustration of a 2-dimensional superconductor with an applied supercurrent I_S at the center of a planar microcavity.

5.2 Superconductor BS modes coupled to photons

The setup we consider is illustrated in Fig. [**BSsystem**]. It consists of a two-dimensional electron system with a superconducting instability located at the center of a perfectly reflecting parallel mirror QED cavity. We focus on a two-dimensional electron system in particular because a thicker superconductor would have a larger effect on the cavity system. A thin-film superconductor can still be relatively transparent to photons as long as it is much thinner than the penetration depth. For a sufficiently thin film, we can consider the effect of the superconductor as a perturbation to the photon states of the empty cavity. Were the superconductor thick compared to its penetration depth, however, cavity would be split into two smaller decoupled cavities.

5.2.1 Superconducting model with BS modes

We assume the 2D electron system is described by a single-band fermion action with a BCS interaction decomposed in angular momentum channels. With $\hbar = 1$

the action can be written

$$S_\psi = \sum_{k,\sigma} \bar{\psi}_{k,\sigma} \left(-i\epsilon_n + \xi_k\right) \psi_{k,\sigma} - \frac{1}{\beta} \sum_q \sum_{\ell=s,d} g_\ell \bar{\varphi}_q^\ell \varphi_q^\ell, \tag{5.1}$$

where $\xi_k = k^2/2m^* - \mu$ is the energy measured from the Fermi surface, σ labels spin, the subscripts k and q of the fields each represent both momentum and Matsubara frequency, g_ℓ is the interaction strength in the ℓ-channel, and the interaction is written in terms of bilinears,

$$\varphi_q^\ell = \sum_k f_\ell(\phi_k) \psi_{-k+\frac{q}{2},\downarrow} \psi_{k+\frac{q}{2},\uparrow}. \tag{5.2}$$

Importantly, following Bardasis and Schrieffer [90] we assume the interaction is sizable in both s-wave and d-wave channels, but the s-wave component is stronger, $g_s > g_d$, which leads to a purely s-wave superconducting ground state. The form factors are taken to be $f_s(\phi_k) = 1$ and $f_d(\phi_k) = \sqrt{2}\cos(2\phi_k)$. This choice for f_d breaks the model's rotational symmetry by choosing an explicit k_x reference axis from which the momentum's angle ϕ_k is measured. Typically we expect this axis to be set by the underlying crystal structure of the system, which is not explicitly present in our continuum model.

The interaction can be decoupled in both angular momentum channels simultaneously with a Hubbard-Stratonovich transformation [103] and one finds

$$\begin{aligned} S = \sum_k \bar{\Psi}_k \left(-i\epsilon_n \hat{\tau}_0 + \xi_k \hat{\tau}_3\right) \Psi_k + \frac{1}{\beta} \sum_{q,\ell} \frac{1}{g_\ell} |\Delta_q^\ell|^2 \\ - \frac{1}{\beta} \sum_{k,q} \bar{\Psi}_{k+\frac{q}{2}} \sum_\ell f_\ell(\phi_k) \begin{pmatrix} 0 & \Delta_q^\ell \\ \bar{\Delta}_{-q}^\ell & 0 \end{pmatrix} \Psi_{k-\frac{q}{2}}, \end{aligned} \tag{5.3}$$

where $\Psi_k = (\psi_{k,\uparrow}, \bar{\psi}_{-k,\downarrow})$ are Nambu spinors, $\hat{\tau}_i$ are the Pauli matrices in Nambu space with $\hat{\tau}_0$ the identity, and Δ_q^ℓ are the complex Hubbard-Stratonovich decoupling

fields labeled by angular momentum.

5.2.2 Cavity model

The model of the photonic sector we use here is that of a parallel mirror cavity consisting of two perfectly conducting plates of infinite extent in the $x-y$ plane, separated by a distance L along the z axis (see Fig. 5.2). This gives perfectly reflecting boundary conditions at $z=0$ and $z=L$. The action for photons inside the empty cavity is (with $c=1$)

$$S_{\text{cav}} = -\frac{1}{2\beta}\sum_{q,n,\alpha} A_{\alpha,n,-q}\left[(i\Omega_m)^2 - \omega_{n,\mathbf{q}}^2\right] A_{\alpha,n,q}. \tag{5.4}$$

Here $\Omega_m = 2\pi m T$ is the Matsubara frequency with m an integer and T the system's temperature, α indexes the two cavity polarizations, n labels the quantized modes resulting from the confinement in z, $\omega_{n,\mathbf{q}}^2 = \omega_{n,0}^2 + q^2$, and $\omega_{n,0} = n\pi/L$.

We consider just the $n=1$ mode and drop the index from this point onward; all other modes are higher in energy and far from resonance with the BS mode. The vector potential can be written in terms of polarization vectors as $\mathbf{A}_q(z) = \sum_\alpha \boldsymbol{\epsilon}_{\alpha,\mathbf{q}}(z) A_{\alpha,q}$, which for the $n=1$ mode in the Coulomb gauge are given as

$$\begin{aligned}
\boldsymbol{\epsilon}_{1,\mathbf{q}}(z) &= i\sqrt{\frac{2}{L}}\sin\left(\frac{\pi z}{L}\right)\hat{\mathbf{z}}\times\hat{\mathbf{q}} \\
\boldsymbol{\epsilon}_{2,\mathbf{q}}(z) &= \sqrt{\frac{2}{L}}\frac{1}{\omega_q}\left(cq\cos\left(\frac{\pi z}{L}\right)\hat{\mathbf{z}} - i\omega_0\sin\left(\frac{\pi z}{L}\right)\hat{\mathbf{q}}\right),
\end{aligned} \tag{5.5}$$

where the momentum $\mathbf{q}$ is in the plane and $\hat{\mathbf{z}}$ and $\hat{\mathbf{q}}$ are the unit vectors along $\mathbf{z}$ and $\mathbf{q}$. We assume that the electron system is located in the middle of the cavity, so only $z = L/2$ must be considered. Consequently, the photon polarizations are orthogonal to each other and lie in the plane, with $\boldsymbol{\epsilon}_1$ along $\hat{\mathbf{z}}\times\hat{\mathbf{q}}$ and $\boldsymbol{\epsilon}_2$ along $\hat{\mathbf{q}}$. Minimal coupling between the cavity photon and the electron system generates

a paramagnetic coupling term proportional to $e\mathbf{v}_\mathbf{k} \cdot \mathbf{A}_q$, with the electron velocity operator $\mathbf{v}_\mathbf{k} = \mathbf{k}/m^*$, and a diamagnetic coupling term proportional to $e^2 A_q^2$. We drop the diamagnetic term since it is unimportant both in the weak-field regime [148] and for the cavity photon self-energy in the presence of disorder; although disorder is ubiquitous in 2D [103, 149] here we consider a clean system.

Note that this cavity geometry is chosen to simplify the calculation, but in real microwave cavities the transverse nature of the photon amplitude envelope is more complicated. The effect of this is to increase the strength of the paramagnetic coupling, which we include via a phenomenological enhancement factor in the light-matter coupling term [145, 148, 150].

5.2.3 Supercurrent-generated linear coupling

If one considers just the system as it has been introduced so far, the linear coupling between photons and the BS mode can be shown to be identically zero. This is understood by considering the symmetry of each state. The BS mode we consider here is a d-wave fluctuation, since the subdominant interaction is d-wave in nature, and a photon incident on the s-wave superconductor produces a state with p-wave symmetry, since it carries angular momentum ± 1. There is no overlap between these two states and so a photon cannot excite a BS mode. This particular obstruction to linear coupling can be overcome by breaking the pure s-wave symmetry of the superconducting state, and here we do so by considering an externally driven supercurrent.

A supercurrent can be understood as the superconducting condensate moving at constant uniform velocity with respect to the lab frame, with Bogoliubov quasiparticles being defined in the comoving frame, i.e. the supercurrent can be included via a simple Galilean transformation. Calling the condensate superfluid velocity $\mathbf{v}_S$, we have $\mathbf{v}_\mathbf{k} \to \mathbf{v}_\mathbf{k} + \mathbf{v}_S$. The angle of $\mathbf{v}_S$ with respect to the axis defined by $f_d(\phi_k)$,

as depicted in the inset in Fig. 5.3, is denoted θ_S. This modifies the quasiparticle dispersion in the lab frame,

$$\xi_k \to \xi_k + \mathbf{k}\cdot\mathbf{v}_S + \frac{1}{2}mv_S^2 \equiv \xi_k^S + \mathbf{k}\cdot\mathbf{v}_S. \tag{5.6}$$

The term linear in $\mathbf{k}$ is a Doppler shift in the quasiparticle energy which breaks its perfect s-wave symmetry. The v_S^2 term can be absorbed into a (negligible) redefinition of the chemical potential. The velocity shift also affects the paramagnetic coupling,

$$S_{\psi-A} \to \frac{X}{\beta}\sum_{k,q}\bar{\Psi}_{k+\frac{q}{2}}\underbrace{\left(-e\mathbf{v}_\mathbf{k}\hat{\tau}_0 - e\mathbf{v}_S\hat{\tau}_3\right)\cdot\mathbf{A}_q}_{\equiv\hat{\chi}_{k,q}[A]}\Psi_{k-\frac{q}{2}}. \tag{5.7}$$

Here X denotes the phenomenological coupling enhancement described above [145, 148, 150], which we absorb into a redefinition of the charge. Crucially the Nambu structure for the paramagnetic and supercurrent-induced terms are different ($\hat{\tau}_0$ vs $\hat{\tau}_3$), since particle and hole velocities are shifted oppositely, which, together with the spoiling of the quasiparticle s-wave symmetry, allows for the coupling of the BS mode to light. Note that the supercurrent can equivalently be included as a uniform phase winding of Δ^s which, upon appropriate gauge transformation, reproduces these results while maintaining gauge invariance throughout.

We now make the mean-field approximation to the s-wave gap function

$$S = S_{\Delta,s} + S_{\Delta,d} + S_{\text{cav}} - \sum_k \bar{\Psi}_k\hat{G}_k^{-1}\Psi_k + \frac{1}{\beta}\sum_{k,q}\bar{\Psi}_{k+\frac{q}{2}}\left(\hat{\chi}_{k,q}[A] - \hat{\Delta}_{k,q}^d\right)\Psi_{k-\frac{q}{2}}, \tag{5.8}$$

where $S_{\Delta,s} = \beta|\Delta|^2/g_s$ describes the static, homogeneous s-wave component Δ, $S_{\Delta,d} = \beta^{-1}\sum_q|\Delta_q^d|^2/g_d$ describes the d-wave fluctuations, $\hat{G}_k^{-1} = (i\epsilon_n - \mathbf{k}\cdot\mathbf{v}_S)\hat{\tau}_0 -$

$\xi_k^S \hat{\tau}_3 + \Delta \hat{\tau}_1$ is the inverse Nambu Green's function, and

$$\hat{\Delta}^d_{k,q} = f_d(\phi_k) \begin{pmatrix} 0 & \Delta^d_q \\ \bar{\Delta}^d_{-q} & 0 \end{pmatrix}. \tag{5.9}$$

The mean field value of Δ is obtained as the saddle point solution in the absence of $\mathbf{A}$ and Δ^d but in the presence of the supercurrent. This is consistent with the approximation that Δ is unaffected by d-wave fluctuations and photons.

5.3 Effective action

After integrating out the fermionic degrees of freedom and expanding to second order in $\hat{\Delta}^d$ and $\hat{\chi}$ we obtain the effective bosonic action

$$S_{\text{eff}} = S_d + S_A + S_{d-A}. \tag{5.10}$$

These three terms describe free d-wave fluctuations, cavity photons in the presence of the superconducting system, and the supercurrent-generated coupling between them, respectively.

Since d-wave fluctuations have much greater kinetic mass than photons, we approximate them with a flat dispersion and assume their energy can be found by taking the limit $\mathbf{q} \to 0$. Additionally, we drop all terms which vanish in the quasiclassical approximation. Writing Δ^d in terms of its real and imaginary components, S_d decouples into an action for each. The real mode is within the Bogoliubov quasiparticle continuum, and is therefore overdamped [90, 151]. It also remains decoupled from photons despite the supercurrent so we do not consider it further. The imaginary mode is the in-gap Bardasis-Schrieffer mode. Naming this mode d_q,

the BS mode action is found to be

$$S_d = \frac{1}{\beta}\sum_q d_{-q}\left[\frac{1}{g_d} + \sum_{\mathbf{k}} f_d(\phi_k)^2 \frac{2\lambda_k\left(n_F(E_{\mathbf{k}}^-) - n_F(E_{\mathbf{k}}^+)\right)}{(i\Omega_m)^2 - (2\lambda_k)^2}\right] d_q, \tag{5.11}$$

where $\bar{d}_q = d_{-q}$, $\lambda_k = \sqrt{\left(\xi_k^S\right)^2 + \Delta^2}$ is the quasiparticle energy in the comoving frame, n_F is the Fermi function, and $E_{\mathbf{k}}^{\pm} = \pm\lambda_k + \mathbf{k}\cdot\mathbf{v}_S$ is the Doppler-shifted energy.

The photon sector of the action consists of the empty cavity action S_{cav} plus a self-energy term due to the superconductor,

$$S_A = -\frac{1}{2\beta}\sum_{q,\alpha,\beta} A_{\alpha,-q}\left[\left((i\Omega_m)^2 - \omega_q^2\right)\delta_{\alpha\beta} - \Pi_{\alpha\beta,q}\right] A_{\beta,q}. \tag{5.12}$$

The matrix $\Pi_{\alpha\beta,q}$ is the electromagnetic linear response function of the superconducting system written in the cavity polarization basis.

Within the approximations discussed above the coupling between photons and the BS mode arises *entirely* through the supercurrent-induced term,

$$S_{d-A} = -\frac{ie\Delta}{\beta}\sum_{\mathbf{k},q,\alpha} f_d(\phi_k)\frac{i\Omega_m\,\delta n_{\mathbf{k}}}{(i\Omega_m)^2 - (2\lambda_k)^2}\frac{\mathbf{v}_S\cdot\boldsymbol{\epsilon}_{\alpha,q}}{\lambda_k}\left(A_{\alpha,q}\,d_{-q} - A_{\alpha,-q}\,d_q\right), \tag{5.13}$$

consistent with the previous argument that the d-wave BS mode should not normally couple linearly to light. We can see for Eq. (5.13) the BS mode only couples to the component of the vector potential parallel to the supercurrent.

The action for the coupled system is then written in terms of a hybrid inverse Green's function as

$$S_{\text{eff}} = \frac{1}{2\beta}\sum_q (d_{-q}, A_{\alpha,-q}) \begin{pmatrix} D_{\text{BS},q}^{-1} & g_{\beta,q} \\ g_{\alpha,q}^* & D_{\alpha\beta,q}^{-1} \end{pmatrix} \begin{pmatrix} d_q \\ A_{\beta,q} \end{pmatrix}, \tag{5.14}$$

with sums over repeated indices and with $D_{\text{BS},q}^{-1}$, $D_{\alpha\beta,q}^{-1}$, and $g_{\alpha,q}$ defined implicitly

through Eqs. (5.11)–(5.13).

5.4 Effective Hamiltonian

An intuitive understanding of the hybrid system can be obtained by deriving an effective Hamiltonian from this action picture. We can do this by first approximating the BS part of the action in a harmonic form, then rewriting both the d-wave fluctuation field d and the cavity photon field $\mathbf{A}$ in terms of mode creation and annihilation operators. Finally, making some simple approximations to the coupling term allows us to completely isolate the frequency dependence of the system, leaving us with a time-independent Hamiltonian.

5.4.1 Bardasis-Schrieffer sector

We begin by rewriting Eq. (5.11) for the action S_d describing the BS mode,

$$\begin{aligned}
S_d &= \frac{1}{\beta}\sum_q d_{-q}\left[\frac{1}{g_d} + \sum_{\mathbf{k}} f_d(\phi_k)^2\ \frac{2\lambda_k\,\delta n_{\mathbf{k}}}{(i\Omega_m)^2-(2\lambda_k)^2} - \frac{1}{g_s} + \sum_{\mathbf{k}}\frac{\delta n_{\mathbf{k}}}{2\lambda_k}\right] d_q \\
&= \frac{1}{\beta}\sum_q d_{-q}\left[\frac{1}{g_d} - \frac{1}{g_s} + \sum_{\mathbf{k}}\frac{\delta n_{\mathbf{k}}}{2\lambda_k}\left(\frac{(i\Omega_m)^2 + (2\lambda_k)^2(f_d(\phi_k)^2-1)}{(i\Omega_m)^2-(2\lambda_k)^2}\right)\right] d_q \\
&= \frac{1}{\beta}\sum_q d_{-q}\left[\frac{1}{g_d} - \frac{1}{g_s} + (i\Omega_m)^2\sum_{\mathbf{k}}\frac{1}{2\lambda_k}\frac{\delta n_{\mathbf{k}}}{(i\Omega_m)^2-(2\lambda_k)^2}\right. \\
&\qquad\qquad \left. + \sum_{\mathbf{k}} 2\lambda_k\cos(4\phi_k)\frac{\delta n_{\mathbf{k}}}{(i\Omega_m)^2-(2\lambda_k)^2}\right] d_q \\
&\equiv -\frac{1}{2\beta}\sum_q d_{-q} D^{-1}_{\mathrm{BS},q} d_q. \qquad (5.15)
\end{aligned}$$

In the first line we add terms that sum to zero using the gap equation for the s-wave order parameter, $\frac{1}{g_s} = \sum_{\mathbf{k}}\frac{\delta n_{\mathbf{k}}}{2\lambda_k}$. This regulates the integration and also allows us to parametrize the BS frequency in terms of the relative strength of the s-wave and d-wave interactions. In the last line we define the BS inverse Green's function D^{-1}_{BS}.

In order to change to the mode operator basis the inverse Green's function

D_{BS}^{-1} must be approximated with a harmonic form. We analytically continue the imaginary frequency to the complex plane, $i\Omega_m \to z \in \mathbb{C}$, then expand the inverse Green's function to second order in z around the saddle point solution we denote as Ω_{BS}, i.e. where the inverse Green's function vanishes, and finally restrict z back to the Matsubara frequency Ω_m. This is equivalent to finding the saddle point solution by the method of steepest descent. Note that because our model has no disorder, the BS mode frequency is real and so it does not decay. The result of this expansion is

$$S_d \approx -\frac{K}{2\beta}\sum_q d_{-q}\left((i\Omega_m)^2 - \Omega_{\mathrm{BS}}^2\right) d_q, \tag{5.16}$$

where the constant $K \equiv \partial^2 D_{\mathrm{BS}}^{-1}(z,\mathbf{q})/\partial z^2|_{z=\Omega_{\mathrm{BS}}}$ is a coefficient resulting from the Taylor expansion. In this form the BS mode field operators d_q can be written in terms of mode operators b_q, $\bar{b}_q$ as

$$d_q = \frac{b_q + \bar{b}_{-q}}{\sqrt{2K\Omega_{\mathrm{BS}}}} \tag{5.17}$$

and the action for the BS sector of the action in terms of these operators is then

$$S_d \to S_b = \frac{1}{\beta}\sum_q \bar{b}_q(-i\Omega_m + \Omega_{\mathrm{BS}})b_q. \tag{5.18}$$

5.4.2 Photon Sector

Because Eq. (5.12) for the action S_A of the empty cavity is already in harmonic form, defining photon mode operators can be done immediately,

$$A_{\alpha,q} = \frac{a_{\alpha,q} + \bar{a}_{\alpha,-q}}{\sqrt{2\omega_q}}. \tag{5.19}$$

However, the cavity is not completely empty, and so the photons also acquire a self-energy term from interaction with the superconductor, which we must carefully

treat when finding the Hamiltonian, as it may contain important momentum and frequency dependence.

The self-energy part of the photon action arises from

$$S_\Pi = \frac{1}{2}\,\mathrm{Tr}\left(\hat{G}\hat{\chi}\hat{G}\hat{\chi}\right) \equiv \frac{1}{2\beta}\sum_q \mathbf{A}_{-q}\hat{\Pi}_q\mathbf{A}_q = \frac{1}{2\beta}\sum_{q,\alpha,\beta} A_{\alpha,-q}\Pi_{\alpha\beta,q}A_{\beta,q}. \tag{5.20}$$

In the last equality, reproducing the term as written in Eq. (5.12), the response function Π has been rewritten in the basis of cavity polarizations from the original Cartesian basis of the vector potential,

$$\Pi_{\alpha\beta,q} = \sum_{i,j} \epsilon^i_{\alpha,-\mathbf{q}}\Pi^{ij}_q\epsilon^j_{\beta,\mathbf{q}}. \tag{5.21}$$

Though the polarization basis is useful for the change to mode operators, an appropriately chosen Cartesian basis is far more convenient for the evaluation of the $\hat{\Pi}$. We choose this basis to be defined as the directions parallel and perpendicular to the axis of the supercurrent because this is the basis most relevant for the hybridization problem, as seen in Eq. (5.13); only the component of $\mathbf{A}_q$ parallel to the supercurrent couples to the BS mode.

The function $\hat{\Pi}$ has the typical form of an electromagnetic linear response function in terms of fermionic Green's functions and current vertices resulting from paramagnetic coupling to light,

$$\Pi^{ij}_q = \frac{e^2}{\beta}\sum_k \mathrm{tr}\left[\hat{G}_{k+\frac{q}{2}}\left(v^i_{\mathbf{k}}\hat{\tau}_0 + v^i_S\hat{\tau}_3\right)\hat{G}_{k-\frac{q}{2}}\left(v^j_{\mathbf{k}}\hat{\tau}_0 + v^j_S\hat{\tau}_3\right)\right], \tag{5.22}$$

where $\hat{G}_k = \left[(i\epsilon_n - \mathbf{k}\cdot\mathbf{v}_S)\hat{\tau}_0 - \xi^S_k\hat{\tau}_3 + \Delta\hat{\tau}_1\right]^{-1}$ is the Nambu Green's function. Unlike for the Bardasis-Schrieffer mode, here we keep the q dependence of the Green's functions. Upon diagonalizing the Green's function with the appropriate Bogoluibov

transformation, $\widehat{U}_{\mathbf{k}} = \begin{pmatrix} u_{\mathbf{k}} & -v_{\mathbf{k}} \\ v_{\mathbf{k}} & u_{\mathbf{k}} \end{pmatrix}$ with $u_{\mathbf{k}}, v_{\mathbf{k}} = \sqrt{\frac{1}{2}\left(1 \pm \frac{\xi_k^S}{\lambda_k}\right)}$, and performing the Matsubara summation we have

$$\begin{aligned}\Pi_q^{ij} = e^2 \sum_{\mathbf{k}} \sum_{\alpha,\alpha'} & \frac{n_F\left(E^{\alpha'}_{\mathbf{k}-\mathbf{q}/2}\right) - n_F\left(E^{\alpha}_{\mathbf{k}+\mathbf{q}/2}\right)}{i\Omega_m - \left(E^{\alpha}_{\mathbf{k}+\mathbf{q}/2} - E^{\alpha'}_{\mathbf{k}-\mathbf{q}/2}\right)} \\ & \times \Big[v^i_{\mathbf{k}} v^j_{\mathbf{k}} \left(\ell^2_{\mathbf{k},\mathbf{q}} \delta_{\alpha,\alpha'} - p^2_{\mathbf{k},\mathbf{q}} \delta_{\alpha,-\alpha'}\right) + v^i_S v^j_S \left(n^2_{\mathbf{k},\mathbf{q}} \delta_{\alpha,\alpha'} + m^2_{\mathbf{k},\mathbf{q}}\ \delta_{\alpha,-\alpha'}\right) \\ & + \left(v^i_{\mathbf{k}} v^j_S + v^i_S v^j_{\mathbf{k}}\right) \ell_{\mathbf{k},\mathbf{q}} n_{\mathbf{k},\mathbf{q}}\ \alpha\, \delta_{\alpha,\alpha'} + \left(v^i_{\mathbf{k}} v^j_S - v^i_S v^j_{\mathbf{k}}\right) p_{\mathbf{k},\mathbf{q}} m_{\mathbf{k},\mathbf{q}}\ \alpha\, \delta_{\alpha,-\alpha'} \Big], \end{aligned} \tag{5.23}$$

where we have defined the superconductor coherence factors

$$\begin{aligned} \ell_{\mathbf{k},\mathbf{q}} &= u_+ u_- + v_+ v_- \qquad & p_{\mathbf{k},\mathbf{q}} &= u_+ v_- - v_+ u_- \\ n_{\mathbf{k},\mathbf{q}} &= u_+ u_- - v_+ v_- \qquad & m_{\mathbf{k},\mathbf{q}} &= u_+ v_- + v_+ u_-, \end{aligned} \tag{5.24}$$

using the shorthand notation for the Bogoliubov amplitudes $u_\pm = u_{\mathbf{k}\pm\mathbf{q}/\mathbf{2}}$ and $v_\pm = v_{\mathbf{k}\pm\mathbf{q}/\mathbf{2}}$.

Analytic evaluation of the function Π_q^{ij} with the full momentum and frequency dependence is cumbersome and unnecessary, so now, after analytic continuation to real frequency $i\Omega_m \to \omega + i0$, we expand to first order in the small deviation of the frequency from the cavity resonant frequency, $\delta\Omega = \omega - \omega_0 + i0$, which is the most that could be needed in the mode operator picture, and to second order in $q = |\mathbf{q}|$. Furthermore, we note that $v_{\mathbf{k}} \gg v_S$ and use this to make some further approximations, dropping terms with v_S when there is a corresponding term appearing with $v_{\mathbf{k}}$. We write the result of this expansion as

$$\begin{aligned}\Pi_q^{ij} \approx\ & x_P^{10,ij}(\phi_q)\, q + x_P^{11,ij}(\phi_q)\, q\delta\Omega + x_P^{20,ij}(\phi_q)\, q^2 \\ & + \left(x_S^{00} + x_S^{01}\, \delta\Omega + x_S^{10}(\phi_q)\, q + x_S^{11}(\phi_q)\, q\, \delta\Omega + x_S^{20}(\phi_q)\, q^2\right) \delta_{ij}\delta_{i,\parallel} \\ & + \left[\left(x_{SPs}^{10,i}(\phi_q) + x_{SPa}^{10,i}(\phi_q)\right)\ \delta_{j,\parallel} + \left(x_{SPs}^{10,j}(\phi_q) - x_{SPa}^{10,j}(\phi_q)\right) \delta_{i,\parallel}\right]\ q \end{aligned}$$

$$+\left[\left(x^{11,i}_{SPs}(\phi_q)+x^{11,i}_{SPa}(\phi_q)\right)\,\delta_{j,\parallel}+\left(x^{11,j}_{SPs}(\phi_q)-x^{11,j}_{SPa}(\phi_q)\right)\delta_{i,\parallel}\right]\,q\,\delta\Omega$$
$$+\left[\left(x^{20,i}_{SPs}(\phi_q)+x^{20,i}_{SPa}(\phi_q)\right)\,\delta_{j,\parallel}+\left(x^{20,j}_{SPs}(\phi_q)-x^{20,j}_{SPa}(\phi_q)\right)\delta_{i,\parallel}\right]\,q^2. \quad (5.25)$$

The fourteen coefficients x that appear in this expansion are given in Eq. (5.26) below. Many of them are functions of the angle ϕ_q between $\mathbf{q}$ and $\mathbf{v}_S$. The coefficients are labeled with a subscript showing the type of vertices they arise from, P for two paramagnetic vertices $\mathbf{v}_\mathbf{k}$, S for two supercurrent vertices $\mathbf{v}_S$, and SP for one of each. The secondary indices s and a on the SP coefficients label whether the term it appears in is symmetric or antisymmetric under exchange of the indices i and j. The superscript indices keep track of the powers of q (first index) and $\delta\Omega$ (second index) that the coefficient multiplies.

$$x^{10,ij}_P(\phi_q)=-e^2v_S\sum_\mathbf{k}\frac{N'_\mathbf{k}}{\omega_0}v^i_\mathbf{k}v^j_\mathbf{k}\cos\phi_q \quad (5.26a)$$

$$x^{11,ij}_P(\phi_q)=-\frac{x^{10,ij}_P(\phi_q)}{\omega_0} \quad (5.26b)$$

$$x^{20,ij}_P(\phi_q)=-\frac{e^2}{\omega_0^2}\sum_\mathbf{k}\left[\left(\frac{\xi^S_k}{\lambda_k}\right)^2N'_\mathbf{k}+\frac{\Delta^2}{\lambda_k^3}\frac{\omega_0^2\,\delta n_\mathbf{k}}{\omega_0^2-(2\lambda_k)^2}\right]v^i_\mathbf{k}v^j_\mathbf{k}\;v_k^2\,\cos^2(\phi_k-\phi_q) \quad (5.26c)$$

$$x^{00}_S=4e^2v_S^2\sum_\mathbf{k}\frac{\Delta^2}{\lambda_k^2}\frac{\lambda_k\,\delta n_\mathbf{k}}{\omega_0^2-(2\lambda_k)^2} \quad (5.26d)$$

$$x^{01}_S=-2e^2v_S^2\omega_0\sum_\mathbf{k}\frac{\Delta^2}{\lambda_k^2}\frac{\lambda_k\,\delta n_\mathbf{k}}{\left[\omega_0^2-(2\lambda_k)^2\right]^2} \quad (5.26e)$$

$$x^{10}_S(\phi_q)=e^2\omega_0v_S^3\sum_\mathbf{k}\frac{\Delta^2}{\lambda_k^2}\left[\frac{8\lambda_k\,\delta n_\mathbf{k}}{\left[\omega_0^2-(2\lambda_k)^2\right]^2}-\frac{N'_\mathbf{k}}{\omega_0^2-(2\lambda_k)^2}\right]\cos\phi_q \quad (5.26f)$$

$$x^{11}_S(\phi_q)=-e^2v_S^3\sum_\mathbf{k}\frac{\Delta^2}{\lambda_k^2}\left[8\lambda_k\frac{3\omega_0^2+(2\lambda_k)^2}{\left[\omega_0^2-(2\lambda_k)^2\right]^3}\,\delta n_\mathbf{k}-\frac{\omega_0^2+(2\lambda_k)^2}{\left[\omega_0^2-(2\lambda_k)^2\right]^2}N'_\mathbf{k}\right]\cos\phi_q \quad (5.26g)$$

$$x^{20}_S(\phi_q)=\frac{e^2v_S^2}{2}\sum_\mathbf{k}\frac{\Delta^2}{\lambda_k^2}\left[\frac{\Delta^2}{\lambda_k^3}\frac{\omega_0^2+(2\lambda_k)^2}{\left[\omega_0^2-(2\lambda_k)^2\right]^2}\delta n_\mathbf{k}-\left(\frac{\Delta}{\lambda_k}\right)^2\frac{N'_\mathbf{k}}{\omega_0^2-(2\lambda_k)^2}\right.$$

$$+\left(\frac{\xi_k^S}{\lambda_k}\right)^2 \frac{\lambda_k\,\delta n''_{\mathbf{k}}}{\omega_0^2-(2\lambda_k)^2}\Bigg]\, v_k^2\,\cos^2(\phi_k-\phi_q) \quad (5.26h)$$

$$x_{SPs}^{10,i}(\phi_q) = -\frac{e^2 v_S}{\omega_0}\sum_{\mathbf{k}}\left(\frac{\xi_k^S}{\lambda_k}\right)^2 N'_{\mathbf{k}} v^i_{\mathbf{k}}\; v_k\,\cos(\phi_k-\phi_q) \quad (5.26i)$$

$$x_{SPs}^{11,i}(\phi_q) = e^2 v_S\sum_{\mathbf{k}}\left(\frac{\xi_k^S}{\lambda_k}\right)^2 \frac{N'_{\mathbf{k}}}{\omega_0^2} v^i_{\mathbf{k}}\; v_k\,\cos(\phi_k-\phi_q) \quad (5.26j)$$

$$x_{SPs}^{20,i}(\phi_q) = -e^2 v_S\sum_{\mathbf{k}}\left(\frac{\xi_k^S}{\lambda_k}\right)^2 \frac{2\,N'_{\mathbf{k}}}{\omega_0^2} v^i_{\mathbf{k}}\; v_k\,\cos(\phi_k-\phi_q)\cos\phi_q \quad (5.26k)$$

$$x_{SPa}^{10,i}(\phi_q) = \frac{e^2 v_S}{\omega_0}\sum_{\mathbf{k}}\frac{\Delta^2}{\lambda_k^3}\frac{\omega_0^2\,\delta n_{\mathbf{k}}}{\omega_0^2-(2\lambda_k)^2} v^i_{\mathbf{k}}\; v_k\,\cos(\phi_k-\phi_q) \quad (5.26l)$$

$$x_{SPa}^{11,i}(\phi_q) = -e^2 v_S\sum_{\mathbf{k}}\frac{\Delta^2}{\lambda_k^3}\frac{\omega_0^2+(2\lambda_k)^2}{\left[\omega_0^2-(2\lambda_k)^2\right]^2}\delta n_{\mathbf{k}}\; v^i_{\mathbf{k}}\; v_k\,\cos(\phi_k-\phi_q) \quad (5.26m)$$

$$x_{SPa}^{20,i}(\phi_q) = e^2 v_S\sum_{\mathbf{k}}\frac{\Delta^2}{\lambda_k^3}\left[\frac{\omega_0^2+(2\lambda_k)^2}{\left[\omega_0^2-(2\lambda_k)^2\right]^2}\delta n_{\mathbf{k}} - \frac{\lambda_k\,N'_{\mathbf{k}}}{\omega_0^2-(2\lambda_k)^2}\right] \times v^i_{\mathbf{k}}\, v_k\,\cos(\phi_k-\phi_q)\cos\phi_q \quad (5.26n)$$

In these expressions we have used the shorthand notation $\delta n_{\mathbf{k}} = n_F(E^-_{\mathbf{k}}) - n_F(E^+_{\mathbf{k}})$, $\delta n''_{\mathbf{k}} = n''_F(E^-_{\mathbf{k}}) - n''_F(E^+_{\mathbf{k}})$, and $N'_{\mathbf{k}} = n'_F(E^+_{\mathbf{k}}) + n'_F(E^-_{\mathbf{k}})$, where $n'_F(E) = \partial n_F(\epsilon)/\partial\epsilon|_{\epsilon=E}$, etc. Because of the angular dependence inside the Fermi functions due to the Doppler shift in the quasiparticle energy $E^\pm_{\mathbf{k}}$, these coefficients cannot be evaluated analytically.

After numerical evaluation and comparing the size of the terms in the expression for Π_q^{ij}, we find that only the constant term with coefficient x_S^{00} given in Eq. (5.26d) is significant. This term affects just the component of $\mathbf{A}_q$ parallel to the supercurrent. Retaining only this term, self-energy contribution to the photon action is then

$$S_\Pi \approx \frac{1}{2\beta}\sum_q x_S^{00} A^\parallel_{-q} A^\parallel_q = \frac{1}{2\beta}\sum_{q,\alpha,\beta} x_S^{00}\epsilon^\parallel_{\alpha,-\mathbf{q}}\epsilon^\parallel_{\beta,\mathbf{q}} A_{\alpha,-q} A_{\beta,q}. \quad (5.27)$$

Using Eq. (5.19) for A_α, q in terms of mode operators and the approximation of discarding energy-nonconserving counterrotating terms ($\bar{a}\bar{a}$ and aa) we find that

the photon portion of the action reduces to

$$S_A \to S_a = \frac{1}{\beta}\sum_{q,\alpha,\beta} \bar{a}_{\alpha,q}\left[-i\Omega_m\delta_{\alpha\beta} + \omega_q\delta_{\alpha\beta} + x_S^{00}\frac{\epsilon^{\parallel}_{\alpha,-\mathbf{q}}\epsilon^{\parallel}_{\beta,\mathbf{q}}}{2\omega_q}\right] a_{\beta,q}. \tag{5.28}$$

The last two terms comprise the effective photonic Hamiltonian in the polarization basis. With our approximations the transformation between polarizations and Cartesian components induced by the polarization vectors is unitary up to an overall constant factor. Changing the mode operators from the polarization basis to the Cartesian supercurrent basis diagonalizes photon Green's function,

$$S_a = \frac{1}{\beta}\sum_q \left(\bar{a}^{\parallel}_q, \bar{a}^{\perp}_q\right)\left[-i\Omega_m\hat{\mathbb{1}} + \begin{pmatrix}\omega_q + \Pi^S_q & 0\\ 0 & \omega_q\end{pmatrix}\right]\begin{pmatrix}a^{\parallel}_q\\ a^{\perp}_q\end{pmatrix}, \tag{5.29}$$

where $\Pi^S_q = x_S^{00}/(L\,\omega_q)$ is the only remaining part of the photon self-energy and $a^i = \sum_\alpha \epsilon^i_\alpha a_\alpha$ are the mode operators in the supercurrent Cartesian basis.

5.4.3 Coupling Term

Finally we consider the coupling term S_{d-A} in the total action. We use Eqs. (5.17) and (5.19) to replace d_q and $A_{\alpha,q}$ with their definitions in terms of the mode operators b_q and $a_{\alpha,q}$, and then perform the same transformation on the photon mode operators as in Sec. 5.4.2, from the polarization basis to the Cartesian supercurrent basis. We then perform an analytic continuation $i\Omega_m \to \omega + i0$ and expand around the BS frequency to lowest order (i.e. we set $\omega = \Omega_{\rm BS}$), since that is the frequency at which the BS mode and photon bands would cross in the absence of coupling and therefore the frequency for which hybridization is most important. The imaginary part of the coupling term resulting from the infinitesimal shift off the real axis identically

vanishes. The result is

$$S_{d-A} \to S_{b-a} = \frac{ev_S\Delta}{\beta}\sum_{\mathbf{k},q}\sqrt{\frac{2\,\Omega_{\mathrm{BS}}}{L\,K\omega_q}}\frac{f_d(\phi_q)}{\lambda_k}\frac{\delta n_{\mathbf{k}}}{\Omega_{\mathrm{BS}}^2-(2\,\lambda_k)^2}\left(\bar{b}_q a_q^{\parallel}+\bar{a}_q^{\parallel}b_q\right), \tag{5.30}$$

from which we then extract the coupling matrix element

$$g_q = ev_S\Delta\sqrt{\frac{2\,\Omega_{\mathrm{BS}}}{L\,K\omega_q}}\sum_{\mathbf{k}}\frac{f_d(\phi_k)}{\lambda_k}\frac{\delta n_{\mathbf{k}}}{\Omega_{\mathrm{BS}}^2-(2\lambda_k)^2}. \tag{5.31}$$

With these rewritings of the fields in terms of mode operators along with all other approximations, all frequency dependence in the action becomes isolated into a linear term and the effective action Eq. (5.14) can be rewritten as

$$S_{\mathrm{eff}} \approx \frac{1}{\beta}\sum_q\left(\bar{b}_q,\bar{a}_q^{\parallel},\bar{a}_q^{\perp}\right)\left(-i\Omega_m\check{\mathbb{1}}+\check{H}_{\mathbf{q}}^{\mathrm{eff}}\right)\begin{pmatrix}b_q\\ a_q^{\parallel}\\ a_q^{\perp}\end{pmatrix}, \tag{5.32}$$

where we can now identify an effective single-particle Hamiltonian

$$\check{H}_q^{\mathrm{eff}} = \begin{pmatrix}\Omega_{\mathrm{BS}} & g_q & 0\\ g_q & \omega_q+\Pi_q^S & 0\\ 0 & 0 & \omega_q\end{pmatrix}, \tag{5.33}$$

where $q=|\mathbf{q}|$. As in the original effective action picture (see Eq. (5.14)), only one photon mode hybridizes with the BS mode in the Hamiltonian approximation, and so this 3×3 Hamiltonian has decoupled into a single uncoupled photon state and a 2×2 block reminiscent of the Hamiltonian used to describe cavity exciton polaritons, as in Eq. (1.7). The coupled photon and BS mode can be made resonant by tuning parameters of the system, most straightforwardly the cavity size L, allowing them to strongly hybridize.

Before discussing the calculation of the polariton energies it is worthwhile to examine the Hamiltonian coupling constant g_q. Because the strength of the hybridization is controlled exclusively by g, any of the parameters on which it depends, including the temperature T, the superfluid velocity v_S, and the supercurrent angle θ_S, can be used to control the strength of the effect. The dependence of the coupling on these parameters is shown in Fig. 5.3. The coupling vanishes for $T \to 0$ since it is mediated by thermally excited quasiparticles, for which the s-wave symmetry of the ground state has been broken by the addition of the supercurrent. When there is no populations of quasiparticles, there is nothing connecting the d-wave state with a BS mode and the p-wave state produced by absorbing a photon.

The coupling also vanishes for $T \to T_c$ because superconductivity vanishes, $\Delta \to 0$. The result is a unique maximum of $g(T)$ at an intermediate temperature, which we find to be $T_{\max} \approx 0.42T_c$. We use this temperature for all other computations. Similarly, g vanishes for small v_S—this can be verified by expansion of $\delta n_{\mathbf{k}}$—and also as v_S approaches a value corresponding to the critical current, where the superconducting state vanishes. We set $v_S = 0.9\Delta(v_S = 0)/k_F$ in our calculations, near the value giving the maximum coupling but not too near the critical value. The value $\Delta(v_S = 0)/k_F$ yields an approximate critical current consistent with values measured in iron-based systems, though in type II materials the current is limited by vortex pinning rather than condensate depletion [152, 153]. Dependence on the supercurrent angle θ_S comes through the d-wave form factor. The coupling is strongest when the supercurrent is along an antinode of the form factor – $\theta_S = m\pi/2$, $m \in \mathbb{Z}$ – and vanishes when the supercurrent is along a node – $\theta_S = (2m+1)\pi/4$. We use $\theta_S = 0$ for all other calculations.

The polariton energies given by the effective Hamiltonian can be written as

$$E_q^{(\pm)} = \frac{\Omega_{\mathrm{BS}} + \omega_q + \Pi_q^S}{2} \pm \sqrt{\left(\frac{\Omega_{\mathrm{BS}} - (\omega_q + \Pi_q^S)}{2}\right)^2 + g_q^2}. \tag{5.34}$$

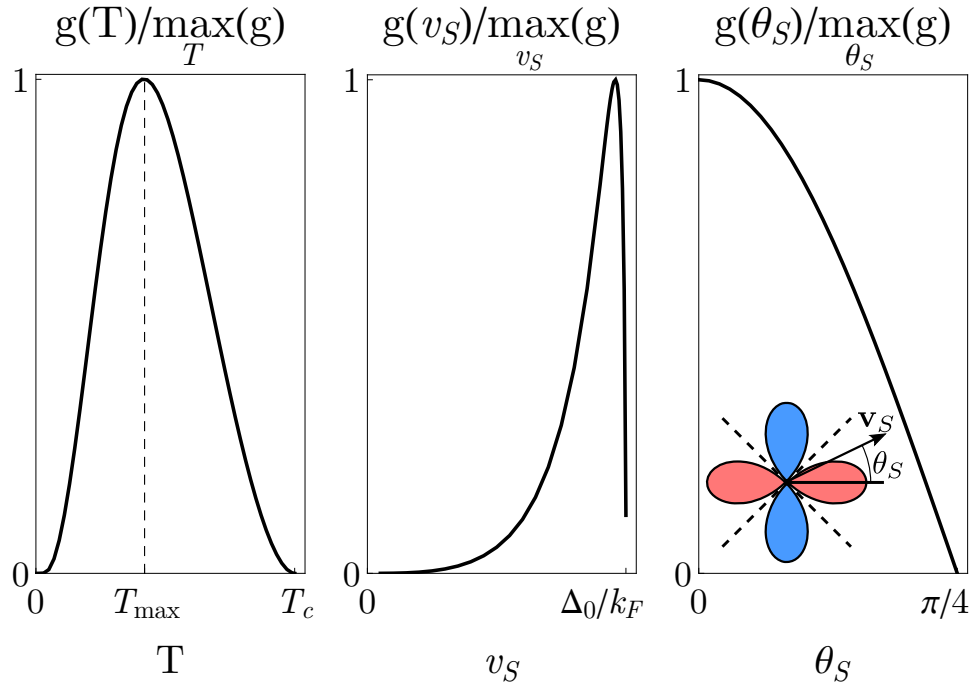

Figure 5.3: The hybridization matrix element g in the effective Hamiltonian as a function of temperature, superfluid velocity, and θ_S, the angle between the direction of the supercurrent and the axis defined implicitly by the d-wave form factor $f_d(\phi_k)$, all scaled by their respective maxima. (Left) $g(T)$ is maximized for a temperature $T_{\max} \approx 0.42T_c$. (Center) $g(v_S)$ is sharply peaked for large superfluid velocity around $v_S \approx 0.96\Delta(v_S = 0)/k_F$. (Note, $\Delta_0 \equiv \Delta(v_S = 0)$.) (Right) $g(\theta_S)$ is maximal for $\theta_S = m\pi/2$, $m \in \mathbb{Z}$, and vanishes when the supercurrent runs along a node of f_d, $\theta_S = (2m + 1)\pi/4$. *Inset* — the orientation of the supercurrent with respect to the d-wave form factor. The color of the lobes gives the relative sign of f_d for different angles, and the dashed lines are the nodes where $f_d = 0$. The plots use $T = T_{\max}$, $v_S = 0.9\Delta(v_S = 0)/k_F$, and $\theta_S = 0$ where applicable, and fixed detuning $\omega_0 = 0.96\Omega_{\mathrm{BS}}$.

5.5 BS polariton numerics and results

We now verify the results of this analytic model by numerically solving for the polariton dispersions as poles of the bosonic Green's function, Eq. (5.14). For our calculations we use material parameters motivated by iron-based superconductors [154–157], where BS modes have been experimentally reported. We set the Fermi energy $\epsilon_F = 100$ meV, the effective mass $m^* = 4m_e$ [1], where m_e is the electron mass, and critical temperature $T_c = 35$ K. We set $1/g_d - 1/g_s = 0.1\nu$, where $\nu = m^*/2\pi$ is the 2D density of states, and tune the size of the cavity L so that $\omega_0 = \pi/L = 0.96\,\Omega_{\mathrm{BS}}(\theta_S = 0)$, putting photons and the BS mode very near perfect resonance. Finally, we set the phenomenological coupling enhancement factor to $X = 10$, although enhancements of $X = 10^2$ or greater have been predicted in similar cavity systems [145, 148, 150].

5.5.1 Numerical method

The numerical method of obtaining the polariton energies begins with Eq. (5.14), the effective Gaussian Matsubara action describing the coupled Bardasis-Schrieffer cavity-photon system. At this stage the polariton modes can be found by solving for the frequency $z = i\Omega_m$ at which the inverse of the Green's function matrix for the coupled system $\hat{D}^{-1}$ vanishes. To do so, we numerically solve for the roots of the determinant of the inverse Green's function $\det \hat{D}^{-1}(\Omega_{\mathbf{q}i}, \mathbf{q}) = 0$. In particular the following algorithm was employed at each $\mathbf{q}$: noting that there are three roots that we are searching for

1. An interval $[\omega_l, \omega_u]$ is chosen within which to search for solutions.

2. An extremum f of $\det \hat{D}^{-1}(\Omega, \mathbf{q})$ with respect to Ω is located by finding the

[1] In the quasiclassical approximation the value of the effective mass cancels everywhere, since only $v_S \propto 1/k_F \propto 1/\sqrt{m^*}$, $K \propto \nu = m^*/2\pi$, and $\sum_{\mathbf{k}} \sim \nu \int d\xi$ depend on it. Therefore, the choice of effective mass is mostly unimportant.

roots of the first derivative with respect to Ω using the Newton-Raphson method in the vicinity of the Bardasis-Schrieffer frequency Ω_{BS}.

3. The other extremum is found by searching for the root of the first derivative in the interval (ω_l, f) or (f, ω_u) as determined by the sign of the function at the endpoints. This gives us two extrema $\{f_0, f_1\}$.

4. Roots of $\det \hat{D}^{-1}(\Omega, \mathbf{q})$ are searched for using the Brent-Dekker method in the intervals (ω_l, f_0), (f_0, f_1), and (f_1, ω_u).

Numerical integration and root-finding were performed using the GSL Scientific Library [158].

5.5.2 Bardasis-Schrieffer polariton results

Comparing the results of this numerical procedure with the approximate energies given in Eq. (5.34), we find that the two methods are in excellent agreement. The dispersions are plotted for both methods in Fig. 5.1—the results from the two methods are visually indistinguishable, differing by, at most, one part in 10^4 for our choice of parameters. This verifies that the approximations made in deriving the effective Hamiltonian Eq. (5.33) are indeed valid.

One can clearly see that only one photon mode strongly hybridizes with the BS mode, while the other "dark" photon remains distinct. This is made especially clear by examining the overlap of the BS mode with the polariton eigenstates obtained from the effective Hamiltonian formulation, shown in Fig. 5.4. Because we have chosen the BS mode and photon dispersions to be detuned in our calculations, i.e. to cross at finite momentum instead of $q = 0$, it is at that non-zero value that the two polariton modes have the same overlap with the BS mode. The lower polariton mode becomes more photon-like for smaller momenta, but even for $q = 0$ it still has significant overlap with the BS mode.

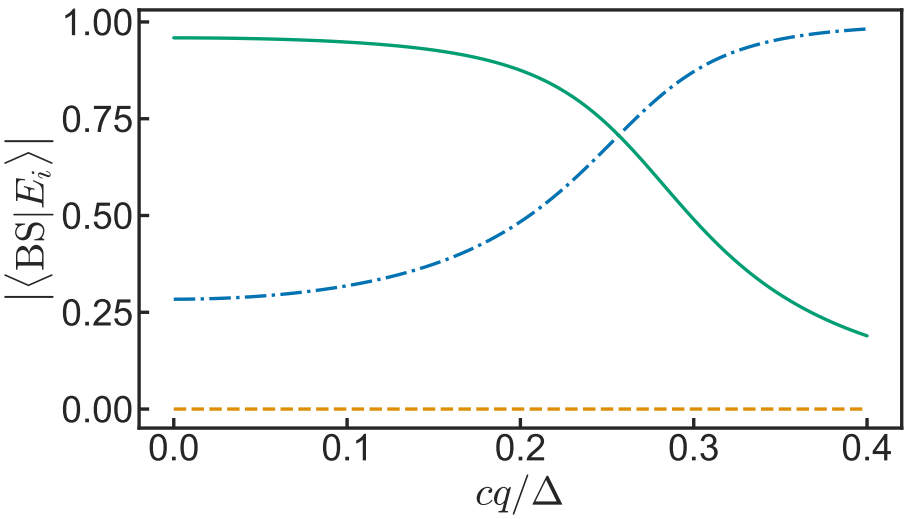

Figure 5.4: The Bardasis-Schrieffer component of the eigenvectors of the effective Hamiltonian, from Eq. (5.33). The upper (solid) and lower (dot-dashed) polaritons have significant photon and Bardasis-Schrieffer character, indicating strong hybridization between the systems. The "dark" photon mode (dashed) which does not hybridize with the superconductor's collective mode.

5.6 Conclusion

In this chapter we have shown that driving a supercurrent through a superconductor in a planar microcavity leads to hybridization of cavity photons with a collective mode of the superconductor. In particular two polariton bands form which have significantly mixed character. This provides a means for observation and control of the Bardasis-Schrieffer mode, and, as for exciton-polaritons, these dispersions could in principle be measured with k-space imaging of the photonic component of the polariton states [55]. The nature of the construction allows for tuning of the hybridization strength, and therefore gives a means to control properties of the polariton states *in situ* through manipulation of the externally applied supercurrent.

We speculate that the condensation observed in exciton-polariton systems [57–59] suggests that properly driving these superconductor-polariton modes could lead to their condensation and the formation of a non-equilibrium $s \pm id$ superconducting state—recall that the mode hybridizing with cavity photons is $\pi/2$ out of phase with

the s-wave condensate. There is reason to suspect that condensation is a reasonable prospect; thermalizing interactions arise at quartic order in the perturbation theory we used in deriving the results we present here, and the polariton lifetime is set by the cavity photon lifetime—the BS mode is in-gap and therefore undamped in this clean model. For a cavity with sufficiently high Q-factor it is possible in principle for polaritons to thermalize before decaying, allowing for a transient quasi-thermal ensemble. More work must be done, however, before definitive statements can be made about a condensed state, especially regarding spontaneous coherence of the condensate. Finally, we note that finite polariton density with coherence imposed externally, e.g. from a coherent driving of photon modes, would produce a non-equilibrium state with $s \pm id$ character, which one would expect to be distinct in nature from a thermodynamic $s \pm id$ state.

Furthermore, we acknowledge that the work presented in this chapter used a very simple model of a system hosting a BS mode, especially given that all observations of these modes have been in iron-based superconductors, which are described by far more complicated models featuring multiple Fermi surfaces and exotic pairing symmetries [159]. Notably, these systems host multiple different BS modes [93, 94] along with other unrelated collective modes such as the Leggett mode [160]. In order to accurately predict or explain what may be seen in experiments probing for these sorts of cavity superconductor polaritons in such real systems, a more sophisticated model that includes at least some of these complications would need to be considered.

Chapter 6: Conclusion

In this dissertation I have studied the coupling of light and two-dimensional matter in a number of different circumstances, focusing specifically on the Casimir effect, the properties of excitons, and the formation of new types of cavity polaritons.

In chapter 2 I began by examining the impact of a change in Fermi surface topology, called a Lifshitz transition, on the Casimir force. By considering a model of a semiconducting system with spin-orbit coupling and a large g-factor, an external magnetic field can be used to modify the systems band structure, removing electron pockets or adding hole pockets to the Fermi surface. At the points where the Fermi surface changes, I find the Casimir force between two such plates, or between one of these plates and a metallic plate, exhibits nonanalytic behavior as a function of magnetic field.

In chapter 3 I continued my examination of the Casimir effect with a proposal to shed light on the role of disorder in modeling metallic plates. I calculated the signature of weak localization on the Casimir force, a correction to the Drude model in two-dimensional systems. I showed that if a disordered model accurately reflects the physics of electrons in metallic plates with regards to the Casimir effect, then the Casimir force should show a similar sensitivity to temperature and magnetic fields as the conductivity of two-dimensional disordered metals. I further examined the role of disorder fluctuations, and found that in certain regimes they can average out and do not give a significant impact on the force.

In chapter 4 I turned from Casimir physics to examine the behavior of excitons in the BHZ model, describing a class of two-dimensional topological systems. By calculating the spectrum of excitons formed in the bulk of this system I demonstrated how a change in topological character can have a qualitative impact on the bulk

optical properties of a system, even though bulk transport properties are largely unaffected. I explored a semiclassical picture of excitons in the model in order to show how this difference can be understood as an effect of the Berry curvature of the model.

Finally, in chapter 5 I considered the formation of a new type of cavity polariton in analogy with cavity exciton polaritons. Substituting the usual semiconducting quantum well with a thin-film superconductor, we examined how the Bardasis-Schrieffer collective mode of a certain class of superconductors can be hybridized with cavity photon modes. I showed that the necessary coupling can be generated by a supercurrent driven through the superconductor, and that the resulting superconductor polaritons can be described by a simple Hamiltonian model. Furthermore, the strength of the hybridization between light and matter can be controlled by changing the magnitude and direction of the supercurrent, which has no apparent analog in standard exciton polariton systems. Lastly, I concluded by speculating on the possibility of condensing these superconductor polaritons and how they may be used to form an exotic superconducting state.

Appendix A: Optical signatures of excitons

There are a number of ways to come to a mathematical description of excitons in a model system, but the one that most clearly demonstrates their nature as an optical effect is to examine the optical response of the model, as given by the spatially homogeneous part of the electromagnetic response function $\Pi_{ij}(\mathbf{q} \to 0, i\omega_m)$, from which the optical conductivity can be straightforwardly derived. Begin by considering a two-band model described by the action

$$\begin{aligned} S = \sum_k \sum_{\alpha,\alpha'} \bar{\psi}_{k,\alpha} \left(-i\epsilon_n \delta_{\alpha\alpha'} + H_{\mathbf{k},\alpha\alpha'} - \mu\delta_{\alpha\alpha'} \right) \psi_{k,\alpha'} \\ + \frac{1}{2\beta} \sum_{k,k',q} \sum_{\alpha,\alpha'} U_{\mathbf{q}} \bar{\psi}_{k,\alpha} \psi_{k-q,\alpha} \bar{\psi}_{k',\alpha'} \psi_{k'+q,\alpha'} \\ + \frac{1}{\beta} \sum_{k,q} \sum_{\alpha,\alpha'} \bar{\psi}_{k,\alpha} \mathbf{A}_q \cdot \mathbf{j}_{\mathbf{k},\mathbf{q},\alpha\alpha'} \psi_{k-q,\alpha'}, \quad \text{(A.1)} \end{aligned}$$

where ψ are the field operators for fermions in the two bands, $\hat{H}$ is the Hamiltonian describing the conduction and valence bands $E_c(\mathbf{k})$ and $E_v(\mathbf{k})$, the chemical potential μ is chosen so that at low temperatures the valence band (v) is filled while the conduction band (c) is empty, $U_{\mathbf{q}}$ is the Fourier transform of the Coulomb interaction, $\mathbf{A}_q$ is the vector potential/photon field, and $\hat{\mathbf{j}}$ is the "current operator"; diagonal elements of $\hat{\mathbf{j}}$ describe actual currents in each band, while off-diagonal elements describe interband transitions. The excitation gap is defined as $E_g = \min_{\mathbf{k}} \left(E_c(\mathbf{k}) - E_v(\mathbf{k}) \right)$. For simplicity we will assume that this minimum occurs at $\mathbf{k} = 0$, though many real systems have a minimum gap at finite momentum, or an indirect gap, with the maximum of the valence band and minimum of the conduction band separated in momentum.

From this model action we can then write a diagrammatic representation of the electromagnetic response of the system, as in Fig. A.1. The first diagram represents

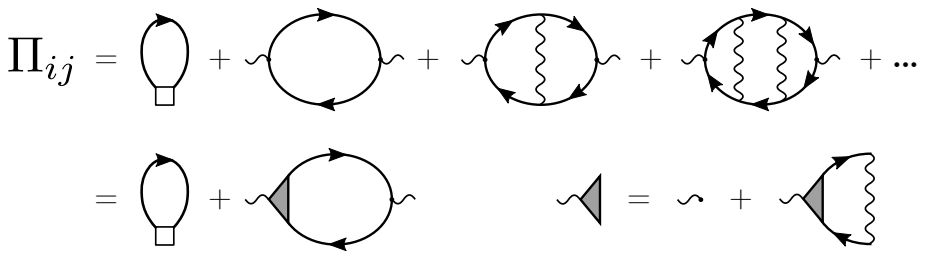

Figure A.1: The diagrammatic representation of the electromagnetic linear response function for the two band gapped system described in Eq. (A.1). The first line shows all the types of diagrams being considered, while the second line shows how the Coulomb interaction is resummed into a renormalized vertex.

the diamagnetic contribution, and the second the paramagnetic contribution in the non-interacting case. We incorporate the Coulomb interaction only at the level of the ladder approximation, which we can then resum into a renormalized current vertex as given in the second line. Diagrams with other configurations of Coulomb lines contribute at higher order. Note that the photon field is free to excite particles between bands, but we enforce that the Coulomb interaction cannot. Symbolically, the expression for Π has the straightforward form of a polarization bubble, while the renormalized vertex solves a Bethe-Salpeter equation,

$$\Pi_{ij}(i\omega_m) = \underbrace{\frac{ne^2}{m}}_{=0}\delta_{ij} - \frac{e^2}{\beta}\sum_{\mathbf{k},\epsilon_n}\sum_{\lambda,\lambda'}\tilde{\Gamma}^i_{\lambda\lambda'}(\mathbf{k},\omega_m)G_{\lambda'}(\mathbf{k},\epsilon_n+\omega_m)\Gamma^j_{\lambda'\lambda}(\mathbf{k})G_{\lambda}(\mathbf{k},\epsilon_n) \tag{A.2}$$

$$\begin{aligned}\tilde{\Gamma}^i_{\lambda\lambda'}(\mathbf{k},\omega_m) = \Gamma^i_{\lambda\lambda'}(\mathbf{k}) - \frac{1}{\beta}\sum_{\mathbf{k}',\epsilon'_n}\sum_{\lambda_1,\lambda_2} U_{\mathbf{k}-\mathbf{k}'}f_{\lambda\lambda_1}(\mathbf{k},\mathbf{k}')f_{\lambda_2\lambda'}(\mathbf{k}',\mathbf{k}) \\ \times G_{\lambda_1}(\mathbf{k}',\epsilon'_n)G_{\lambda_2}(\mathbf{k}',\epsilon'_n+\omega_m)\tilde{\Gamma}^i_{\lambda_1\lambda_2}(\mathbf{k}',\omega_m),\end{aligned} \tag{A.3}$$

where $\hat{\mathbf{\Gamma}}(\mathbf{k}) = \frac{1}{e}\hat{\mathbf{j}}_{\mathbf{k},0}$ represents the bare vertex and $\hat{\tilde{\mathbf{\Gamma}}}$ the renormalized vertex, G_λ is the Green's function for fermions in band λ, and $f_{\lambda\lambda'}(\mathbf{k},\mathbf{k}') = \langle\lambda,\mathbf{k}|\lambda',\mathbf{k}'\rangle$, where $|\lambda,\mathbf{k}\rangle$ are the single-particle eigenstates of the Hamiltonian. Note that the diamagnetic term vanishes because the total density of free carriers n in this systems is zero by design.

Excitons arise from the Coulomb interaction between particles and holes, so it is no surprise that their properties can be acquired by further analyzing the vertex correction $\widehat{\widetilde{\mathbf{\Gamma}}}$, in particular the off-diagonal, interband elements. Restricting to the off-diagonal terms of the Bethe-Salpeter equation and performing the Matsubara sum, I can then safely consider the zero-temperature limit of the expression as long as $T/E_g \ll 1$. Furthermore, I discard terms in the exchange channel, which contain inner products between conduction band and valence band states (f_{cv}). This approximation is equivalent to saying that the Coulomb interaction does not scatter between bands–particles remain particles and holes remain holes. The result is

$$\tilde{\Gamma}^i_{\lambda,-\lambda}(\mathbf{k},\omega_m) = \Gamma^i_{\lambda,-\lambda}(\mathbf{k}) + \sum_{\mathbf{k}'} U_{\mathbf{k}-\mathbf{k}'} \mathcal{F}^{\lambda}_{\mathbf{k},\mathbf{k}'} \frac{\lambda\, \tilde{\Gamma}^i_{\lambda,-\lambda}(\mathbf{k}',\omega_m)}{i\omega_m + E_\lambda(\mathbf{k}') - E_{-\lambda}(\mathbf{k}')}, \tag{A.4}$$

where I have defined $\mathcal{F}^{\lambda}_{\mathbf{k},\mathbf{k}'} = f_{\lambda\lambda}(\mathbf{k},\mathbf{k}')f_{-\lambda,-\lambda}(\mathbf{k}',\mathbf{k})$. I now expand the renormalized vertex in a new basis as $\tilde{\Gamma}^i_{\lambda,-\lambda}(\mathbf{k},\omega_m) = \sum_\nu \alpha^i_{\nu,\lambda}(\omega_m)(i\omega_m + E_\lambda(\mathbf{k}) - E_{-\lambda}(\mathbf{k}))\Phi^{(\lambda)}_\nu(\mathbf{k})$, where the new basis functions Φ are labeled by ν, which may be a continuous index for extended states and a discrete index for bound states. I substitute this into Eq. (A.4) and then isolate a frequency-independent Schrödinger-like eigenvalue equation,

$$(E_\lambda(\mathbf{k}) - E_{-\lambda}(\mathbf{k}))\Phi_\nu(\mathbf{k}) - \lambda \sum_{\mathbf{k}'} U_{\mathbf{k}-\mathbf{k}'}\ \mathcal{F}^{\lambda}_{\mathbf{k},\mathbf{k}'}\ \Phi_\nu(\mathbf{k}') = \lambda\, E_\nu\, \Phi_\nu(\mathbf{k}), \tag{A.5}$$

where I have chosen basis functions $\Phi^{(\lambda)}_\nu(\mathbf{k})$ to be the eigenfunctions of this Schrödinger equation. We see that this method gives another way to derive Eq. (1.5) by choosing $\lambda = c = +$. Note that the same functions solve this equation for both $\lambda = c = +$ and $\lambda = v = -$, so I have dropped the index from $\Phi_\nu(\mathbf{k})$. Because the Coulomb interaction is attractive, this equation has solutions with energy both greater than and less than E_g. Energies above the gap correspond to extended scattering states, and those states with energy less than the gap are the exciton bound states I seek.

I can define the exciton spectrum E_ν^{ex} through $E_\nu = E_g - |E_\nu^{\text{ex}}|$. The eigenfunctions corresponding to these eigenvalues are the exciton wave functions in their center of mass frame. I will not consider extended scattering states with energy greater than E_g.

In principle, solving Eq. (A.5) is sufficient to determine many of the properties of excitons in a given system, but I now complete the calculation I started to show how these states contribute to the optical response. With the above substitutions and by employing the Schrödinger equation, Eq. (A.4) is dramatically simplified,

$$\Gamma^i_{\lambda,-\lambda}(\mathbf{k}) = \sum_\nu \alpha^i_{\nu,\lambda}(\omega_m)(i\omega_m + \lambda E_\nu)\ \Phi_\nu(\mathbf{k}). \tag{A.6}$$

Using the fact that the wave functions C_ν form an orthonormal basis, I can invert this expression to find a closed-form expression for the expansion coefficients of the vertex correction and so write

$$\tilde{\Gamma}^i_{\lambda,-\lambda}(\mathbf{k},\omega_m) = \sum_{\mathbf{k}',\nu} \frac{i\omega_m + E_\lambda(\mathbf{k}') - E_{-\lambda}(\mathbf{k}')}{i\omega_m + \lambda E_\nu} \Phi_\nu(\mathbf{k}')\,\Gamma^i_{\lambda,-\lambda}(\mathbf{k}'). \tag{A.7}$$

Taking this form of the renormalized vertex and returning to Eq. (A.2) I arrive at

$$\Pi_{ij}(i\omega_m) \approx e^2 \sum_{\nu,\lambda} \lambda \frac{\sum_{\mathbf{k}} \Phi_\nu(\mathbf{k})\,\Gamma^i_{\lambda,-\lambda}(\mathbf{k}) \sum_{\mathbf{k}'} \Phi_\nu(\mathbf{k}')\,\Gamma^j_{-\lambda\lambda}(\mathbf{k}')}{i\omega_m + \lambda E_g - \lambda\,|E_\nu^{\text{ex}}|}. \tag{A.8}$$

Consider the diagonal elements of the response ($i = j$), and analytically continue to real frequency, $i\omega_m \to \omega + i0^+$. Also note that the interband transition element must obey $\mathbf{\Gamma}_{cv} = \mathbf{\Gamma}^*_{vc}$. Define $M^i_\nu = \sum_{\mathbf{k}} C_\nu(\mathbf{k})\,\Gamma^i_{cv}(\mathbf{k})$, and so the retarded response function takes the form

$$\Pi^R_{ii}(\omega) = e^2 \sum_\nu \left|M^i_\nu\right|^2 \left(\frac{1}{\omega + E_g - |E_\nu^{\text{ex}}| + i0^+} - \frac{1}{\omega - E_g + |E_\nu^{\text{ex}}| + i0^+} \right). \tag{A.9}$$

The two terms in Eq. (**??**) are related by time reversal, so I only need to consider one to understand how excitons appear optically. The second term has poles at positive frequency, so I consider that one.

There are a number of optical properties that I may now consider, one of the most straightforward being the optical absorption. Absorption is related to the imaginary part of the retarded response, so using the relation

$$\frac{1}{x \pm i0^+} = \mathcal{P}\frac{1}{x} \mp i\pi\delta(x) \tag{A.10}$$

we can then see that the absorption of this system is given by

$$\mathcal{A} \propto \mathrm{Im}\Pi^R_{ii}(\omega) = \pi e^2 \sum_\nu \left|M^i_\nu\right|^2 \delta\left(\omega - E_g + \left|E^{(\mathrm{ex})}_\nu\right|\right), \tag{A.11}$$

and so an optical signature of excitons is subgap features in the absorption spectrum of the system. For the system we've considered here the exciton-induced absorption appears as sharp δ-functions at precise frequencies determined by the exciton spectrum, but in a real system disorder and finite temperature would be expected to broaden the features.

Appendix B: Properties of the BHZ Hamiltonian

B.1 Symmetries and Angular Momentum

The BHZ Hamiltonian Eq. (1.13) respects both time-reversal and inversion symmetry, with the two blocks of the Hamiltonian mapping into each other under time reversal and remaining unchanged with inversion. This can be explicitly verified by representing the time reversal and inversion operators, respectively, as

$$\Theta = -i\hat{\sigma}_y K \otimes \hat{\mathbf{1}}, \text{ and } P = \hat{\mathbf{1}} \otimes \hat{\tau}_z, \tag{B.1}$$

and confirming that they commute with the Hamiltonian. Here K denotes complex conjugation. The set of single-particle eigenstates respects these symmetries as well, which one can straightforwardly verify, finding

$$\begin{aligned} \Theta \left|\mathbf{k}, \pm, i\right\rangle &= \sum_j \epsilon_{ij} \left|-\mathbf{k}, \pm, j\right\rangle \\ P\left|\mathbf{k}, \pm, i\right\rangle &= \pm \left|-\mathbf{k}, \pm, i\right\rangle . \end{aligned} \tag{B.2}$$

Here the $\pm$ labels the conduction and valence bands, while i, j labels the block of the Hamiltonian that acts on the states.

In addition to these discrete symmetries, the system is also rotationally invariant so the total angular momentum is also a good quantum number. Since the system is two-dimensional, the total angular momentum is equivalent to its z-component. The angular momentum of a particles has three components—spin, $S_z = \hat{\mathbf{1}} \otimes \hat{\sigma}_z/2$, atomic orbital, $K_z = \mathrm{diag}(0, 1, 0, -1)$, and orbital, $L_z = \hat{\mathbf{1}} \left(\mathbf{r} \times \mathbf{p}\right)_z$—so in total I have $J_z = S_z + K_z + L_z$, and a simple calculation confirms that $[J_z, H_{\mathrm{BHZ}}] = 0$.

The eigenstates of H_{BHZ} are also eigenstates of J_z, and I can most easily compute the angular momentum of single particle states at $\mathbf{k} = 0$, though the result must

hold at all points in k-space, giving

$$J_z \left|\mathbf{k}, \pm, i\right\rangle = (-1)^{i+1} \left[1 \mp \tfrac{1}{2} \operatorname{sgn} M\right] \left|\mathbf{k}, \pm, i\right\rangle . \tag{B.3}$$

Note that this value is simply either $\frac{1}{2}$ or $\frac{3}{2}$ up to a sign.

To consider excitons I must add the Coulomb interaction to this single-particle Hamiltonian. With regards to symmetry, it is enough to note that the Coulomb interaction is also invariant under time reversal, inversion, and rotations, so the states of the interacting system must obey these symmetries as well. Let intrablock exciton eigenstates be labeled as $|n, m, i\rangle$, where n and m are two quantum numbers, and i labels the block from which we take the particle and hole constituents. In the center-of-mass frame, these exciton eigenstates are

$$\left|n, m, i\right\rangle = \sum_{\mathbf{k}} C^{(i)}_{nm\mathbf{k}} \, a^{\dagger}_{\mathbf{k},+,i} a_{\mathbf{k},-,i} \left|0\right\rangle . \tag{B.4}$$

A straightforward calculation shows that

$$J_z \left|n, m, i\right\rangle = \left[m + (-1)^i \operatorname{sgn} M\right] \left|n, m, i\right\rangle \equiv j \left|n, m, i\right\rangle , \tag{B.5}$$

where the second term in the eigenvalue is the sum of the spin and orbital angular momenta of the single-particle bands, Eq.B.3. We see here that m labels the part of the angular momentum interpreted classically as arising from the relative motion of the exciton's constituent particle and hole. Furthermore, it can be easily verified that time reversal acts in the expected way, simply flipping the sign of the angular momentum, $J_z \Theta \left|n, m, i\right\rangle = -j \, \Theta \left|n, m, i\right\rangle$.

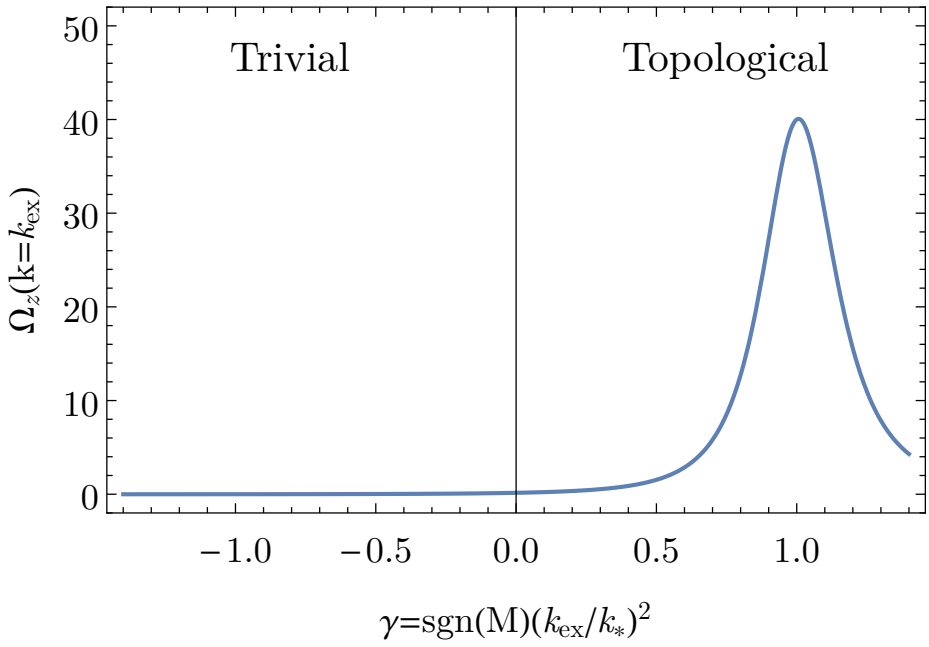

Figure B.1: A plot of the z-component of the Berry curvature $\mathbf{\Omega}_+$ as a function of the parameter γ, evaluated at the characteristic exciton momentum k_{ex}. The Berry curvature $\mathbf{\Omega}_-$ is related by an overall sign. In the topological regime the Berry curvature is peaked near $\gamma = 1$ which implies $k_{\text{ex}} \approx k_*$ and is positive for all values of the momentum, leading to a nonzero Chern number, while in the trivial regime it takes both positive and negative values producing a Chern number of 0.

B.2 Two-particle Berry physics in the BHZ model

A plot of the Berry curvature versus γ in the topological and trivial regimes is presented in Fig. B.1. Calculating the Berry curvature for the lower block of the Hamiltonian gives the same results up to overall signs.

When considering the interacting two-particle problem, I define the particle and hole states as

$$|\mathbf{k}, e\rangle = |\mathbf{k}, +\rangle\,, \quad |\mathbf{k}, h\rangle = \mathcal{C}\,|\mathbf{k}, -\rangle\,, \tag{B.6}$$

using the particle-hole transformation $\mathcal{C} = K\hat{\sigma}_x$. With these definitions, I can define the Berry connections for particles and holes in the upper block analogously as in Eq. (1.17) to find $\mathbf{A}_e(\mathbf{k}) = \mathbf{A}_+(\mathbf{k})$ and $\mathbf{A}_h(\mathbf{k}) = \mathbf{A}_-(\mathbf{k}) = -\mathbf{A}_e(\mathbf{k})$. The Berry curvature is then calculated as the curl of the Berry connection.

Bibliography

[1]H. B. G. Casimir, "On the attraction between two perfectly conducting plates", Proc. K. Ned. Akad. Wet. **51**, 793 (1948).

[2]M. Bordag, U. Mohideen, and V. M. Mostepanenko, "New developments in the Casimir effect", Phys. Rep. **353**, 1–205 (2001).

[3]E. M. Lifshitz, "The theory of molecular attractive forces between solids", Sov. Phys. JETP **2**, 73 (1956).

[4]I. E. Dzyaloshinskii, E. M. Lifshitz, and L. P. Pitaevskii, "General theory of van der Waals' forces", Sov. Phys. Usp. **4**, 153–176 (1961).

[5]S. K. Lamoreaux, "Demonstration of the Casimir force in the 0.6 to 6μm range", Phys. Rev. Lett. **78**, 5–8 (1997).

[6]K. A. Milton, *The Casimir Effect*, Physical Manifestations of Zero-point energy (World Scientific, 2001).

[7]K. A. Milton, "Recent developments in the Casimir effect", Journal of Physics: Conference Series **161**, 012001 (2009).

[8]M. Sparnaay, "Attractive forces between flat plates", Nature **180**, 334–335 (1957).

[9]M. Sparnaay, "Measurements of attractive forces between flat plates", Physica **24**, 751–764 (1958).

[10]S. K. Lamoreaux, "The Casimir force: background, experiments, and applications", Rep. Prog. Phys. **68**, 201–236 (2005).

[11]U. Mohideen and A. Roy, "Precision measurement of the Casimir force from 0.1 to 0.9 μm", Phys. Rev. Lett. **81**, 4549–4552 (1998).

[12]J. N. Munday, F. Capasso, and V. A. Parsegian, "Measured long-range repulsive Casimir–Lifshitz forces", Nature (London) **457**, 170–173 (2009).

[13]A. A. Banishev, G. L. Klimchitskaya, V. M. Mostepanenko, and U. Mohideen, "Demonstration of the Casimir force between ferromagnetic surfaces of a Ni-coated sphere and a Ni-coated plate", Phys. Rev. Lett. **110**, 137401 (2013).

[14]P. Bruno, "Long-range magnetic interaction due to the Casimir effect", Phys. Rev. Lett. **88**, 240401 (2002).

[15]G. Metalidis and P. Bruno, "Magnetic Casimir effect", Phys. Rev. A **66**, 062102 (2002).

[16]G. Bimonte, E. Calloni, G. Esposito, and L. Rosa, "Variations of Casimir energy from a superconducting transition", Nucl. Phys. B **726**, 441–463 (2005).

[17]G. Bimonte, E. Calloni, G. Esposito, L. Milano, and L. Rosa, "Towards measuring variations of Casimir energy by a superconducting cavity", Phys. Rev. Lett. **94**, 180402 (2005).

[18]A. O. Sushkov, W. J. Kim, D. A. R. Dalvit, and S. K. Lamoreaux, "Observation of the thermal Casimir force", Nature Physics **7**, 230–233 (2011).

[19]G. Torricelli et al., "Switching Casimir forces with phase-change materials", Phys. Rev. A **82**, 010101 (2010).

[20]P. Ziherl, R. Podgornik, and S. Žumer, "Casimir force in liquid crystals close to the nematic–isotropic phase transition", Chem. Phys. Lett. **295**, 99–104 (1998).

[21]F. Chen, G. L. Klimchitskaya, V. M. Mostepanenko, and U. Mohideen, "Control of the Casimir force by the modification of dielectric properties with light", Phys. Rev. B **76**, 035338 (2007).

[22]S. de Man, K. Heeck, R. J. Wijngaarden, and D. Iannuzzi, "Halving the Casimir force with conductive oxides", Phys. Rev. Lett. **103**, 040402 (2009).

[23]C.-C. Chang, A. A. Banishev, G. L. Klimchitskaya, V. M. Mostepanenko, and U. Mohideen, "Reduction of the Casimir force from indium tin oxide film by UV treatment", Phys. Rev. Lett. **107**, 090403 (2011).

[24]M. Bordag, B. Geyer, G. L. Klimchitskaya, and V. M. Mostepanenko, "Constraints for hypothetical interactions from a recent demonstration of the Casimir force and some possible improvements", Phys. Rev. D **58**, 075003 (1998).

[25]J. C. Long et al., "Upper limits to submillimetre-range forces from extra space-time dimensions", Nature **421**, 922–925 (2003).

[26]R. S. Decca et al., "Constraining new forces in the Casimir regime using the isoelectronic technique", Phys. Rev. Lett. **94**, 240401 (2005).

[27]D. J. Kapner et al., "Tests of the gravitational inverse-square law below the dark-energy length scale", Phys. Rev. Lett. **98**, 021101 (2007).

[28]D. M. Weld, J. Xia, B. Cabrera, and A. Kapitulnik, "New apparatus for detecting micron-scale deviations from Newtonian gravity", Phys. Rev. D **77**, 062006 (2008).

[29]F. Capasso, J. N. Munday, D. Iannuzzi, and H. B. Chan, "Casimir forces and quantum electrodynamical torques: physics and nanomechanics", IEEE J. Sel. Topics Quantum Electron. **13**, 400–414 (2007).

[30]M. Levin, A. P. McCauley, A. W. Rodriguez, M. T. H. Reid, and S. G. Johnson, "Casimir repulsion between metallic objects in vacuum", Phys. Rev. Lett. **105**, 090403 (2010).

[31]S. A. Fulling, L. Kaplan, and J. H. Wilson, "Vacuum energy and repulsive Casimir forces in quantum star graphs", Phys. Rev. A **76**, 012118 (2007).

[32]O. Kenneth and I. Klich, "Opposites attract: a theorem about the Casimir force", Phys. Rev. Lett. **97**, 160401 (2006).

[33]W.-K. Tse and A. H. MacDonald, "Quantized Casimir force", Phys. Rev. Lett. **109**, 236806 (2012).

[34]A. G. Grushin and A. Cortijo, "Tunable Casimir repulsion with three-dimensional topological insulators", Phys. Rev. Lett. **106**, 020403 (2011).

[35]J. H. Wilson, A. A. Allocca, and V. Galitski, "Repulsive Casimir force between Weyl semimetals", Phys. Rev. B **91**, 235115 (2015).

[36]A. A. Allocca, J. H. Wilson, and V. Galitski, "Nonanalytic behavior of the Casimir force across a Lifshitz transition in a spin-orbit-coupled material", Phys. Rev. B **90**, 075420 (2014).

[37]R. Decca et al., "Precise comparison of theory and new experiment for the Casimir force leads to stronger constraints on thermal quantum effects and long-range interactions", Ann. Phys. **318**, 37–80 (2005).

[38]R. S. Decca et al., "Tests of new physics from precise measurements of the Casimir pressure between two gold-coated plates", Phys. Rev. D **75**, 077101 (2007).

[39]R. Castillo-Garza, J. Xu, G. L. Klimchitskaya, V. M. Mostepanenko, and U. Mohideen, "Casimir interaction at liquid nitrogen temperature: Comparison between experiment and theory", Phys. Rev. B **88**, 075402 (2013).

[40]A. A. Banishev, G. L. Klimchitskaya, V. M. Mostepanenko, and U. Mohideen, "Casimir interaction between two magnetic metals in comparison with nonmagnetic test bodies", Phys. Rev. B **88**, 155410 (2013).

[41]D. Garcia-Sanchez, K. Y. Fong, H. Bhaskaran, S. Lamoreaux, and H. X. Tang, "Casimir force and in situ surface potential measurements on nanomembranes", Phys. Rev. Lett. **109**, 027202 (2012).

[42]R. O. Behunin, F. Intravaia, D. A. R. Dalvit, P. A. M. Neto, and S. Reynaud, "Modeling electrostatic patch effects in Casimir force measurements", Phys. Rev. A **85**, 012504 (2012).

[43]R. O. Behunin et al., "Kelvin probe force microscopy of metallic surfaces used in Casimir force measurements", Phys. Rev. A **90**, 062115 (2014).

[44]J. L. Garrett, D. Somers, and J. N. Munday, "The effect of patch potentials in Casimir force measurements determined by heterodyne Kelvin probe force microscopy", Journal of Physics: Condensed Matter **27**, 214012 (2015).

[45]A. Naji, D. S. Dean, J. Sarabadani, R. R. Horgan, and R. Podgornik, "Fluctuation-induced interaction between randomly charged dielectrics", Phys. Rev. Lett. **104**, 060601 (2010).

[46]G. H. Wannier, "The structure of electronic excitation levels in ensulating crystals", Phys. Rev. **52**, 191–197 (1937).

[47]C. Kittel, *Introduction to Solid State Physics*, 8th ed. (Wiley, 2004).

[48]M. Kira and S. Koch, "Many-body correlations and excitonic effects in semiconductor spectroscopy", Progress in Quantum Electronics **30**, 155–296 (2006).

[49]"Saturation of the free exciton resonance in GaAs", Solid State Communications **30**, 271–275.

[50]S. Schmitt-Rink, D. Chemla, and D. Miller, "Linear and nonlinear optical properties of semiconductor quantum wells", Advances in Physics **38**, 89–188 (1989).

[51]Y. H. Lee et al., "Room-temperature optical nonlinearities in GaAs", Phys. Rev. Lett. **57**, 2446–2449 (1986).

[52]G. W. Fehrenbach, W. Schäfer, J. Treusch, and R. G. Ulbrich, "Transient optical spectra of a dense exciton gas in a direct-gap semiconductor", Phys. Rev. Lett. **49**, 1281–1284 (1982).

[53]J. J. Hopfield, "Theory of the contribution of excitons to the complex dielectric constant of crystals", Phys. Rev. **112**, 1555–1567 (1958).

[54]C. Weisbuch, M. Nishioka, A. Ishikawa, and Y. Arakawa, "Observation of the coupled exciton-photon mode splitting in a semiconductor quantum microcavity", Phys. Rev. Lett. **69**, 3314–3317 (1992).

[55]J. Kasprzak et al., "Bose-Einstein condensation of exciton polaritons", Nature **443**, 409 (2006).

[56]A. L. Fetter and J. D. Walecka, *Quantum Theory of Many-Particle Systems* (McGraw-Hill, Boston, 1971).

[57]E. Wertz et al., "Spontaneous formation and optical manipulation of extended polariton condensates", Nature physics **6**, 860 (2010).

[58]F. Li et al., "From excitonic to photonic polariton condensate in a ZnO-based microcavity", Phys. Rev. Lett. **110**, 196406 (2013).

[59]Y. Sun et al., "Bose-Einstein condensation of long-lifetime polaritons in thermal equilibrium", Phys. Rev. Lett. **118**, 016602 (2017).

[60]A. Kavokin, G. Malpuech, and M. Glazov, "Optical spin Hall effect", Phys. Rev. Lett. **95**, 136601 (2005).

[61]C. Leyder et al., "Observation of the optical spin Hall effect", Nature Physics **3**, 628–631 (2007).

[62]T. Jacqmin et al., "Direct observation of Dirac cones and a flatband in a honeycomb lattice for polaritons", Phys. Rev. Lett. **112**, 116402 (2014).

[63]C. E. Whittaker et al., "Exciton polaritons in a two-dimensional Lieb lattice with spin-orbit coupling", Phys. Rev. Lett. **120**, 097401 (2018).

[64]H. S. Nguyen et al., "Acoustic black hole in a stationary hydrodynamic flow of microcavity polaritons", Phys. Rev. Lett. **114**, 036402 (2015).

[65]F. Baboux et al., "Measuring topological invariants from generalized edge states in polaritonic quasicrystals", Phys. Rev. B **95**, 161114 (2017).

[66]I. Carusotto and C. Ciuti, "Quantum fluids of light", Rev. Mod. Phys. **85**, 299–366 (2013).

[67]I. M. Lifshitz, "Anomalies of electron characteristics of a metal in the high pressure region", Sov. Phys. JETP **38**, 1569 (1960).

[68]A. A. Abrikosov, *Fundamentals of the theory of metals* (North-Holland, Amsterdam, 1988).

[69]K.-S. Chen, Z. Y. Meng, T. Pruschke, J. Moreno, and M. Jarrell, "Lifshitz transition in the two-dimensional Hubbard model", Phys. Rev. B **86**, 165136 (2012).

[70]Y. Okamoto, A. Nishio, and Z. Hiroi, "Discontinuous Lifshitz transition achieved by band-filling control in Na_xCoO_2", Phys. Rev. B **81**, 121102 (2010).

[71]A. Hackl and M. Vojta, "Zeeman-driven Lifshitz transition: a model for the experimentally observed Fermi-surface reconstruction in $YbRh_2Si_2$", Phys. Rev. Lett. **106**, 137002 (2011).

[72]M. R. Norman, J. Lin, and A. J. Millis, "Lifshitz transition in underdoped cuprates", Phys. Rev. B **81**, 180513 (2010).

[73]C. Liu et al., "Evidence for a Lifshitz transition in electron-doped iron arsenic superconductors at the onset of superconductivity", Nature Phys. **6**, 419–423 (2010).

[74]S. Hikami, A. I. Larkin, and Y. Nagaoka, "Spin-orbit interaction and magnetoresistance in the two dimensional random system", Prog. Theor. Phys, **63**, 707–710 (1980).

[75]B. L. Altshuler, D. Khmel'nitzkii, A. I. Larkin, and P. A. Lee, "Magnetoresistance and Hall effect in a disordered two-dimensional electron gas", Phys. Rev. B **22**, 5142–5153 (1980).

[76]P. A. Lee and T. V. Ramakrishnan, "Disordered electronic systems", Rev. Mod. Phys. **57**, 287–337 (1985).

[77]G. Bergmann, "Weak localization in thin films: a time-of-flight experiment with conduction electrons", Phys. Rep. **107**, 1–58 (1984).

[78]J. J. Lin and J. P. Bird, "Recent experimental studies of electron dephasing in metal and semiconductor mesoscopic structures", Journal of Physics: Condensed Matter **14**, R501–R596 (2002).

[79]B. L. Altshuler, A. G. Aronov, and D. E. Khmelnitsky, "Effects of electron-electron collisions with small energy transfers on quantum localisation", Journal of Physics C: Solid State Physics **15**, 7367–7386 (1982).

[80]L. D. Landau, "On the theory of phase transitions", Zh. Eksp. Teor. Fiz. **7**, 19–32 (1937).

[81]V. L. Ginzburg and L. D. Landau, "On the theory of superconductivity", Zh. Eksp. Teor. Fiz. **20**, 1064–1082 (1950).

[82]P. W. Anderson, *Basic Notions of Condensed Matter Physics* (Westview Press / Addison-Wesley, 1997).

[83]K. v. Klitzing, G. Dorda, and M. Pepper, "New method for high-accuracy determination of the fine-structure constant based on quantized Hall resistance", Phys. Rev. Lett. **45**, 494–497 (1980).

[84]D. J. Thouless, M. Kohmoto, M. P. Nightingale, and M. den Nijs, "Quantized Hall conductance in a two-dimensional periodic potential", Phys. Rev. Lett. **49**, 405–408 (1982).

[85]M. Z. Hasan and C. L. Kane, "Colloquium: Topological insulators", Rev. Mod. Phys. **82**, 3045–3067 (2010).

[86]X.-L. Qi and S.-C. Zhang, "Topological insulators and superconductors", Rev. Mod. Phys. **83**, 1057–1110 (2011).

[87]B. A. Bernevig, T. L. Hughes, and S.-C. Zhang, "Quantum spin Hall effect and topological phase transition in HgTe quantum wells", Science **314**, 1757–1761 (2006).

[88]M. König et al., "Quantum spin Hall insulator state in HgTe quantum wells", **318**, 766–770 (2007).

[89]M. V. Berry, "Quantal phase factors accompanying adiabatic changes", Proceedings of the Royal Society of London. A. Mathematical and Physical Sciences **392**, 45–57 (1984).

[90]A. Bardasis and J. R. Schrieffer, "Excitons and plasmons in superconductors", Phys. Rev. **121**, 1050–1062 (1961).

[91]F. Kretzschmar et al., "Raman-scattering detection of nearly degenerate *s*-wave and *d*-wave pairing channels in iron-based $Ba_{0.6}K_{0.4}Fe_2As_2$ and $Rb_{0.8}Fe_{1.6}Se_2$ superconductors", Phys. Rev. Lett. **110**, 187002 (2013).

[92]T. Böhm et al., "Balancing act: evidence for a strong subdominant *d*-wave pairing channel in $Ba_{0.6}K_{0.4}Fe_2As_2$", Phys. Rev. X **4**, 041046 (2014).

[93]D. Jost et al., "Indication of subdominant *d*-wave interaction in superconducting $CaKFe_4As_4$", Phys. Rev. B **98**, 020504 (2018).

[94]S. Maiti, T. A. Maier, T. Böhm, R. Hackl, and P. J. Hirschfeld, "Probing the pairing interaction and multiple Bardasis-Schrieffer modes using Raman spectroscopy", Phys. Rev. Lett. **117**, 257001 (2016).

[95]P. Parashar, K. A. Milton, K. V. Shajesh, and M. Schaden, "Electromagnetic semitransparent δ-function plate: Casimir interaction energy between parallel infinitesimally thin plates", Phys. Rev. D **86**, 085021 (2012).

[96]G. Barton, "Casimir effects for a flat plasma sheet: I. Energies", Journal of Physics A: Mathematical and General **38**, 2997–3019 (2005).

[97]G. Barton, "Casimir effects for a flat plasma sheet: II. Fields and stresses", Journal of Physics A: Mathematical and General **38**, 3021–3044 (2005).

[98]M. Bordag, I. V. Fialkovsky, D. M. Gitman, and D. V. Vassilevich, "Casimir interaction between a perfect conductor and graphene described by the Dirac model", Phys. Rev. B **80**, 245406 (2009).

[99]D. Drosdoff and L. M. Woods, "Casimir forces and graphene sheets", Phys. Rev. B **82**, 155459 (2010).

[100]B. E. Sernelius, "Casimir interactions in graphene systems", EPL (Europhysics Letters) **95**, 57003 (2011).

[101]J. D. Koralek et al., "Emergence of the persistent spin helix in semiconductor quantum wells", Nature **458**, 610–613 (2009).

[102]R. Winkler, *Spin–Orbit Coupling Effects in Two-Dimensional Electron and Hole Systems*, Vol. 191, Springer Tracts in Modern Physics (Springer Berlin Heidelberg, Berlin, Heidelberg, 2003).

[103]A. Altland and B. D. Simons, *Condensed Matter Field Theory*, 2nd (Cambridge University Press, Cambridge, 2010).

[104]A. A. Allocca, J. H. Wilson, and V. M. Galitski, "Quantum interference phenomena in the Casimir effect", Phys. Rev. A **91**, 062512 (2015).

[105]G. L. Klimchitskaya, U. Mohideen, and V. M. Mostepanenko, "The Casimir force between real materials: Experiment and theory", Rev. Mod. Phys. **81**, 1827–1885 (2009).

[106]N. W. Ashcroft and N. D. Mermin, *Solid State Physics* (Saunders College, 1976), p. 826.

[107]R. S. Decca, D. López, and E. Osquiguil, "New results for the Casimir interaction: sample characterization and low temperature measurements", Int. J. Mod Phys A **25**, 2223–2230 (2010).

[108]B. L. Altshuler, "Fluctuations in the extrinsic conductivity of disordered conductors", JETP lett. **41**, 648 (1985).

[109]P. A. Lee and A. D. Stone, "Universal conductance fluctuations in metals", Phys. Rev. Lett. **55**, 1622–1625 (1985).

[110]V. B. Bezerra, G. L. Klimchitskaya, and V. M. Mostepanenko, "Correlation of energy and free energy for the thermal Casimir force between real metals", Phys. Rev. A **66**, 062112 (2002).

[111]V. B. Bezerra, G. L. Klimchitskaya, V. M. Mostepanenko, and C. Romero, "Violation of the Nernst heat theorem in the theory of the thermal Casimir force between Drude metals", Phys. Rev. A **69**, 022119 (2004).

[112]J. Rammer, "Quantum transport theory of electrons in solids: A single-particle approach", Rev. Mod. Phys. **63**, 781–817 (1991).

[113]A. A. Allocca, D. K. Efimkin, and V. M. Galitski, "Fingerprints of Berry phases in the bulk exciton spectrum of a topological insulator", Phys. Rev. B **98**, 045430 (2018).

[114]I. Garate and M. Franz, "Excitons and optical absorption on the surface of a strong topological insulator with a magnetic energy gap", Phys. Rev. B **84**, 045403 (2011).

[115]D. K. Efimkin and Y. E. Lozovik, "Resonant manifestations of chiral excitons in Faraday and Kerr effects in a topological insulator film", Phys. Rev. B **87**, 245416 (2013).

[116]D. K. Efimkin, Y. E. Lozovik, and A. A. Sokolik, "Electron-hole pairing in a topological insulator thin film", Phys. Rev. B **86**, 115436 (2012).

[117]J. M. Blatt, K. W. Böer, and W. Brandt, "Bose-Einstein condensation of excitons", Phys. Rev. **126**, 1691–1692 (1962).

[118]B. Seradjeh, J. E. Moore, and M. Franz, "Exciton condensation and charge fractionalization in a topological insulator film", Phys. Rev. Lett. **103**, 066402 (2009).

[119]D. I. Pikulin and T. Hyart, "Interplay of exciton condensation and the quantum spin Hall effect in InAs/GaSb bilayers", Phys. Rev. Lett. **112**, 176403 (2014).

[120]S. Juergens, P. Michetti, and B. Trauzettel, "Plasmons due to the interplay of Dirac and Schrödinger fermions", Phys. Rev. Lett. **112**, 076804 (2014).

[121]K. Saha, K. Légaré, and I. Garate, "Detecting band inversions by measuring the environment: fingerprints of electronic band topology in bulk phonon linewidths", Phys. Rev. Lett. **115**, 176405 (2015).

[122]A. Srivastava and A. Imamoğlu, "Signatures of Bloch-band geometry on excitons: nonhydrogenic spectra in transition-metal dichalcogenides", Phys. Rev. Lett. **115**, 166802 (2015).

[123]J. Zhou, W.-Y. Shan, W. Yao, and D. Xiao, "Berry phase modification to the energy spectrum of excitons", Phys. Rev. Lett. **115**, 166803 (2015).

[124]G. Wang et al., "Colloquium: Excitons in atomically thin transition metal dichalcogenides", Rev. Mod. Phys. **90**, 021001 (2018).

[125]A. P. Silin and S. V. Shubenkov, "Wannier-mott excitons in narrow-gap semiconductor heterostructures", Physics of the Solid State **42**, 24–28 (2000).

[126]M. Trushin, M. O. Goerbig, and W. Belzig, "Optical absorption by Dirac excitons in single-layer transition-metal dichalcogenides", Phys. Rev. B **94**, 041301 (2016).

[127]L. V. Keldysh, "Coulomb interaction in thin semiconductor and semimetal films", JETP Letters **29**, 658 (1979).

[128]A. Chernikov et al., "Exciton binding energy and nonhydrogenic Rydberg series in monolayer WS_2", Phys. Rev. Lett. **113**, 076802 (2014).

[129]G. Bir and G. Pikus, *Symmetry and Strain-induced Effects in Semiconductors*, A Halsted Press book (Wiley, New York, 1974).

[130]G. Sundaram and Q. Niu, "Wave-packet dynamics in slowly perturbed crystals: Gradient corrections and Berry-phase effects", Phys. Rev. B **59**, 14915–14925 (1999).

[131]M.-C. Chang and Q. Niu, "Berry curvature, orbital moment, and effective quantum theory of electrons in electromagnetic fields", Journal of Physics: Condensed Matter **20**, 193202 (2008).

[132]D. Xiao, M.-C. Chang, and Q. Niu, "Berry phase effects on electronic properties", Rev. Mod. Phys. **82**, 1959–2007 (2010).

[133]M. Trushin, M. O. Goerbig, and W. Belzig, "Model prediction of self-rotating excitons in two-dimensional transition-metal dichalcogenides", Phys. Rev. Lett. **120**, 187401 (2018).

[134]X. L. Yang, M. Lieber, and F. T. Chan, "The Runge–Lenz vector for the two-dimensional hydrogen atom", American Journal of Physics **59**, 231–232 (1991).

[135]D. G. W. Parfitt and M. E. Portnoi, "The two-dimensional hydrogen atom revisited", Journal of Mathematical Physics **43**, 4681–4691 (2002).

[136]C. Y.-P. Chao and S. L. Chuang, "Analytical and numerical solutions for a two-dimensional exciton in momentum space", Phys. Rev. B **43**, 6530–6543 (1991).

[137]J. P. Provost and G. Vallee, "Riemannian structure on manifolds of quantum states", Communications in Mathematical Physics **76**, 289–301 (1980).

[138]I. Sodemann and L. Fu, "Quantum nonlinear Hall effect induced by Berry curvature dipole in time-reversal invariant materials", Phys. Rev. Lett. **115**, 216806 (2015).

[139]A. A. Allocca, Z. M. Raines, J. B. Curtis, and V. M. Galitski, "Cavity superconductor-polaritons", Phys. Rev. B **99**, 020504 (2019).

[140]F. P. Laussy, A. V. Kavokin, and I. A. Shelykh, "Exciton-polariton mediated superconductivity", Phys. Rev. Lett. **104**, 106402 (2010).

[141]G. Baskaran, *Superradiant superconductivity*, 2012, arXiv:1211.4567 [cond-mat.supr-con].

[142]O. Cotleţ, S. Zeytinoğlu, M. Sigrist, E. Demler, and A. Imamoğlu, "Superconductivity and other collective phenomena in a hybrid Bose-Fermi mixture formed by a polariton condensate and an electron system in two dimensions", Phys. Rev. B **93**, 054510 (2016).

[143]J. B. Curtis, Z. M. Raines, A. A. Allocca, M. Hafezi, and V. M. Galitski, "Cavity quantum Eliashberg enhancement of superconductivity", Phys. Rev. Lett. **122**, 167002 (2019).

[144]M. A. Sentef, M. Ruggenthaler, and A. Rubio, "Cavity quantum-electrodynamical polaritonically enhanced electron-phonon coupling and its influence on superconductivity", Science Advances **4** (2018) 10.1126/sciadv.aau6969.

[145]F. Schlawin, A. Cavalleri, and D. Jaksch, "Cavity-mediated electron-photon superconductivity", Phys. Rev. Lett. **122**, 133602 (2019).

[146]A. Moor, A. F. Volkov, and K. B. Efetov, "Amplitude Higgs mode and admittance in superconductors with a moving condensate", Phys. Rev. Lett. **118**, 047001 (2017).

[147]S. Nakamura et al., "Infrared activation of Higgs mode by supercurrent injection in a superconductor NbN", ArXiv e-prints (2018), arXiv:1809.10335 [cond-mat.supr-con].

[148]C. Maissen et al., "Ultrastrong coupling in the near field of complementary split-ring resonators", Phys. Rev. B **90**, 205309 (2014).

[149]A. Kamenev, *Field Theory of Non-Equilibrium Systems* (Cambridge University Press, 2011).

[150]A. Bayer et al., "Terahertz light–matter interaction beyond unity coupling strength", Nano Letters **17**, 6340–6344 (2017).

[151]S. Maiti and P. J. Hirschfeld, "Collective modes in superconductors with competing *s*- and *d*-wave interactions", Phys. Rev. B **92**, 094506 (2015).

[152]E. F. Talantsev and J. L. Tallon, "Universal self-field critical current for thin-film superconductors", Nature Communications **6**, 7820 (2015).

[153]S. J. Singh et al., "Ultrahigh critical current densities, the vortex phase diagram, and the effect of granularity of the stoichiometric high-T_c superconductor $CaKFe_4As_4$", Phys. Rev. Materials **2**, 074802 (2018).

[154]M. M. Qazilbash et al., "Electronic correlations in the iron pnictides", Nature Physics **5**, 647 (2009).

[155]N. Bari ši ć et al., "Electrodynamics of electron-doped iron pnictide superconductors: Normal-state properties", Phys. Rev. B **82**, 054518 (2010).

[156]D. C. Johnston, "The puzzle of high temperature superconductivity in layered iron pnictides and chalcogenides", Advances in Physics **59**, 803–1061 (2010).

[157]V. Cvetkovic and O. Vafek, "Space group symmetry, spin-orbit coupling, and the low-energy effective hamiltonian for iron-based superconductors", Phys. Rev. B **88**, 134510 (2013).

[158]M. Galassi and B. Gough, *GNU Scientific Library: Reference Manual*, GNU manual (Network Theory, 2009).

[159]P. J. Hirschfeld, M. M. Korshunov, and I. I. Mazin, "Gap symmetry and structure of Fe-based superconductors", Reports on Progress in Physics **74**, 124508 (2011).

[160]A. J. Leggett, "Number-phase fluctuations in two-band superconductors", Progress of Theoretical Physics **36**, 901–930 (1966).